Universität Bielefeld

Fakultät für Physik
Theorie der Kondensierten Materie

Lipid-Protein Interactions in Lipid Membranes

Dissertation

zur Erlangung des Doktorgrades
an der Fakultät für Physik
der Universität Bielefeld

vorgelegt von

Beate Monika Lieselotte West

3. Dezember 2008

begutachtet durch

Prof. Dr. Friederike Schmid
Prof. Dr. Jürgen Schnack

Gedruckt auf alterungsbeständigem Papier gemäß ISO 9706.

Für Torsten und meine Eltern.

Contents

Nicht in der Kenntnis liegt die Frucht,
sondern im Erfassen.

Bernhard von Clairvaux,
Über die Betrachtung, 105

1 Introduction

Biomembranes play a central role in both the structure and function of all biological cells [34]. They serve as an interface between different areas within a cell. The biomembrane consists of a liquid-like bilayer of amphiphile lipids, into which membrane proteins and other macromolecules are inserted or attached, figure 1.1. The major role of the lipids is to form a stable bilayer matrix with which the proteins interact. The lipids are also responsible for the physicochemical characteristics of the membrane, i.e. the structure and function of the membrane are determined by the lipids. The proteins, e.g. receptors, enzymes and ion channels, are the biochemically active components. Their functions are very versatile: transport (exchange of material away over the membrane), enzyme activity, signal transmission (receptors), cell connection, cell-cell recognition. The relative amounts of protein and lipid composition vary significantly. The amount of proteins varies from 20% to 80% of the membrane's dry weight. In this thesis we investigate generic mechanisms of lipid-protein interactions. In the following we introduce the single components.

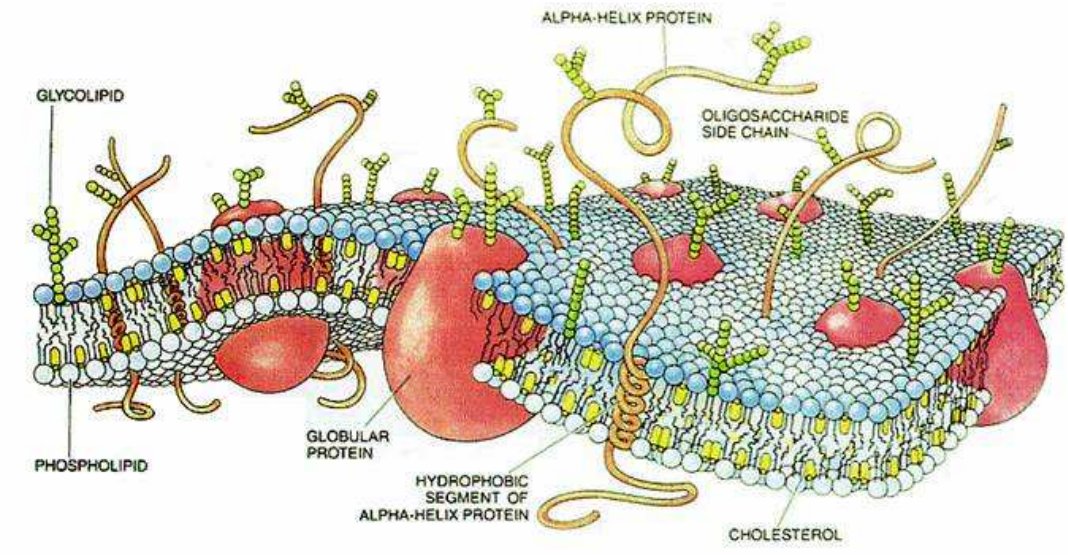

Figure 1.1: Schematic drawing of a membrane [1]

1.1 Membrane Lipids

Membrane lipids are very diverse. Any single membrane can contain over 100 different lipids. However, all the different lipid types have one thing in common, they are amphiphiles. They consist of a hydrophilic head group and one or more hydrophobic tails. The composition of the head group as well as the number of carbon atoms and the number of double bonds in the tails differ from lipid to lipid. The most common class of lipids in biomembranes are the phospholipids. They consist of a polar charged phosphate head group, followed by a semipolar glycerol backbone. The fatty acid tail chains vary widely in length, branching and saturation. The acyl chains nearly always have an even number of carbon atoms ranging from 14 to 24. The degree of unsaturation indicates the number of double bonds within a fatty acid tail. A double bond often places a kink in the molecule. Many phospholipid molecules have one saturated and one unsaturated tail chain. Our model lipid corresponds to the lipid dipalmitoyl phosphatidylcholine (DPPC), figure 1.2. This lipid belongs to the phosphatidylcholines, a class of the phospholipids. This is the most abundant lipid class in mammalian membranes [58].

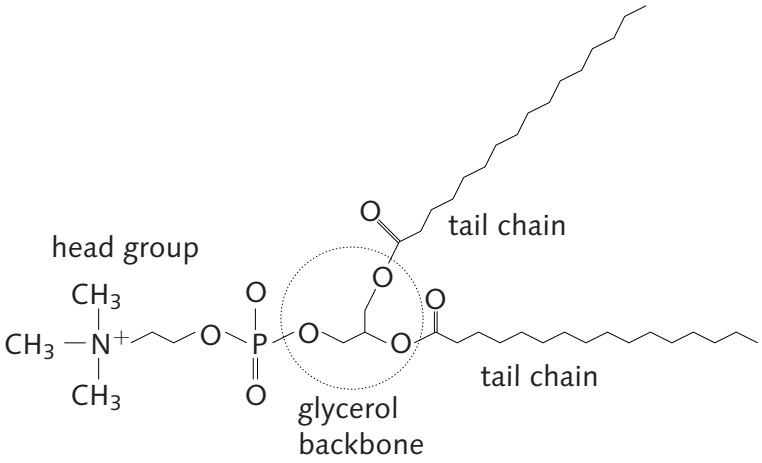

Figure 1.2: Chemical structure of dipalmitoyl phosphatidylcholine

In an aqueous environment the lipids tend to assemble in different kinds of aggregates: Bilayers, micelles and vesicles, figure 1.3. Due to their hydrophilic nature the head group of the lipids points towards the water. In a bilayer the lipids form two monolayers with all the tails oriented in the same direction. The two monolayers are arranged such that the tails face each other and are shielded from the aqueous environment by the head groups. A vesicle is a bilayer forming a closed structure. In a micelle the lipids form a sphere with the head groups facing towards the water. The inner part of the sphere contains the tails. Inverted micelles are spherical droplets surrounded by lipids with the heads groups facing inwards towards the water. The aggregate the lipids prefer depends on the molecular shape of the lipids.

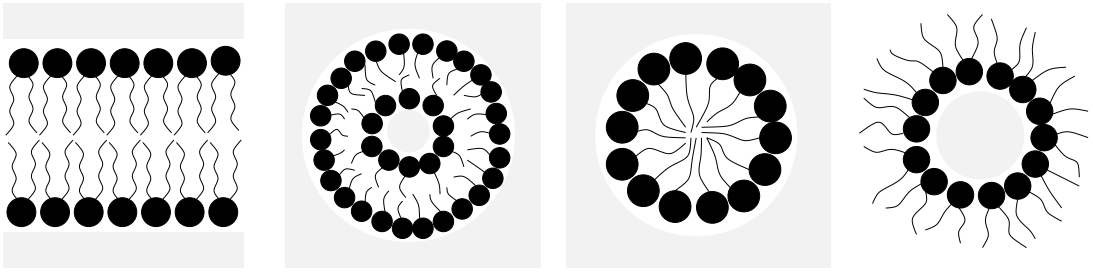

(a) (b) (c) (d)

Figure 1.3: Aggregates of lipid molecules in an aqueous environment: Bilayer (a), vesicle (b), micelle (c) and inverted micelle (d). The aqueous environment is presented by the grey area.

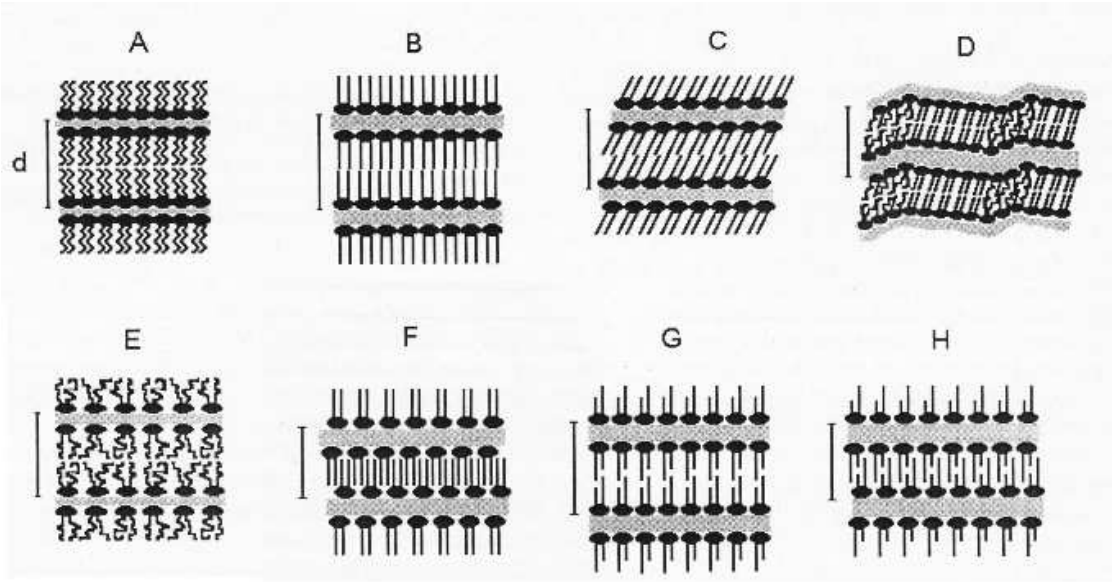

Figure 1.4: Schematic drawing of various lipid phases found in phosphatidylcholine/water mixtures: (A) subgel L_c, (B) gel (untilted chains) L_β, (B) gel (tilted chains) $L_{\beta'}$, (D) ripple gel $P_{\beta'}$ (does not correspond with our perceptions [64, 66]), (E) liquid crystalline L_α, (F) fully interdigitated gel L_β^{int}, (G) partially interdigitated gel, (H) mixed interdigitated gel. Reproduced from [58].

Depending on the temperature, the lipid bilayer can exhibit different phases [58], figure 1.4. In the liquid crystalline or fluid phase L_α the lipids are disordered and behave like a fluid. At low temperatures the lipids are in the gel phase L_β or $L_{\beta'}$. They are packed closely together and the tails show a high order. Since the lipids are stretched in this phase the bilayer thickness is much larger than in the fluid phase. In

the case of the L_β phase the tails are oriented along the bilayer normal, whereas in the $L_{\beta'}$ case the tails are tilted with respect to the bilayer normal. Between the fluid and the gel phase, the ripple phase $P_{\beta'}$ exists. In this phase the surface of the bilayer shows a ripple structure. The phase transition $P_{\beta'} \rightarrow L_\alpha$ is called main transition, whereas the transition $L_{\beta'} \rightarrow P_{\beta'}$ is called pre-transition.

1.2 Membrane Proteins

In general proteins are built from amino acids [24, 109]. Each amino acid, figure 1.5, consist of four groups: an amino (-NH_2) group, a carboxyl (-COOH) group, an H atom and a side chain R. In the α-amino acids the amino and the carboxyl group are attached to the same carbon atom – the α-carbon atom. The various α-amino acids differ in which side chain (R group) is attached to the α-carbon atom. Depending on the polarity of the side chain the amino acids vary in their hydrophilic or hydrophobic character. The amino acids of proteins are linked together by peptide bonds. These are amide bonds formed between the carboxyl group of one amino acid and the amino group of an adjacent amino acid. The binding between the amino acid is covalent. Depending on the number of amino acids in a sequence the molecule is called peptide or protein. Proteins can be described by four structures. The primary structure describes the amino acid sequence. The secondary structure describes the specific spatial arrangement of regularly repeated local structures stabilised by hydrogen bonds. Examples are α-helices and β-sheets. The tertiary structure describes the overall three-dimensional configuration of the protein. The following bond types are involved: ionic bonds, interpeptide hydrogen bonds, side-chain hydrogen bonds, disulfide covalent bonds. A protein is said to have a quaternary structure if it is composed of several polypeptide chains which are not covalently linked to one another. The distribution of hydrophilic and hydrophobic amino acids determines the tertiary structure of the protein, and their physical location on the outside structure of the proteins influences their quaternary structure.

Figure 1.5: Basic structure of the α-amino acids [109]. The four groups can be attached in two possible spatial configurations. These two configurations are mirror images of one another and labelled as L and D, respectively.

Any membrane protein that interacts directly with the hydrophobic core of the

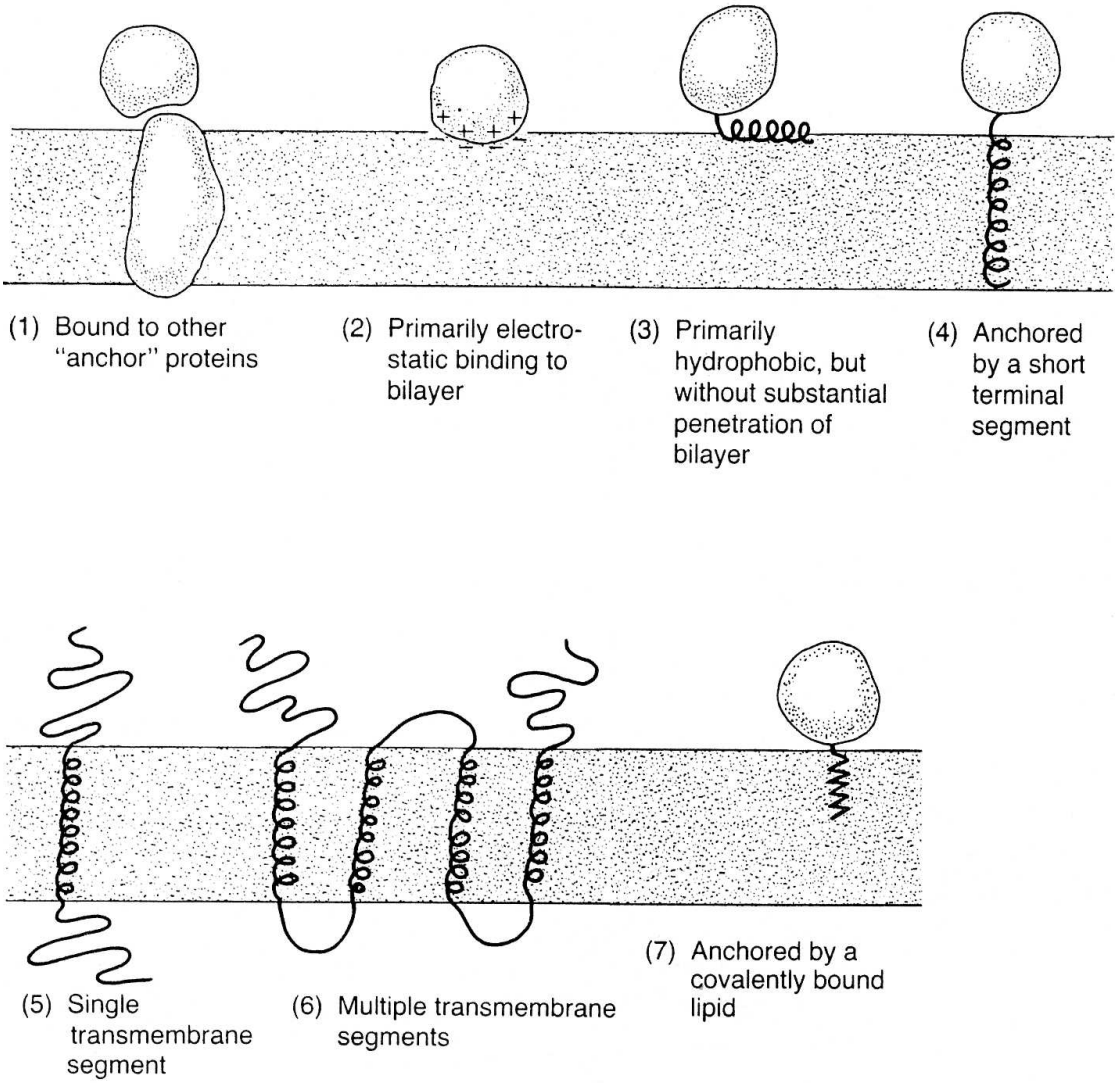

Figure 1.6: Schematic drawing of how proteins are attached to a lipid bilayer. Reproduced from [34].

lipid bilayer must be amphiphilic. The parts of the protein in contact with the aqueous environment are enriched with amino acids with polar and ionisable side chains, whereas the part of the protein in contact with the hydrophobic tails contains amino acids which are nonpolar.

Membrane proteins are classified as extrinsic or integral proteins, figure 1.6. The distinction between extrinsic and integral only gives information about the strength but not about the mode of attachment to the lipid bilayer. In general the proteins are bound to the lipid bilayer through hydrophobic or electrostatic interactions. The different ways how proteins are attached to the lipid bilayer are [34]:

(1) They interact with other proteins which are embedded in the lipid bilayer.

(2) They interact with the surface of the lipid bilayer.

(3)-(4) They interact with the lipid bilayer via a hydrophobic anchor or tail.

(5)-(6) Transmembrane proteins: They pass completely through the lipid bilayer once or many times.

(7) They are covalently bound to a lipid.

Integral proteins are so tightly bound to the membrane lipids that they can be freed only under denaturation conditions. Extrinsic proteins can be dissociated non-destructively from the membrane by relatively mild procedures.

1.3 Membrane-Protein Interactions

If one or more (transmembrane) proteins are incorporated into a lipid bilayer, this leads to perturbations within the lipid bilayer, figure 1.7. All the perturbations described in the following can generally be divided into symmetric and asymmetric perturbations. Symmetric perturbations leave the bilayer midplane unaffected and are for example caused by a cylindrical inclusion. The two monolayers experience the same deformation. If for example the inclusion has a cone-like structure, the perturbations are asymmetric. In this case the perturbations have to be described, beside other order parameters, in terms of the main curvature of the bilayer midplane [76].

If the length of the hydrophobic section of the protein is much smaller or much larger than the hydrophobic thickness of the lipid bilayer, this has a strong effect on the surrounding lipids and can also have an effect on the protein itself. This effect is called *hydrophobic mismatch*. One distinguishes between positive hydrophobic mismatch, if the hydrophobic length of the protein is much larger than the hydrophobic thickness of the lipid bilayer, and negative hydrophobic mismatch, if the hydrophobic length of the protein is much smaller than the hydrophobic thickness of the lipid bilayer. Even in the absence of hydrophobic mismatch proteins affect the lateral structure of the lipid bilayer: The number of possible conformations of the lipids is reduced in the vicinity of proteins, in addition proteins can induce a tilt of the lipid molecules. Proteins can induce a strong membrane curvature and last but not least affect the elastic properties of the membrane and thereby change the fluctuation spectrum of the membrane.

A hydrophobic mismatch may have consequences on the one hand for the protein properties and with this for the protein activity [26] and on the other hand for the lipid properties and with this for the membrane functionality. The unfavourable exposure of the hydrophobic surface of the protein to the water can be avoided through different scenarios [55]. The proteins may aggregate in order to minimise the hydrophobic area exposed to the water. In the case of positive hydrophobic mismatch the proteins may tilt in order to reduce the effective hydrophobic length. The protein may tilt as a whole or the individual helices of which the protein might be composed

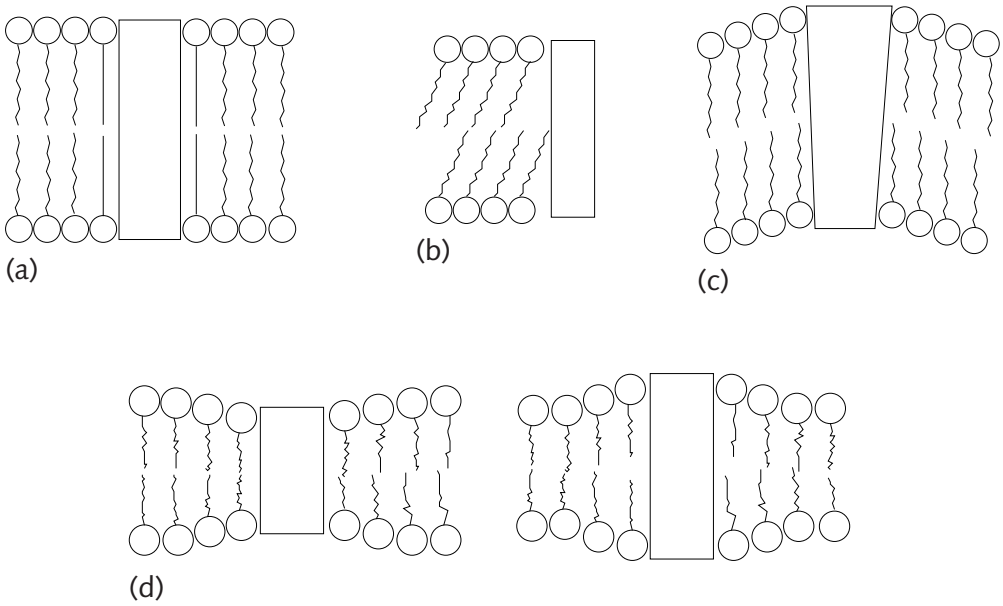

Figure 1.7: Protein-induced perturbations: (a) perturbation of the lipid conformation, (b) induced tilt of the lipids, (c) induced lateral curvature, (d) negative and positive hydrophobic mismatch.

may also experience a tilt [63]. In the case of negative hydrophobic mismatch the protein may not be incorporated into the lipid bilayer but instead localise at the surface. The protein might be deformed. There may be a change in the backbone conformation or the helices of the protein might change the organisation of their hydrophobic and hydrophilic side chains and thus adjust the hydrophobic length of the protein. Certainly both effects can occur. The lipids can change the membrane thickness by stretching or compressing their acyl chains. This also changes the local chain order in the lipid bilayer. The lipids can assemble into another type of aggregate. Proteins with a large hydrophobic section stabilise the gel phase, whereas proteins with a short hydrophobic length stabilise the fluid phase. Hydrophobic mismatch can also lead to non-lamellar phases, i.e. the inverted hexagonal phase. This can especially happen if the membrane contains a large amount of lipids which prefer non-lamellar phases.

An example of a protein being very sensitive to the bilayer thickness is gramicidin A [27, 57, 76]. It is a small 15-residue hydrophobic peptide, which forms dimeric channels for cations and water. The formation and lifetime of gramicidin A channels depend on the hydrophobic thickness of the membrane. An increase in the bilayer thickness reduces the mean channel lifetime. The function of gramicidin A has been investigated experimentally [27, 45, 57] as well as theoretically [46, 47, 48] using an elastic theory. Gramicidin A causes an increase in ordering of the neighbouring lipids.

The interaction between integral proteins is of great importance for the functionality of the membrane. On the one hand there are the direct protein-protein interactions, for example van der Waals forces and electrostatic forces for charged inclusions. The

van der Waals interactions are attractive and decrease with increasing distances between the proteins according to $1/R^6$. The electrostatic interactions are repulsive and decay exponentially with increasing distances between the proteins. Since the electrostatic interactions are shielded by the aqueous environment of the membrane [5, 117], they are often ignored in the analysis of protein-protein interactions. In general these direct interactions are short-range, acting over a few Ångströms. On the other hand the perturbation of the lipid bilayer by the proteins can induce indirect lipid-mediated interactions. The lipid-mediated interactions have a long-range contribution, acting over a few nanometres [12], if the inclusions couple to the local membrane curvature resulting in a suppression of long wavelength bilayer fluctuations, and a short-range contribution due to the local deformation of the lipid structure close to the protein. Both the lipid-mediated interactions between proteins included in the membrane and the influence of proteins on lipid bilayers have been intensively investigated for some time [7, 35, 76]. Chapter 2 focuses on the different theoretical models used to describe lipid-protein as well as lipid-mediated protein interactions.

In this thesis we want to investigate the influence of transmembrane proteins on the lipids on the one hand and the membrane-mediated interactions between transmembrane proteins on the other hand. In particular, we will investigate the influence of hydrophobic mismatch. For this analysis we use a coarse-grained model.

1.4 Coarse-Graining

Many systems are characterised by structures and processes on very different time and length scales and with a different number of degrees of freedom [6, 83]. Practically even with modern computers it is still impossible to simulate a model system on all time and length scales. One possibility to bypass this problem is to coarse-grain the model under consideration. The idea behind coarse-graining is to collect many microscopic degrees of freedom into fewer larger ones. Viewing a system at a coarser level has the advantage that on the one hand one reduces the computational cost, since unnecessary details are disregarded, and on the other hand the analysis of the system is faster. Long time scale processes are slower than processes on larger time scales. The reduction of degrees of freedom has the advantage that much larger time spans can be simulated. The different levels of coarse-graining are:

- *atomistic level*: The atomistic level is a realistic (atomistic) description of the system. All atoms of a molecule are considered.
- *microscopic level*: The structure of molecules is simplified.
- *mesoscopic level*: One considers minimal systems. Many atoms are combined to one particle.
- *macroscopic level*: One does not consider single particles any more, instead the system is described by continuum models.

Depending on the aim of the simulations it has to be decided what level of coarse-graining and what kind of simulation method, e.g. molecular dynamic, Monte Carlo or dissipative particle dynamic simulation, will be used.

Lipid and Protein Models

For the simulation of a pure lipid bilayer there is a big community of people involved in all-atom simulations [15, 21, 53, 54, 67, 68, 69, 70, 110, 111, 112]. The advantage of atomistic simulations is that they can be compared more directly to experiments. The length and time scale of pure lipids in atomistic simulations is very limited: about 10-30nm in length and hundreds of nanoseconds in time [4].

The lipid bilayer models dealing with the system on a mesoscopic level [10, 11, 13, 14, 38, 39, 90, 102] differ not only in the representation of the lipids and the used potentials but also in the representation of the aqueous environment. There are models that use explicit solvent beads [38, 39] and models which are solvent-free. In the latter type of models the hydrophobic interaction of the solvent is incorporated into the interactions of the lipid beads [10, 13, 14].

If proteins are inserted into the lipid bilayer, one also has to decide how these proteins will be modelled. The protein can be modelled on an atomistic level [42, 43, 110] or on a mesoscopic level. The protein models on the mesoscopic level differ much from each other [11, 41, 46, 82, 89, 99, 106].

Previous Coarse-Grained Simulations of Lipid-Protein Interactions

The first computer simulations on lipid-mediated protein interactions were done by Sintes and Baumgärtner in 1997 [103, 104, 105, 106]. They used a coarse-grained membrane model with two cylindrical inclusions embedded in a lipid bilayer using Monte Carlo simulation methods. They found that the inclusions exhibit two types of attraction forces – short-range and long-range forces. Up to distances of the diameter of the lipids the cylinders feel a depletion-induced attraction. The reason for this interaction is that because of the spatial interaction between the lipids and the inclusions, the inclusions are surrounded by a depletion zone. When the depletion zones of the two inclusions overlap, this gives an extra free volume for the lipids and therefore an attractive force. At larger distances the inclusions feel a fluctuation-induced attraction. The two regions are separated by a repulsive barrier for protein distances somewhat larger than the lipid diameter. The fluctuation-induced attractive force is related to the density and orientational fluctuations of the lipids. The density is not only reduced in the depletion zone but it also decreases with increasing distance.

Brannigan and Brown [10] construct their proteins as a rigid assembly of coarse-grained lipids: one hydrophilic bead, one interface bead and a different number of hydrophobic beads. The thickness and length of the proteins are adapted by changing the number of lipid chains, and the number of hydrophobic beads in the lipid chains, respectively. They compare the thickness profiles obtained for a lipid bilayer in the

vicinity of one protein to an elastic theory. With this elastic theory they calculate the effective interaction between two proteins inserted into the lipid bilayer.

De Meyer et al. [19] use a combination of dissipative particle dynamics methods and Monte Carlo methods and Schmidt et al. [99] use dissipative particle dynamics methods to simulate the coarse-grained model. The proteins are constructed by linking together chains with one hydrophilic bead and a certain number of hydrophobic beads. The thickness and length of the proteins are adapted by changing the number of chains, and the number of hydrophobic beads in the chains, respectively. De Meyer et al. calculate the effective interaction potential between two proteins with umbrella sampling methods as a function of the diameter and the length of the proteins. Schmidt et al. integrate the force between two proteins in order to determine the effective pair potential.

1.5 Present Work

This thesis is organised as follows. In chapter 2 we focus on the different theories that exist in order to explain lipid-protein interaction from a theoretical point of view. Chapters 3 and 4 introduce the model and the methods we use for our simulations. In chapter 5 we analyse some characteristics of a pure lipid bilayer. In chapters 6 and 7 we present the results of incorporating one and two proteins into the lipid bilayer, respectively. The results obtained from the computer simulations are compared to two theories described in chapter 2.

2 Theories on Lipid-Protein Interactions

When a protein is inserted into a lipid bilayer, this can lead to different distortion effects in the bilayer. On the one hand there is a change in the conformations of the lipids surrounding the protein. This even happens in the case of zero hydrophobic mismatch, i.e. if the size of the hydrophobic part of the protein matches the hydrophobic thickness of the lipid bilayer bilayer [76]. On the other hand, in the case of positive or negative hydrophobic mismatch, there may be structural changes of the lipids. I.e. the lipids get stretched or compressed, which changes, for example, the area per lipid.

The perturbation of the lipid conformation induced by a protein can be characterised by an order parameter. The order parameter measures the protein-induced perturbation in lipid order and can be realised by different quantities, for example the hydrophobic thickness, the bilayer area or the average acyl-chain orientational order parameter [81]. Far away from the protein the order parameter is equal to the order parameter measured in an undisturbed lipid bilayer. The distance over which the order parameter is affected by the inclusion is described by the correlation length.

In this chapter we summarise different theories used to describe lipid-protein interactions and lipid-mediated protein-protein interactions.

2.1 Mean Field Theory

The first theoretical study of lipid-mediated protein interactions was done by Marčelja in 1976 [74] using mean field methods. He assumed that the structure of the neighbouring lipids is disturbed by an integral protein [73] and furthermore that the length of the inclusion fits the thickness of the lipid bilayer (no hydrophobic mismatch). The lipid chains are arranged on a two-dimensional hexagonal lattice, whereas each lipid occupies one lattice site. The order parameter n_j at each lattice site j is defined as

$$n_j = \left\langle \frac{1}{n} \sum_{m=1}^{n} \left(\frac{3}{2} \cos^2 \nu_m - \frac{1}{2} \right) \right\rangle \quad . \tag{2.1}$$

n is the number of chain segments and ν_m describes the orientation of each chain segment. The influence of the proteins on the surrounding lipids is expressed by an explicit lipid-protein interaction contribution to the total energy of the system. Marčelja found that up to three layers of neighbouring lipids are disturbed by the protein. With increasing distance to the protein the disturbance effect decreases. In a system containing two proteins, each of the proteins perturbs the structure of

the surrounding lipids. If the two proteins are close together or in contact, the total perturbation of the surrounding lipids is decreased, because the regions with the disturbed lipids overlap. This lowers the free energy and causes an attractive force between the proteins. Depending on the relative strength of the direct protein-protein interaction in comparison to the lipid-protein interaction the proteins are separated by a layer of lipids or come into contact.

Schröder [100] assumed a lipid continuum to describe the lipid-mediated protein interaction. The order parameter is taken to be the average of the second Legendre polynom

$$\eta_j = \langle P_2(\nu) \rangle \quad , \tag{2.2}$$

where ν describes the orientation. The fluctuations of the chain-order parameter are decreased near the protein. Schröder derived an expression for the effective interaction between two proteins: This potential is attractive as long as the proteins have the same effect on the surrounding lipids. With increasing correlation length the range of the effective interaction is increased.

2.2 Landau-de Gennes Theory

A very old approach to study lipid-protein interactions is the Landau-de Gennes theory. In this theory the free energy is expanded in terms of an order parameter ϕ [51, 53, 91, 92, 94]. The free energy $\mathcal{F}$ can be expressed as a function of ϕ and the deviation of ϕ from its equilibrium value ϕ_0 [94]:

$$\mathcal{F}_{LdG} = \int d^2r \, \frac{c}{2} (\nabla\phi)^2 + \frac{a}{2} (\phi - \phi_0)^2 \quad . \tag{2.3}$$

The first term accounts for the cost of spatial variations in ϕ. The last term represents the restoring force tending to keep ϕ at its equilibrium value ϕ_0. The variable c is taken to be positive. Minimising the free energy yields the equation

$$\left(\xi^2 \nabla^2 - 1\right) \phi(r) + \phi_0 = 0 \quad . \tag{2.4}$$

$\xi = \sqrt{c/a}$ is the correlation length. Assuming the boundary conditions

$$\phi(r \to \infty) = \phi_0 \tag{2.5}$$

$$\phi(R) = \phi_R \tag{2.6}$$

with R the radius of the inclusion, the solution of equation 2.4 is

$$\phi(r) = \phi_0 + (\phi_R - \phi_0) \frac{K_0(r/\xi)}{K_0(R/\xi)} \quad . \tag{2.7}$$

K_0 is the zeroth Bessel function of the second kind. For large values of r/ξ the Bessel function can be replaced by its asymptotic function and equation 2.7 can be approximated by

$$\phi(r) = \phi_0 + (\phi_R - \phi_0) \sqrt{R/r} \, e^{\left(-\frac{r-R}{\xi}\right)} \quad . \tag{2.8}$$

The order parameter can be quite versatile. Owicki et al. [91, 92] defined the order parameter in terms of the area per molecule. Jähnig [51] defined the order parameter in terms of a lipid order parameter that takes into account the lipid orientation. A very popular order parameter is the thickness of the lipid bilayer. Since the order of the lipid chains is connected to the bilayer thickness, an integral protein induces local variations not only in the conformational order of the lipids but also in the bilayer thickness [108].

We use ϕ to describe the local variations of the monolayer thickness from its equilibrium value t_0, the value of the monolayer thickness of an undisturbed lipid bilayer. In this case $\phi_0 = 0$ and the two boundary conditions, equations 2.5 and 2.6, take the form $\phi(r \to \infty) = 0$ and $\phi(R) = t_R$.

The exponential law, equation 2.8, has been used quite often to fit thickness profiles obtained from simulations or molecular theories for membranes with a single inclusion [28, 29, 41, 99, 108, 115, 116].

2.3 Elastic Theory

A very powerful tool for describing lipid-protein interactions is the elastic theory of coupled monolayers. The idea is to introduce a certain number of order parameters representing elastic degrees of freedom. The perturbation of these order parameters with respect to their equilibrium value is evaluated by expressing the free energy as an expansion in terms of the order parameters [76].

Different authors have introduced different elastic theories [3, 10, 16, 17, 18, 46, 47, 48, 49, 87, 88, 101]. These theories differ mainly in the number of elastic terms they include and in the boundary conditions. All these theories have in common that the monolayer deformation is described in terms of the local monolayer thickness.

We will focus on the most recent theory by Brannigan and Brown [10]. The free energy of thickness deformations can be expressed as

$$\mathcal{F}_0 = \int_R^L d^2r \left\{ \frac{k_A}{2t_0^2}\phi^2 + 2k_c c_0 \nabla_r^2\phi + 2k_c \frac{\zeta}{t_0}\phi\nabla_r^2\phi + \frac{k_c}{2}\left(\nabla_r^2\phi\right)^2 + k_G \det\left(\partial_{ij}\phi\right) \right\} \quad . \tag{2.9}$$

$\phi + t_0$ is the locally smoothed monolayer thickness with t_0 being the equilibrium value. k_A is the compressibility modulus and $\zeta = c_0 - c_0'\Sigma_0$ is an extrapolated curvature with $c_0' = \partial c_0/\partial\Sigma|_{\Sigma=\Sigma_0}$. Σ is the area per lipid and Σ_0 is the equilibrium value of the area per lipid of an undisturbed lipid bilayer. k_c is the bending rigidity and indicates the energy cost of deviating from the spontaneous curvature c_0. The spontaneous curvature characterises the tendency and the magnitude of the monolayer head-tail interface to curve to or from the water phase [16]. Bilayer-forming lipids have zero spontaneous curvature, whereas non-bilayer forming lipids have a positive or negative spontaneous curvature. Dan et al. [17] showed that an inclusion decouples the two monolayers of a bilayer resulting in the fact that the spontaneous curvature of the amphiphiles dominates the thickness deformation profile and the membrane-induced

interaction between proteins. The last term in equation 2.9 takes into account the Gaussian curvature. The Gaussian rigidity k_G measures the energy cost of saddle-like deformations [96]. According to the Gauss-Bonnet theorem [95] the integral of the Gaussian curvature over closed surfaces is proportional to the Euler characteristics of this surface. In planar sheets this gives an uninteresting constant and thus is often omitted. However, surfaces containing inclusions are no longer closed. Brannigan and Brown showed that the membrane-mediated interactions between inclusions are strongly affected by the Gaussian curvature and thus has to be accounted for.

The inclusion of radius R is centred at $r = 0$. The monolayer thickness deformation at the surface of the inclusion is $\phi(R) = t_R$. The minimisation of the free energy, equation 2.9, with respect to the variation in the deformation profile $\phi(r)$ yields the Euler-Lagrange equation

$$\frac{k_A}{k_c t_0^2}\phi + \frac{4\zeta}{t_0}\nabla_r^2\phi + \nabla_r^4 t = 0 \tag{2.10}$$

with the boundary conditions

$$\phi(R) = t_R \tag{2.11}$$

$$\nabla_r^2\phi\Big|_R = -2\left(c_0 + \frac{\zeta}{t_0}t_R\right) - \frac{k_G}{k_c R}t'_R \tag{2.12}$$

$$\partial_r\phi\Big|_L = 0 \tag{2.13}$$

$$\nabla_r^3\phi\Big|_L = 0 \quad , \tag{2.14}$$

where $\partial_r = \partial/\partial r$, $\nabla_r^2 = (1/r)\partial_r r\partial_r$, $\nabla_r^3 = \partial_r\nabla_r^2$, and $t'_R = \partial_r\phi|_R$. The boundary condition 2.11 is the thickness matching condition: The height of the bilayer at the inclusion is equal to the inclusion height. The boundary condition 2.13 indicates that the lipids far away from the inclusions are not disturbed and therefore the thickness of the bilayer is equal to the thickness of an undisturbed bilayer. The boundary conditions 2.12 and 2.14 result from the minimisation of the free energy. For a single inclusion the solution of equation 2.10 is

$$\phi(r) = a_1 J_0(\alpha_+ r) + a_2 Y_0(\alpha_+ r) + a_3 J_0(\alpha_- r) + a_4 Y_0(\alpha_- r) \tag{2.15}$$

with

$$\alpha_\pm = \sqrt{2\frac{\zeta}{t_0} \pm \sqrt{\left(2\frac{\zeta}{t_0}\right)^2 - \frac{k_A}{k_c t_0^2}}} \quad . \tag{2.16}$$

$J_0(x)$ and $Y_0(x)$ are the zeroth order Bessel function of the first and second kind, respectively. The deformation profile can be described by two characteristic length scales: The decay length $\gamma = 1/\mathrm{Im}(\alpha_\pm)$ and the wavelength $\lambda = 2\pi/\mathrm{Re}(\alpha_\pm)$.

The coefficients a_1 to a_4 are determined by the boundary conditions:

$$a_1 = -a_- Y_1(\alpha_+ L) \tag{2.17}$$
$$a_2 = \quad a_- J_1(\alpha_+ L) \tag{2.18}$$
$$a_3 = \quad a_+ Y_1(\alpha_- L) \tag{2.19}$$
$$a_4 = -a_+ J_1(\alpha_- L) \tag{2.20}$$

with

$$a_\pm = \frac{\left(-2\left(c_0 + \frac{\zeta}{t_0} t_R\right) + \alpha_\pm^2 t_R\right) b_0(\alpha_\pm) - \frac{k_G}{k_c R} t_R \alpha_\pm b_1(\alpha_\pm)}{-(\alpha_+^2 - \alpha_-^2) b_0(\alpha_-) b_0(\alpha_+) + \frac{k_G}{k_c R}\left(\alpha_+ b_0(\alpha_-) b_1(\alpha_+) - \alpha_- b_0(\alpha_+) b_1(\alpha_-)\right)} \tag{2.21}$$

and

$$b_0(\alpha_\pm) = Y_0(\alpha_\pm R) J_1(\alpha_\pm L) - Y_1(\alpha_\pm L) J_0(\alpha_\pm R) \tag{2.22}$$
$$b_1(\alpha_\pm) = Y_1(\alpha_\pm L) J_1(\alpha_\pm R) - Y_1(\alpha_\pm R) J_1(\alpha_\pm L) \quad . \tag{2.23}$$

Inserting equation 2.15 into equation 2.9 and performing the integration, we get the following equation for the free energy of the deformation:

$$\mathcal{F}_0 = \pi R k_c \left(t_R \nabla_r^3 \phi \Big|_R - 2\left(c_0 - \frac{\zeta}{t_0} t_R\right) t_R' \right) \tag{2.24}$$

$$\begin{aligned} &= \pi R k_c \Bigg(-\left(\alpha_+^3 t_R + 2\alpha_+\left(c_0 - \frac{\zeta}{t_0} t_R\right)\right) a_- b_1(\alpha_+) \\ &\qquad + \left(\alpha_-^3 t_R + 2\alpha_-\left(c_0 - \frac{\zeta}{t_0} t_R\right)\right) a_+ b_1(\alpha_-) \Bigg) \quad . \end{aligned} \tag{2.25}$$

In the elastic model used so far only changes in properties of the free bulk membrane, for example the area per lipid and the thickness, have been considered. However, inclusions may locally change the lipid properties, for example the lipid volume or the lipid ordering, which may in turn affect the elastic properties of the membrane. For varying lipid volume Brannigan and Brown [10] have demonstrated how such effects are incorporated into the theory. We want to adapt this in a more general way.

We consider some scalar quantity $q(r)$, which is distorted from its bulk value q_0 by the inclusion and locally alters the membrane properties. By symmetry there are two new terms in equation 2.9:

$$\mathcal{F}_{el} = \mathcal{F}_0 + \mathcal{F}_q \quad \text{with} \tag{2.26}$$
$$\mathcal{F}_q = \int_R^L d^2 r \left\{ K_1 \frac{\delta q(r)}{q_0} \phi + K_2 \frac{\delta q(r)}{q_0} \nabla_r^2 \phi \right\} \quad . \tag{2.27}$$

$\delta q(r)/q_0$ denotes the relative deviation of q. Assuming that $\delta\phi(r)$ decays to zero on a length scale which is much smaller than the characteristic length scale of the elastic profile we can write for the free energy $\mathcal{F}_q$, equation 2.27 (cf. appendix B):

$$\mathcal{F}_q = 2\pi t_R \int_R^L r dr K_1 \frac{\delta q(r)}{q_0} + 2\pi t_R' \int_R^L dr \frac{\delta q(r)}{q_0} \left(K_1 r(r - R) + K_2\right) \quad . \tag{2.28}$$

The extra terms change the boundary condition 2.12:

$$\begin{aligned}\nabla_r^2\phi\Big|_R &= -2\left(c_0 + \frac{\zeta}{t_0}t_R - \frac{1}{2k_cR}\int_R^L dr\frac{\delta q(r)}{q_0}(K_1 r(r-R)+K_2)\right) - \frac{k_G}{k_cR}t'_R \\ &= -2\left(\tilde{c}_0 + \frac{\zeta}{t_0}t_R\right) - \frac{k_G}{k_cR}t'_R \quad .\end{aligned} \tag{2.29}$$

The spontaneous curvature is renormalised by the local distortion $\delta q(r)$ according to

$$\tilde{c}_0 = c_0 - \frac{1}{2k_cR}\int_R^L dr\frac{\delta q(r)}{q_0}(K_1 r(r-R)+K_2) \quad . \tag{2.30}$$

The overall free energy of the deformation can now be written as

$$\mathcal{F}_{el} = \pi R k_c\left(t_R\nabla_r^3\phi\Big|_R - 2\left(\tilde{c}_0 - \frac{\zeta}{t_0}t_R\right)t'_R\right) + \text{const} \quad , \tag{2.31}$$

where the constant does not depend on the deformation profile.

Depending on the used parameters the membrane will either promote aggregation of the two proteins or a finite spacing between the proteins. In general this interaction is short-range.

2.4 Elastic Theory with Local Tilt

The elastic theories presented so far take into account only the main degree of freedom, the local thickness of the monolayers. A number of authors included another degree of freedom in their elastic theory, the local tilt of the lipid chains [8, 30, 31, 32, 75]. This is of interest, because on the one hand integral proteins can induce a perturbation of the lipids through their shape, and on the other hand the lipid tilt degree of freedom reduces the lipid perturbation close to proteins [76].

Fournier [30, 31] presented an equation for the free energy taking into account the membrane curvature and the lipid tilt in addition to the monolayer thickness:

$$\mathcal{F} = \int d^2r\frac{B}{2}u^2 + \frac{\lambda}{2}(\nabla u)^2 + c\mathbf{m}\nabla u + \frac{\kappa_t}{2}\mathbf{m}^2 + \frac{\kappa_s}{2}(\nabla\mathbf{m})^2 + \frac{K_s}{2}(\nabla\times\mathbf{m})^2 \quad . \tag{2.32}$$

$u(r)$ is the deviation in bilayer thickness and $\mathbf{m}(r)$ describes the molecular tilt difference. B corresponds to the chain stretching modulus and for the molecular tilt difference new elastic parameters are introduced: Tilt modulus κ_t, splay modulus κ_s, twist modulus K, c describes the coupling between the thickness and the tilt. Minimising the free energy equation in this case results in two equations, one for the thickness profile $u(r)$ and one for the tilt difference $\mathbf{m}(r)$.

The thickness mismatch induces an attraction between inclusions because of the overlap of the depletion zone of the inclusions. The tilt difference on the other hand induces a repulsion between like inclusions. Therefore inclusions producing no tilt difference show a tendency to aggregate while inclusions producing a non-zero tilt difference either repel each other or form two-dimensional crystals [30].

2.5 Integral Equation Theory

Lagüe et al. [60, 61, 62] used a hypernetted chain integral projected onto the two-dimensional space of the lipid bilayer plane. They assumed that the proteins are repulsive objects, which interact with the hydrocarbon chains via a repulsive potential but not with the polar headgroups. The perturbation affects only the lateral positions of the lipids. The hypernetted chain equation can be written in terms of a pair of coupled integral equations. In order to compute the lipid-mediated potential of mean force between two proteins one needs, beside the hypernetted chain equation, the equations for the direct potential between proteins, the direct protein-lipid correlation function for a single protein and a response function related to the density fluctuations of lipid chains in the undisturbed lipid bilayer.

The lipid-mediated interaction between two proteins was found to be non-monotonic. In the case of inclusions of small and medium radii it is repulsive at intermediate distances and attractive at short range. In the event of inclusions with a large radius it is repulsive over all distances.

2.6 Chain Packing Theory

A totally different approach is the mean field chain packing theory [28, 29, 44, 77, 78] which aims at calculating the deformation free energy as a function of the hydrophobic mismatch. The key quantity in this theory is the probability distribution of chain conformations, which any conformational property can be calculated from. The free energy is described separately for the head and tail groups. The contribution from the tail groups consists of an energetic and an entropic contribution. The distribution of chain conformations is derived by minimisation of the free energy subject to packing constraints and geometric boundary conditions. The contribution from the head groups is a function of the average area per chain and the interfacial curvature between the head groups and the aqueous solution. The chain term is a sum of two contributions. One of these terms is always positive, even in case of hydrophobic matching, and results from the loss of conformational entropy imposed by the presence of the protein. The other contribution is related to the fact that in the case of hydrophobic mismatch the lipids must either stretch or compress. The interaction free energy between a transmembrane protein and the surrounding lipids has a minimum in the case of hydrophobic matching.

2.7 Theory of Fluctuation-Induced Interactions

The last theory we want to present is the theory of fluctuation-induced interactions [12, 22, 23, 36, 37, 40, 56, 86, 93, 118]. In the elastic theories presented so far it was assumed that the elastic constants are uniform. The indirect interactions are short-range and arise from a deformation field induced by an inclusion. In this theory

the proteins couple to the local membrane curvature. The indirect long-range interactions fall off with $1/R^4$. At temperatures that are small relative to the bending energies (the low temperature regime) the thermal fluctuations are unimportant, the interaction is attractive or repulsive depending on the strength of the bending energies. The energy scale is set by the bending energies. When the thermal fluctuations of the membrane dominate, the fact that the fluctuation spectrum of the lipid bilayer is affected leads to an attractive interaction for inclusions, which are much more rigid than the surrounding membrane. For inclusions less rigid the interaction is attractive or repulsive. The energy scale is set by the temperature and is independent of the bending energies. The force, a Casimir force, is entropic and much larger for large distances than van der Waals or screened electrostatic forces. Kim et al. [56] showed that these curvature-mediated interactions are not pairwise additive. Chou et al. [12] showed that the Gaussian curvature affects protein-protein attractions as well as thermodynamics. Dommersnes and Fournier [22] have performed Monte Carlo simulations to study the collective behaviour of identical inclusions imposing a local curvature on the membrane. These simulations show a transition from compact clusters to aggregation on lines or circles.

2.8 Conclusions

In this section we have presented different theories to describe lipid-protein interactions. The local perturbation of the lipid structure leads to short-range interactions. If the proteins affect the fluctuation spectra, the interactions are long-range.

In chapter 6 we use the Landau-de Gennes theory and the elastic theory to describe the thickness deformation profile of a single protein. In chapter 7 the two theories are used to describe the lipid-mediated interaction between two proteins.

3 Coarse-Grained Model

In this chapter we present the coarse-grained membrane model we use for our simulations. We use a generic bilayer model based on a lipid representation by Düchs and Schmid [25] and a solvent model by Lenz and Schmid [65]. We have expanded the model to simulate coarse-grained proteins in form of simple rigid cylinders.

3.1 Bilayer Model

Our bilayer model consists of a self-assembled bilayer of lipids in a solvent environment [25]. Each lipid is represented by one head bead of diameter σ_h and six tail beads of diameter σ_t, figure 3.1. The head beads are slightly larger than the tail beads, $\sigma_h = 1.1\sigma_t$.

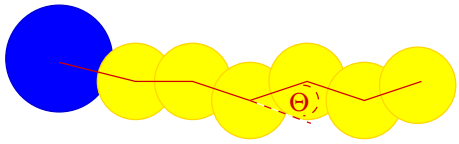

Figure 3.1: Sketch of the model lipid

Beads not connected with each other interact via a truncated and lifted Lennard-Jones potential:

$$U_{LJ,\,\text{lifted}}(r) = \begin{cases} U_{LJ}(r/\sigma) - U_{LJ}(r_c/\sigma) & \text{, if } r < r_c \\ 0 & \text{, otherwise} \end{cases} \tag{3.1}$$

with

$$U_{LJ}(r/\sigma) = \epsilon\left(\left(\frac{\sigma}{r}\right)^{12} - 2\left(\frac{\sigma}{r}\right)^{6}\right) \quad . \tag{3.2}$$

$r = |\mathbf{r}|$ is the distance between two interacting beads. The parameter σ is the mean value of the diameters of the interacting beads. Head-head and head-tail interactions are purely repulsive ($r_c = \sigma$) and tail-tail interactions also have an attractive component ($r_c = 2\sigma$). The adjacent beads of the lipid chain are bound to each other by a finite extensible nonlinear elastic potential (FENE potential):

$$U_{\text{FENE}}(r) = -\frac{1}{2}\epsilon(\Delta r_{\max})^2 \log\left(1 - \left(\frac{r - r_0}{\Delta r_{\max}}\right)^2\right) \quad . \tag{3.3}$$

bead-bead	ϵ	σ	r_c
head-head	1.0	1.1	1.0σ
head-tail	1.0	1.05	1.0σ
head-solvent	1.0	1.1	1.0σ
tail-tail	1.0	1.0	2.0σ
tail-solvent	1.0	1.05	1.0σ

Table 3.1: Parameters of the Lennard-Jones potential

$$\begin{array}{rl} U_{FENE}: & \epsilon = 100 \quad r_0 = 0.7 \quad \Delta r_{max} = 0.2 \\ U_{BA}: & \epsilon = 4.7 \end{array}$$

Table 3.2: Parameters of the bond-length and bond-angle potential

r_0 is the equilibrium bond length and Δr_{max} is the maximal deviation. This potential ensures that the bond length is always between $r_0 - \Delta r_{max} \leq r \leq r_0 + \Delta r_{max}$. Additionally, chains are given a bending stiffness by a bond-angle potential:

$$U_{BA}(\Theta) = \epsilon(1 - \cos(\Theta)) \quad . \tag{3.4}$$

Θ is the angle between three adjacent beads, figure 3.1. The tables 3.1 and 3.2 summarise the parameters we use for the different potentials for all our simulations.

The solvent environment is represented by explicit solvent beads [65]. They behave like unbound head beads, except for not interacting with each other. This kind of solvent model has the advantage of being computationally cheap. Only solvent beads close to the lipid bilayer contribute to the energy calculation. The lipid bilayer has the whole structure and flexibility, whereas the solvent cannot develop any internal structures. Physically, the solvent probes the accessible free volume on the length scale of the head beads. The lipid bilayer gets stabilised by the attractive interaction between the lipid tails and the entropic effect that the solvent has more accessible volume, if the lipids group together.

For the simulations the initial configuration is created by setting up a perfectly ordered bilayer in the xy-plane where the lipid chains point into the z-direction (the bilayer normal). Afterwards the system is simulated until it is equilibrated. The system is said to be equilibrated, when all observables fluctuate around its equilibrium value without showing any particular trend.

The model has two fundamental simulation units: The length unit σ_t and the energy unit ϵ. All quantities of the system can be expressed in these two units.

3.1.1 Bilayer Characterising Quantities

The bilayer thickness $2t$ and the height h of the bilayer midplane are defined as the difference and the average value of the average z-position of the head beads of the

upper and lower monolayer, respectively:

$$2t = \langle z \rangle_{\text{upper}} - \langle z \rangle_{\text{lower}} \tag{3.5}$$

$$h = \frac{1}{2}\left(\langle z \rangle_{\text{upper}} + \langle z \rangle_{\text{lower}}\right) \quad . \tag{3.6}$$

t is the monolayer thickness. The equilibrium monolayer thickness of an undisturbed lipid bilayer is denoted by t_0.

The area per lipid Σ is twice the area of the xy-plane divided by the number of lipids N in the system:

$$\Sigma = \frac{2L_x L_y}{N} \quad . \tag{3.7}$$

In this definition we assume that the number of lipids in both monolayers is equal. The equilibrium value of the area per lipid of an undisturbed lipid bilayer is denoted by Σ_0.

The bilayer thickness and the area per lipid are two values which are very well measurable in experimental membranes. We can therefore use these two quantities to convert the simulation units σ_t and ϵ to SI units. In the fluid phase the equilibrium bilayer thickness is $2t_0 = 6.1 \pm 0.05\sigma_t$ and the equilibrium area per lipid is $\Sigma_0 = 1.36 \pm 0.005\sigma_t^2$. The corresponding experimental values for DPPC are: $2t_0 = 39.2\text{Å}$ and $\Sigma_0 = 62.9\text{Å}^2$ [84]. If we compare the temperature of the main transition of our model, $k_B T_m = 1.2\epsilon$, $k_B = 1,3806504(24) \cdot 10^{-23}\text{J/K}$ the Boltzmann constant, with the corresponding experimental value for DPPC, $T_m = 42°C$ [58], we can identify an energy scale. The two conversion factors are: $\sigma_t = 6\text{Å}$ and $\epsilon \sim 0.36 \cdot 10^{-20}\text{J}$.

The end-to-end vector $\mathbf{l}$ of a lipid is defined as the difference vector between the head bead and the last tail bead. With this vector we can analyse the order of the lipids within the bilayer. The chain order parameter S_z shows how good the lipids are aligned to the z-axis:

$$S_z = \frac{1}{2}\left\langle 3\left(\frac{l_z}{l}\right)^2 - 1 \right\rangle \quad . \tag{3.8}$$

The norm of the end-to-end vector $l = |\mathbf{l}|$ is the chain length. l_z is the z-component of the end-to-end vector.

The overlap O of the two monolayers can be defined in two different ways. One possibility is to calculate the overlap according to monomer characteristics via an overlap integral:

$$O_I = \int_0^{L_z} \rho^{\text{tail}}_{\text{upper}}(z)\rho^{\text{tail}}_{\text{lower}}(z)\,dz \quad . \tag{3.9}$$

$\rho^{\text{tail}}_{\text{upper, lower}}$ is the density of the tail beads in the upper and lower monolayer, respectively. L_z is the length of the simulation box in z-direction. The other possibility is to define the overlap via chain characteristics [59]:

$$O_C = \frac{2(l_z - t)}{l_z} \quad . \tag{3.10}$$

l_z is the z-component of the end-to-end vector and t is the monolayer thickness defined in equation 3.5.

3.2 Protein Model

The proteins are modelled as rigid cylinders of diameter $\sigma_p = 3\sigma_t$ and correspond to simple β-helices. They are oriented along the z-axis, the bilayer normal, and are not allowed to tilt. In biological membranes this can be realised by an anchoring mechanism between the transmembrane proteins and the lipid bilayer.

The proteins are free to move in all three directions of the lipid bilayer, realised by a movement of the protein centre. The interaction is described by the repulsive part of the Lennard-Jones potential, equation 3.2, which is radially shifted by σ_0:

$$U_{rep,P}(r) = \begin{cases} U_{LJ}\left(\frac{r-\sigma_0}{\sigma}\right) - U_{LJ}(1) & \text{, if } r - \sigma_0 < \sigma \\ 0 & \text{, otherwise} \end{cases} . \tag{3.11}$$

Since the interaction between the proteins and the lipid and solvent beads is restricted to the xy-plane, $r = \sqrt{x^2 + y^2}$ is the distance in the xy-plane. This implies that the protein covers the whole length of the simulation box in z-direction. The proteins are repulsive (hydrophilic) over their whole length. The coefficients σ and σ_0 in equation 3.11 are defined as $\sigma = 0.5(\sigma_t + \sigma_i)$, $(i = h,t,s)$, $\sigma_0 = \sigma_t$ for bead-protein interactions and $\sigma = \sigma_t$, $\sigma_0 = 2\sigma_t$ for protein-protein interactions.

Additionally, the proteins attract the tail beads on a "hydrophobic" section of length L. This is described by another attractive potential, which depends on the z-distance between the tail bead and the protein centre:

$$U_{att,P}(r,z) = U_{attr}(r) \cdot W_P(z) \tag{3.12}$$

with

$$U_{attr}(r) = \begin{cases} U_{LJ}(1) - U_{LJ}(2) & \text{, if } r - \sigma_0 < \sigma \\ U_{LJ}\left(\frac{r-\sigma_0}{\sigma}\right) - U_{LJ}(2) & \text{, if } \sigma < r - \sigma_0 < 2\sigma \\ 0 & \text{, otherwise} \end{cases} \tag{3.13}$$

and $W_P(z)$ a weight function that is unity over a length $L - 2\sigma_t$ and slopes smoothly to zero:

$$W_P(z) = \begin{cases} 1 & \text{, if } |z| \leq l \\ \cos^2(1.5\,(|z| - l)) & \text{, if } l < |z| < l + \frac{\pi}{3} \\ 0 & \text{, otherwise} \end{cases} \tag{3.14}$$

with $l = L/2 - \sigma_t$. Table 3.3 outlines the coefficients we use for our simulations.

To summarise, the protein length is equal to the length of the simulation box in z-direction. On a length L the proteins are hydrophobic. Above and beyond this part the proteins are hydrophilic. Since the length of the simulation box fluctuates during the simulation (cf. chapter 4) the lengths of these two hydrophilic parts also fluctuate.

In the simulations two parameters are varied: the hydrophobic length L of the proteins and the parameter ϵ_{pt}. ϵ_{pt} tunes the strength of the lipid-protein interaction,

bead-protein	ϵ	σ	r_c	σ_0
head-protein	1.0	1.05	1.0σ	1.0
solvent-protein	1.0	1.05	1.0σ	1.0
tail-protein	1.0 ... 6.0	1.0	1.0σ	1.0
protein-protein	1.0	1.0	1.0σ	2.0

Table 3.3: Parameters of the Lennard-Jones potential for the bead-protein interactions

i.e. the hydrophobicity of the protein. In order to simulate proteins of different diameters we vary the parameter σ_0 while keeping all other parameters constant. To simulate a protein corresponding to a simple α-helix we set $\sigma_p = 1\sigma_t$ and $\sigma_0 = 0$.

3.2.1 Protein Model with Tilt

The orientation of the protein along the z-axis is a geometrical constraint. Especially in the case of hydrophobic mismatch it is interesting to study how the proteins behave to avoid the hydrophobic mismatch. In an extension of the protein model the proteins are allowed to tilt and rotate. The proteins are modelled as rigid sphero-cylinders with a finite length L and a direction $\mathbf{d}_P$, figure 3.2. The components of the direction vector are between zero and one with a length of the direction vector equal to one. If the z-component of the direction vector is one and the x- and y-component are zero the protein is oriented along the z-axis.

The interaction of the protein with the head, tail and solvent beads is realised according to the equations 3.11 and 3.12, where the distance is now calculated in three dimensions. The distance $r = \sqrt{x^2 + y^2}$ is replaced by the distance r_t and the z-distance z between tail beads and protein is substituted by r_p, figure 3.2. The distance vector $\mathbf{r}_t$ between each bead and the protein is defined as the shortest distance between the bead and the protein axis. In practice this is realised by calculating the perpendicular point F on the protein axis. If this point is outside of the protein, i.e. outside of the section L, the distance to the nearest end-point $L_{1,2} = P \pm \frac{L}{2}\mathbf{d}_P$ of the protein is calculated. P is the centre point of the protein. The distance vector $\mathbf{r}_p$ is defined as the connecting vector between the perpendicular point F and the centre of the protein P.

The tilt angle θ_P and the rotation angle ϕ_P of the protein are calculated according to

$$d_{P,x} = \sin(\theta_P)\cos(\phi_P) \tag{3.15}$$

$$d_{P,y} = \sin(\theta_P)\sin(\phi_P) \tag{3.16}$$

$$d_{P,z} = \cos(\theta_P) \quad . \tag{3.17}$$

In order to change the two angles the direction vector $\mathbf{d}_P$ is changed using an algorithm introduced by Marsaglia [71]. Two uniformly distributed random numbers r_1 and r_2 of the interval $(-1, 1)$ with $S = r_1^2 + r_2^2 < 1$ are generated. The direction vector

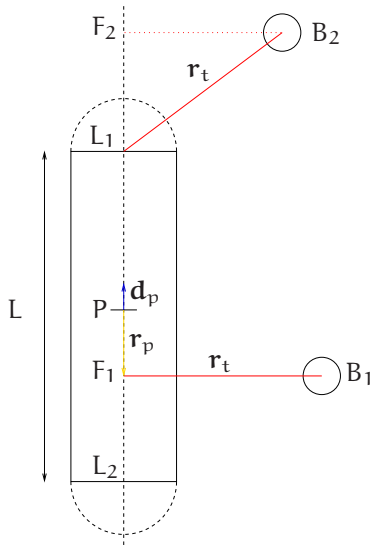

Figure 3.2: Distance calculation if the protein of length L is allowed to tilt and rotate. P is the centre of the protein. $\mathbf{d}_P$ is the direction vector. The distance vector $\mathbf{r}_t$ is the shortest distance between the protein and the bead B: The perpendicular point F of each bead B and the protein axis is calculated. If F is outside of the protein, the distance between the bead and the nearest end-point of the protein, L_1 or L_2, is calculated, as in the case of bead B_2. The distance vector $\mathbf{r}_p$ is the connecting vector between P and F.

$\mathbf{d}_P$ is changed according to

$$d_{P,x} = d_{P,x} + 2r_1\sqrt{1-S} \cdot \Delta \tag{3.18}$$

$$d_{P,y} = d_{P,y} + 2r_2\sqrt{1-S} \cdot \Delta \tag{3.19}$$

$$d_{P,z} = d_{P,z} + 1 - 2S \cdot \Delta \tag{3.20}$$

with Δ the tilt range. Afterwards the direction vector is normalised to one.

4 Methods

The system is simulated using Monte Carlo methods at constant pressure P, temperature T and particle number N with periodic boundary conditions in a simulation box of variable size and shape. The simulation box is a parallelepiped spanned by the vectors $(L_x,0,0)$, $(s_{yx}L_x,L_y,0)$, $(s_{zx}L_x,s_{zy}L_y,L_z)$. All L_i and s_j are allowed to fluctuate. The fluctuation of the simulation box guarantees that the membrane is tension-free. This can be ensured by calculating the pressure tension. When the simulation box changes its shape the bead coordinates are rescaled accordingly. The calculation of the distance vector $\mathbf{r}_{ij}$ between two particles i and j is done according to the minimum image convention, i.e. the distance between i and the nearest picture of particle j, with respect to the boundary condition, is calculated. The programme is parallelised using a geometrical decomposition scheme.

4.1 Monte Carlo Simulations

The idea behind Monte Carlo simulations [33] is to compute thermal averages of an observable A of a system in equilibrium:

$$\langle A\rangle = \frac{\int d\mathbf{r}^N A\left(\mathbf{r}^N\right)\exp\left(-\beta\mathcal{U}\left(\mathbf{r}^N\right)\right)}{\int d\mathbf{r}^N \exp\left(-\beta\mathcal{U}\left(\mathbf{r}^N\right)\right)} \quad . \tag{4.1}$$

$\mathcal{U}$ is the potential energy and $\beta = (k_B T)^{-1}$ with T the temperature of the system and k_B the Boltzmann constant.

The algorithm for our Monte Carlo simulations works according to the following simple scheme. The moves are accepted with respect to the Metropolis criterion:

1. Select a bead at random. Calculate its energy $\mathcal{U}(\mathbf{r})$.

2. Move the bead by a random displacement $\mathbf{r}' = \mathbf{r} + \mathbf{d}r$. Calculate its new energy $\mathcal{U}(\mathbf{r}')$.

3. Accept the move from $\mathbf{r}$ to $\mathbf{r}'$ with probability

$$\mathrm{acc}(o \to n) = \min\left(1, \exp\left\{-\beta\left[\mathcal{U}(\mathbf{r}') - \mathcal{U}(\mathbf{r})\right]\right\}\right) \quad . \tag{4.2}$$

x. Every x steps do a volume and/or a shear move. Calculate the old energy $U(\mathbf{r}^N,V)$.

Volume move: Change the length L_i by dl_i, $L'_i = L_i + dl_i$. All particle positions are rescaled $r_i = r_i \cdot (1.0 + dl_i/L_i)$.

Shear move: Change the shift s_{ji} by ds_{ji}, $s'_{ji} = s_{ji} + ds_{ji}$. All particle positions are sheared $r_j = r_j + r_i \cdot ds_{ji} L_i/L_j$.

Calculate the new energy $U(\mathbf{r}'^N, V')$. Accept the change according to

$$\begin{aligned} \text{acc}(o \to n) = \min\Big(1, \exp\Big\{-\beta\Big[\mathcal{U}(\mathbf{r}^N, V') - \mathcal{U}(\mathbf{r}^N, V) \\ + P(V' - V) - N\beta^{-1}\ln(V'/V)\Big]\Big\}\Big) \quad . \end{aligned} \tag{4.3}$$

The move ranges $d\mathbf{r}$ of the beads and the change ranges dl and ds of the simulation box are chosen so that the acceptance rate is about 30%.

4.2 Pressure Profile

For a system in equilibrium the internal pressure must be equal to the external pressure acting on the system. This can be ensured by calculating the pressure tensor of the system. For example in dissipative particle dynamics simulations the calculation of the pressure tensor can be used to check, if the time step is of appropriate size [2, 52].

The pressure tensor of a system with N particles and a volume V at a temperature T consists of a kinetic part $\mathcal{P}^{kin}$ and a potential part $\mathcal{P}^U$ [107, 114]:

$$\mathcal{P} = \mathcal{P}^{kin} + \mathcal{P}^U \quad . \tag{4.4}$$

The kinetic part can be expressed by a generalisation of the ideal gas law:

$$\mathcal{P}^{kin} = \frac{N k_B T}{V} \underline{1} \quad . \tag{4.5}$$

$\underline{1}$ is the 3×3 unity matrix. The potential part is obtained from the virial theorem [33]:

$$\mathcal{P}^U_{\alpha\beta} = -\left\langle \frac{1}{V} \sum_{i=1}^{N} r_i^\alpha \frac{dU}{dr_i^\beta} \right\rangle \tag{4.6}$$

$$= \left\langle \frac{1}{V} \sum_{i=1}^{N} r_i^\alpha F_i^\beta \right\rangle \tag{4.7}$$

$$= \left\langle \frac{1}{V} \sum_{i<j} r_{ij}^\alpha F_{ij}^\beta \right\rangle \quad , \tag{4.8}$$

where $\mathbf{r}_i$ is the position of particle i and $\mathbf{F}_i = \sum_{j,i\neq j} \mathbf{F}_{ij}$ is the total force acting on that particle. If using periodic boundary conditions it is better not to use the absolute

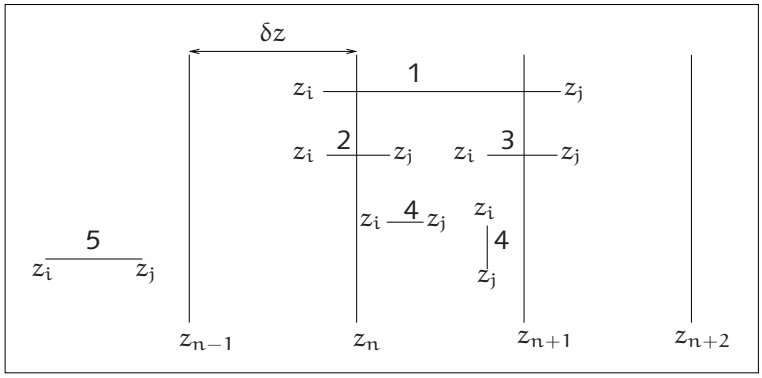

Figure 4.1: Pressure profile – illustration of the pressure distribution according to the Irving-Kirkwood convention

positions of the particles but the distance vector $\mathbf{r}_{ij} = \mathbf{r}_i - \mathbf{r}_j$ between particles i and j. This distance vector is calculated according to the minimal image convention. In the above equations we have used the following relation between force and potential:

$$\mathbf{F}_{ij} = \mathbf{F}(\mathbf{r}_{ij}) = -\frac{dU(|\mathbf{r}_i - \mathbf{r}_j|)}{d\mathbf{r}_{ij}} = -\frac{dU(|\mathbf{r}_i - \mathbf{r}_j|)}{d\mathbf{r}_i} = \frac{dU(|\mathbf{r}_i - \mathbf{r}_j|)}{d\mathbf{r}_j} \quad . \tag{4.9}$$

For the force we assume that all interactions in the system can be reduced to pair interactions $\mathbf{F}_{ij} = -\mathbf{F}_{ji}$.

In an equilibrated system the non-diagonal elements of the pressure tensor vanish and the diagonal elements are equal to the applied pressure P. In order to calculate the local distribution of the pressure in a system $\mathcal{P}(\mathbf{r})$, we use the ansatz by Irving and Kirkwood [50]. Since the system is rotationally symmetric around the z-axis, the pressure tensor only depends on the position z. The system is divided along the z-axis into s slices with width $\delta z = L_z/s$. L_z is the length of the simulation box in z direction. The pressure contribution in slice n, extending from z_n to z_{n+1}, is:

$$\mathcal{P}^n_{\alpha\beta} = \left\langle \frac{N_n}{V_n} \right\rangle k_B T \, \delta_{\alpha\beta} + \left\langle \frac{1}{V_n} \sum_{i<j} r^\alpha_{ij} \, F^\beta_{ij} \cdot I_n \right\rangle \quad . \tag{4.10}$$

N_s is the number of particles in slice s. The volume V_s of slice s is $V_s = L_x L_y \delta z$, where L_x and L_y are the lengths of the simulation box in x- and y-direction, respectively. The function I_n is a weight function and expresses the contribution of $z_{ij} = z_i - z_j$ to slice n, figure 4.1. We assume that $z_i < z_j$:

$$I_n = \begin{cases} (z_{n+1} - z_n)/z_{ij} & z_i \le z_n \;\&\; z_j \ge z_{n+1} \text{ (case 1)} \\ (z_j \quad - z_n)/z_{ij} & z_i < z_n \;\&\; z_n < z_j < z_{n+1} \text{ (case 2)} \\ (z_{n+1} - z_i)/z_{ij} & z_n < z_i < z_{n+1} \;\&\; z_j > z_{n+1} \text{ (case 3)} \\ 1 & z_n < z_i \le z_j < z_{n+1} \text{ (case 4)} \\ 0 & \text{else (case 5)} \end{cases} \quad . \tag{4.11}$$

In our simulations we have three different kind of potentials. The Lennard-Jones potential (equation 3.1) and the FENE-potential (equation 3.3) are pair interactions. The resulting forces are

$$\mathbf{F}_{\mathrm{LJ,lifted}}(\mathbf{r}_{ij}) = \begin{cases} 12\frac{\epsilon}{\sigma}\left(\left(\frac{\sigma}{r_{ij}}\right)^{13} - \left(\frac{\sigma}{r_{ij}}\right)^{7}\right)\frac{\mathbf{r}_{ij}}{r_{ij}} & \text{, if } r_{ij} < r_c \\ 0 & \text{, otherwise} \end{cases} \tag{4.12}$$

and

$$\mathbf{F}_{\mathrm{FENE}}(\mathbf{r}_{ij}) = -\epsilon \frac{1}{1-\left(\frac{r_{ij}-r_0}{\Delta r_{max}}\right)^2}(r_{ij}-r_0)\frac{\mathbf{r}_{ij}}{r_{ij}} \quad . \tag{4.13}$$

The bond-angle potential is a three-particle potential. The bond angle between three adjacent beads i, j and k is

$$\cos(\Theta) = \frac{\mathbf{r}_{ji}\mathbf{r}_{jk}}{|\mathbf{r}_{ji}||\mathbf{r}_{jk}|} \tag{4.14}$$

with $\mathbf{r}_{ji} = \mathbf{r}_j - \mathbf{r}_i$ and $\mathbf{r}_{jk} = \mathbf{r}_j - \mathbf{r}_k$. With equation 4.14 the bond-angle potential (equation 3.4) between the beads i, j and k can be written as

$$U_{ijk} = \epsilon\,(1+\cos(\Theta_{ijk})) = \epsilon\left(1+\frac{\mathbf{r}_{ji}\cdot\mathbf{r}_{jk}}{|\mathbf{r}_{ji}||\mathbf{r}_{jk}|}\right) \quad . \tag{4.15}$$

The resulting forces on the beads i, j and k are:

$$\mathbf{F}_i = -\frac{dU_{ijk}}{dr_i} = \frac{\epsilon}{|\mathbf{r}_{ji}||\mathbf{r}_{jk}|}\left(\mathbf{r}_{jk} - \mathbf{r}_{ji}\cdot\mathbf{r}_{jk}\frac{\mathbf{r}_{ji}}{|\mathbf{r}_{ji}|^2}\right) = \frac{dU_{ijk}}{dr_{ji}} =: -\mathbf{F}_{ji} \quad , \tag{4.16}$$

$$\mathbf{F}_j = -\frac{dU_{ijk}}{dr_j} = \frac{-\epsilon}{|\mathbf{r}_{ji}||\mathbf{r}_{jk}|}\left(\mathbf{r}_{ji}+\mathbf{r}_{jk} - \mathbf{r}_{ji}\cdot\mathbf{r}_{jk}\left(\frac{\mathbf{r}_{ji}}{|\mathbf{r}_{ji}|^2}+\frac{\mathbf{r}_{jk}}{|\mathbf{r}_{jk}|^2}\right)\right) \quad , \tag{4.17}$$

$$\mathbf{F}_k = -\frac{dU_{ijk}}{dr_k} = \frac{\epsilon}{|\mathbf{r}_{ji}||\mathbf{r}_{jk}|}\left(\mathbf{r}_{ji} - \mathbf{r}_{ji}\cdot\mathbf{r}_{jk}\frac{\mathbf{r}_{jk}}{|\mathbf{r}_{jk}|^2}\right) = \frac{dU_{ijk}}{dr_{jk}} =: -\mathbf{F}_{jk} \quad . \tag{4.18}$$

The contribution of the bond-angle potential of the beads i, j and k to the pressure tensor is

$$\mathcal{P}^{U,\,BA}_{\alpha\beta} = \frac{1}{V}\left(r_i^\alpha F_i^\beta + r_j^\alpha F_j^\beta + r_k^\alpha F_k^\beta\right) \tag{4.19}$$

$$\begin{aligned} &= \frac{-\epsilon}{V|\mathbf{r}_{ji}||\mathbf{r}_{jk}|}\Bigg((r_j^\alpha - r_i^\alpha)r_{jk}^\beta - \frac{\mathbf{r}_{ji}\cdot\mathbf{r}_{jk}}{|\mathbf{r}_{ji}|^2}(r_j^\alpha - r_i^\alpha)r_{ji}^\beta \\ &+ \qquad (r_j^\alpha - r_k^\alpha)r_{ji}^\beta - \frac{\mathbf{r}_{ji}\cdot\mathbf{r}_{jk}}{|\mathbf{r}_{jk}|^2}(r_j^\alpha - r_k^\alpha)r_{jk}^\beta\Bigg) \end{aligned} \tag{4.20}$$

$$= \frac{-\epsilon}{V|\mathbf{r}_{ji}||\mathbf{r}_{jk}|}\left(r_{ji}^\alpha r_{jk}^\beta - \frac{\mathbf{r}_{ji}\cdot\mathbf{r}_{jk}}{|\mathbf{r}_{ji}|^2}r_{ji}^\alpha r_{ji}^\beta + r_{jk}^\alpha r_{ji}^\beta - \frac{\mathbf{r}_{ji}\cdot\mathbf{r}_{jk}}{|\mathbf{r}_{jk}|^2}r_{jk}^\alpha r_{jk}^\beta\right) \tag{4.21}$$

$$= \frac{1}{V}\left(r_{ji}^\alpha F_{ji}^\beta + r_{jk}^\alpha F_{jk}^\beta\right) \quad . \tag{4.22}$$

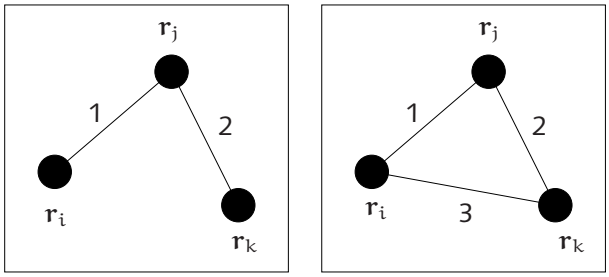

Figure 4.2: Distribution of the bond-angle potential according to (a) Irving-Kirkwood and (b) Götz-Lipowsky

Thus the three-particle interactions can be reduced to pair interactions. In order to distribute the contribution $\mathbf{r}_{ji} \otimes \mathbf{F}_{ji} + \mathbf{r}_{jk} \otimes \mathbf{F}_{jk}$ to the local pressure profile, we have two possibilities, figure 4.2:

(a) We use the Irving-Kirkwood convention and distribute the contribution on the two bonds 1 and 2:

1: $\mathbf{F}_i \otimes (\mathbf{r}_i - \mathbf{r}_j) = \mathbf{F}_{ji} \otimes \mathbf{r}_{ji}$
2: $\mathbf{F}_k \otimes (\mathbf{r}_k - \mathbf{r}_j) = \mathbf{F}_{jk} \otimes \mathbf{r}_{jk}$.

(b) We use an alternative way by Götz and Lipowsky [39] and distribute the contribution on the three bonds 1, 2 and 3:

1: $\frac{1}{3}(\mathbf{F}_i - \mathbf{F}_j) \otimes (\mathbf{r}_i - \mathbf{r}_j) = \frac{1}{3}(2\mathbf{F}_{ji} + \mathbf{F}_{jk}) \otimes \mathbf{r}_{ji}$
2: $\frac{1}{3}(\mathbf{F}_j - \mathbf{F}_k) \otimes (\mathbf{r}_j - \mathbf{r}_k) = \frac{1}{3}(2\mathbf{F}_{jk} + \mathbf{F}_{ji}) \otimes \mathbf{r}_{jk}$
3: $\frac{1}{3}(\mathbf{F}_i - \mathbf{F}_k) \otimes (\mathbf{r}_i - \mathbf{r}_k) = \frac{1}{3}(\mathbf{F}_{ji} - \mathbf{F}_{jk}) \otimes \mathbf{r}_{ki}$.

In the equations above we have used the following identities:

$$\begin{aligned} \mathbf{F}_i &= -\mathbf{F}_{ji} \\ \mathbf{F}_k &= -\mathbf{F}_{jk} \\ \mathbf{F}_j &= -\mathbf{F}_i - \mathbf{F}_k = \mathbf{F}_{ji} + \mathbf{F}_{jk} \quad . \end{aligned} \tag{4.23}$$

We will see later that the difference between the results obtained with the two distributions is negligible.

4.3 Parallelisation

Our programme is parallelised with MPI [79] using a geometrical decomposition scheme [97, 113]. The idea is to define *active regions* represented by the light blue areas in figure 4.3. Each processor gets one of these active regions. The distance between the regions is slightly larger than the maximum interaction range of the beads.

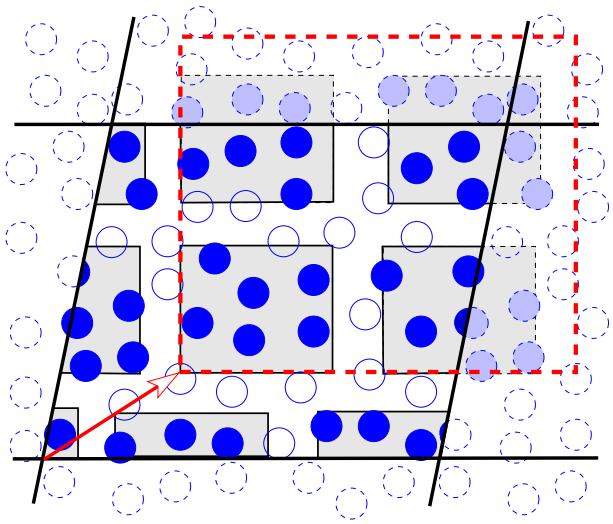

Figure 4.3: Parallelisation using a geometrical decomposition scheme. The grey areas are the active regions. Only beads in these active regions, the dark blue filled circles, will be moved during a Monte Carlo step. Reproduced from [97].

This is important to avoid interactions between beads in various active regions. Only the beads inside the active regions will be moved during a Monte Carlo step. Moves out of the active region will be rejected. To make sure that ergodicity is fulfilled, the offset of the active regions, represented by the red arrow in figure 4.3, is regularly moved by a random value.

In order to parallelise our system, we divide it into $N_x \times N_y \times 1$ subsystems, i.e. we need $N_x \times N_y$ processors. We do not divide the system in z-direction because of the possibility of one processor only getting solvent beads, which do not interact with each other. Processor 0 is the master processor: It is responsible for reading in configurations, writing configurations and doing the measurements. Dividing the system into subsystems, we deal with three different kinds of regions:

- *central region*: The system can be divided into $N_x \times N_y$ central regions. The system size of each central region is $(L_x/N_x, L_y/N_y, L_z)$. Each bead belongs exactly to one central region.

- *active region*: The active region is a subsystem of the central region. The offset of this region is 10% larger than half of the maximal interaction range of the beads. The maximal interaction range is the maximum of $\sigma \cdot r_c$ for the head, tail and solvent beads. The size of the active region is the size of the central region minus two times the offset of the active region.

- *boundary*: Each central region is covered by a boundary region of the same size

as the offset of the active regions.

The offset of the active region, represented by the red arrow, is regularly randomly chosen. It is within the range $[(0,0,0),(L_x/N_x,L_y/N_y,L_z)]$. Doing a new decomposition of the system, each processor decides to which new central region its beads belong and sends the according beads to the other processors. One has to bear in mind that the boundaries overlap with the active regions of the other processors. Therefore the volume and shear moves have to be done directly after a decomposition. Each processor calculates the energy of its central beads including the interaction with beads from other central regions which are in the boundary of the processor. Afterwards the master processor takes the sum of the contributions from the different processors. Before a configuration can be written or measurements of the system can be done, the new positions of the beads inside the active region have to be sent to the master processor. This is also done before a new decomposition of the system, because the master processor needs to know every position change of the beads.

An important component for parallel computing is to determine whether a programme is performing well. The values we are most interested in are the speedup and the efficiency of a parallel programme [80]:

- *speedup(*p*)*: (time of the serial programme) / (time of the parallel programme, using p processors)

- *efficiency(*p*)*: (time of the serial programme) / (number of processors p)*(time of the parallel programme, using p processors)

In table 4.1 we summarise some results of the parallelisation of a model system of 3200 lipids and 24612 solvent beads. We simulated 10000 Monte Carlo steps (every 10 steps decomposition, every 50 steps volume and shear moves, every 100 steps measurements, every 1000 steps writing the configuration) on the parallel computer *jump.fz-juelich.de* (IBM p690 cluster (Power4++ with 1.7GHz)). The number of beads in the active region is an approximated value. It depends on the number of beads in each central region and thus is different for every active region and every decomposition.

	no. of processors	user time [sec]	no. of beads in active regions
serial	1	11621	47012
$2 \times 2 \times 1$	4	4038	8000
$3 \times 3 \times 1$	9	2537	3500
$4 \times 4 \times 1$	16	2033	1600
$5 \times 5 \times 1$	25	1753	900
$6 \times 6 \times 1$	36	1668	500

Table 4.1: Parallelisation of the model system: User time and number of beads in the active region for different numbers of processors.

Figure 4.4 shows the speedup and the efficiency of the parallelisation of the model system calculated from the values of table 4.1. According to Amdahl's law

$$\text{speedup}(p) \leq \frac{1}{f + (1-f)/p} \quad , \tag{4.24}$$

where f is the fraction of time spent on unparallelisable work and p is the number of processors. The speedup is always less than or equal to $1/f$ no matter how many processors are used. Typically f is between $5 - 20\%$. In our case f is 12%. The reason for this high f is that the reading/writing and the measurements are still serial. In case we do the measurements and write out the configurations less often, we can speed up the programme. Another problem is that through the parallelisation extra work like communication has to be done by the processors. The more processors used, the more communication there is between the processors. This can also be seen in table 4.1. With an increasing number of processors the number of beads in the active region that are moved decrease. Therefore the programme spends a lot of time for the communication between the processors.

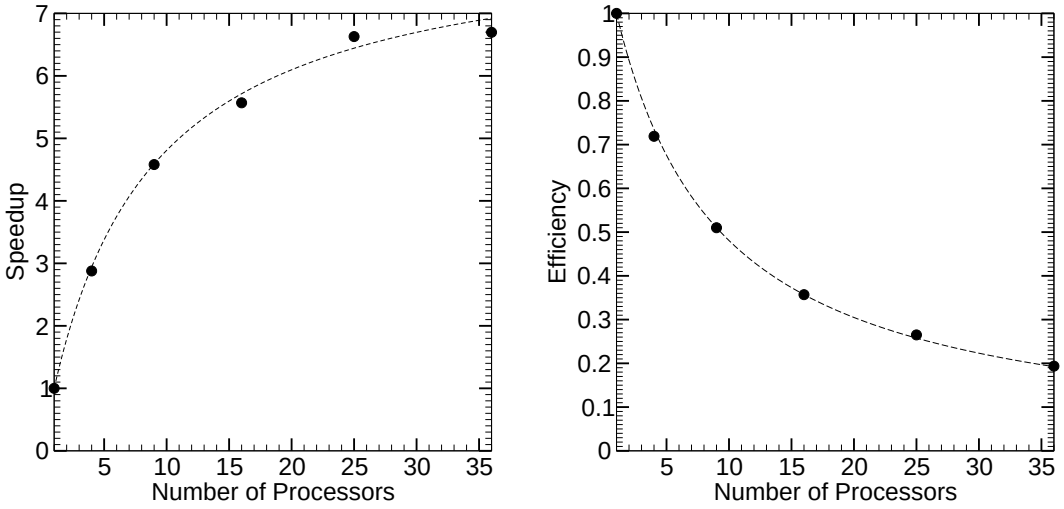

Figure 4.4: Speedup and efficiency as a function of the number of processors for the model system. The dashed line is calculated according to equation 4.24 with $f = 12\%$.

5 Characteristics of a Pure Lipid Bilayer

In this chapter we investigate some characteristics of a pure lipid bilayer in the fluid phase, $P = 2.0\epsilon/\sigma_t^3$, $k_BT = 1.3\epsilon$, and in the gel phase, $P = 2.0\epsilon/\sigma_t^3$, $k_BT = 1.0\epsilon$. These characteristics are inter alia the pressure profile and the fluctuation spectra. The system sizes range from 200 to 7200 lipids, and the simulations run up to 8 million Monte Carlo steps. The equilibration time was 4 million Monte Carlo steps for the analysis of the long-range fluctuations and 1 million Monte Carlo steps otherwise. For all simulations the moves altering the simulation box were attempted every 50th Monte Carlo step. In case the simulations were carried out on a parallel computer the domain decomposition was done every 10th Monte Carlo step.

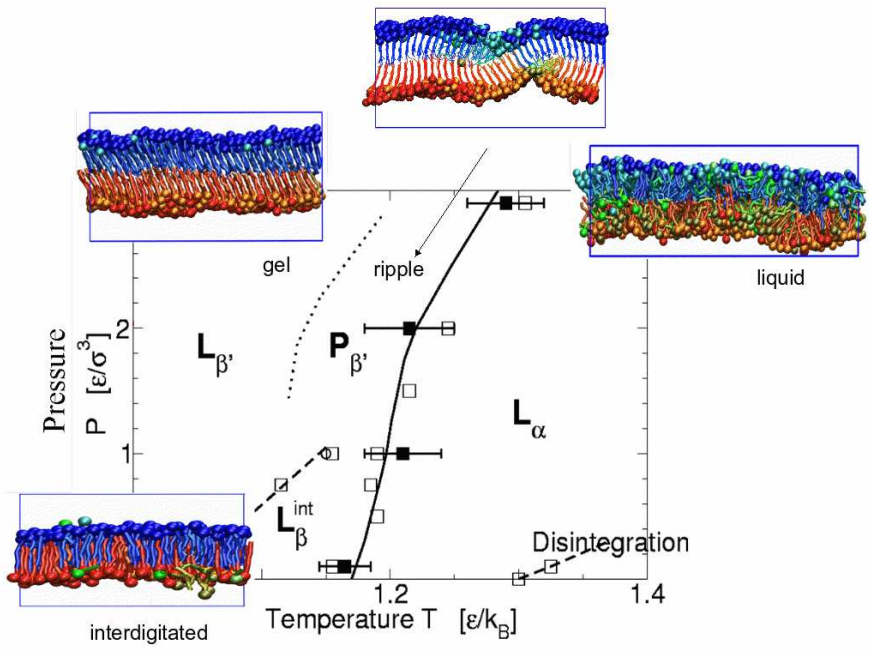

Figure 5.1: Phase diagram of our lipid model. Reproduced from [64, 66].

The bilayer model shows a very rich phase diagram (obtained from Olaf Lenz), figure 5.1. In the fluid phase L_α the lipids are disordered and more or less oriented parallel to the bilayer normal. They have a very high mobility in the plane of the membrane. In the gel phase $L_{\beta'}$ the lipids are very ordered and in a stretched configuration. The lipid chains are tilted towards the bilayer normal. In the interdigitated

gel phase L_β^{int} the lipid are again stretched but the two monolayers are interdigitated. The lipid chains show no tilt any more. Between the $L_{\beta'}$ phase and the L_α phase there is the ripple phase $P_{\beta'}$. In this phase the bilayer exhibits a height-varying ripple structure. Depending on the history of the system, it shows a symmetric or asymmetric ripple phase.

5.1 Pressure Profiles

Although the overall tension of real membranes in solution vanishes, the distribution of tension within the membrane is not uniform [39, 102]. It depends on the membrane composition and chemical structure of the lipids. The internal tension distribution can be calculated via the pressure tensor, chapter 4.2. The interfacial tension profile γ is given by

$$\gamma(z) = \mathcal{P}_N(z) - \mathcal{P}_T(z) \quad , \tag{5.1}$$

where $\mathcal{P}_N$ and $\mathcal{P}_T$ are the normal and tangential component of the pressure tensor, respectively:

$$\mathcal{P}_N(z) = \mathcal{P}_{zz}(z) \qquad \text{and} \qquad \mathcal{P}_T(z) = \frac{1}{2}(\mathcal{P}_{xx}(z) + \mathcal{P}_{yy}(z)) \quad . \tag{5.2}$$

The overall tension of the system is defined by the integral

$$\Gamma = \int_{-\infty}^{\infty} (\mathcal{P}_N(z) - \mathcal{P}_T(z))\mathrm{d}z \quad . \tag{5.3}$$

The first and second moment of the tension profile, equation 5.1, correspond to the spontaneous curvature c_0 and the Gaussian rigidity k_G [96]:

$$k_c c_0 = -\int_0^{\infty} \gamma(z)(z - z_0)\mathrm{d}z \tag{5.4}$$

$$k_G = 2\int_0^{\infty} \gamma(z)(z - z_0)^2\mathrm{d}z \quad . \tag{5.5}$$

k_c is the bending rigidity and $z = z_0$ is the "inextensibility plane", the plane in which an infinitesimal volume element is not compressed or extended if the monolayer is bent.

We measured the tension profile for the fluid and the gel phase for systems with 200, 288, 400 and 3200 lipids, figure 5.2. The system was centred around $z = 0$ and divided into slices of length $\delta z = 0.125\sigma_t$. Since the length of the simulation box varied, the size of the slices varied.

Qualitatively our tension profiles show the same characteristics as the tension profiles measured by Götz and Lipowsky [39] and others [68, 70, 90, 102]. The interfacial tension is much higher in the gel phase $\left(\text{between } -8\epsilon/\sigma_t^3 \text{ and } 4\epsilon/\sigma_t^3\right)$ than in the fluid phase $\left(\text{between } -0.7\epsilon/\sigma_t^3 \text{ and } 0.7\epsilon/\sigma_t^3\ (\epsilon/\sigma_t^3 \simeq 0.2 \text{ kbar})\right)$.

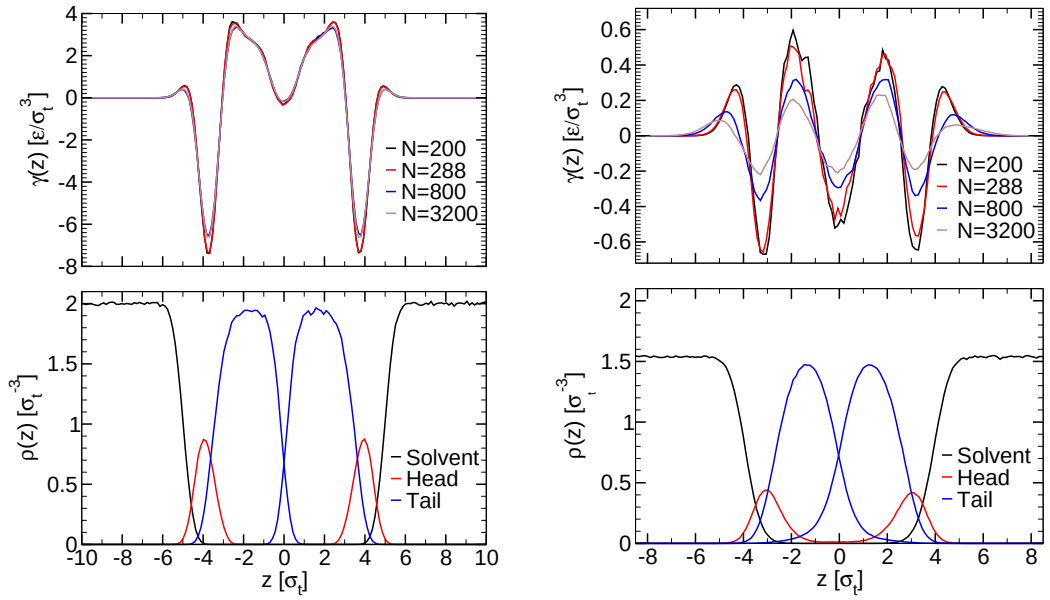

gel phase fluid phase

Figure 5.2: Tension profile $\gamma(z)$ for systems of different sizes (200, 244, 800, 3200 lipids) in the gel phase (left) and the fluid phase (right). The bottom panels show the corresponding density profiles $\rho(z)$ of solvent, head and tail beads in the system with 200 lipids.

Figure 5.3 (a) and (b) show the different contributions to the tension profile from the different potentials. A comparison of the distribution of the bond-angle potential according to Irving-Kirkwood and Götz-Lipowsky as described in section 4.2 can be found in panel (c). Looking at figure 5.3 (a) and (b) we can relate the different peaks to the different potentials: The first positive peak is related to a small positive surface tension between head and solvent beads. Since the interaction between head and solvent beads is purely repulsive, there is a reduction in density. This reduction in the solvent density leads to an increasing pressure. Since the head beads do not cover the surface of the lipid bilayer closely, there is a contact area between tail and solvent beads. The system tries to minimise this contact area resulting in a negative peak in the head region. The positive peak in the tail region reflects the fact that the tails attract each other. In the middle of the membrane, at $z = 0$, the density is again reduced and the negative peak indicates that the monolayers are strongly bound to each other. The positive contribution of the bond-angle potential indicates that the tails fluctuate and thus deviate from straight configurations. The positive contribution of the bond-length potential indicates that the lipids are stretched. The different contributions are much larger in the gel phase than in the fluid phase. The only exception is the contribution from the tail-solvent interaction indicating that the solvent is much more shielded from the tails in the gel phase.

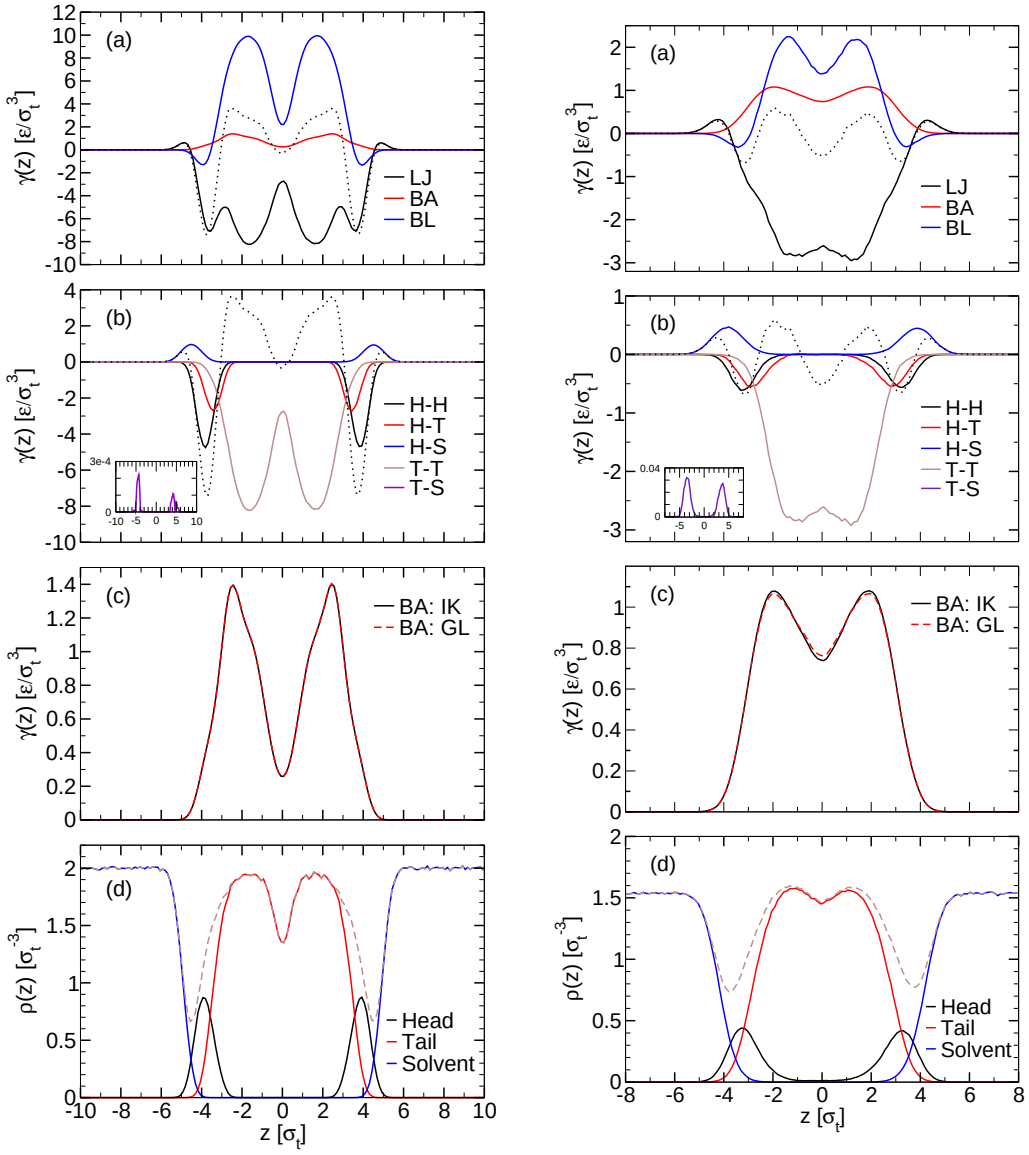

Figure 5.3: Different contributions to the tension profile $\gamma(z)$ for a system with 200 lipids in the gel phase (left) and the fluid phase (right). (a) Contributions from the Lennard-Jones (LJ), bond-angle (BA) and bond-length (BL) potential. (b) Contributions of the head (H), tail (T) and solvent (S) beads to the Lennard-Jones potential. (c) Comparison of the distribution of the bond-angle potential according to Irving-Kirkwood (IK) and Götz-Lipowsky (GL). (d) Density profiles $\rho(z)$ of the head, tail and solvent beads. The dotted black line in panel (a) and (b) is the total tension profile. The dashed brown line in panel (d) shows the total bead density.

	gel phase		fluid phase	
number of lipids	Γ_0 $[\epsilon/\sigma_t^2]$	Γ_2 $[\epsilon]$	Γ_0 $[\epsilon/\sigma_t^2]$	Γ_2 $[\epsilon]$
200	-0.03 ± 0.1	-121	-0.02 ± 0.1	2.8
288	0.004 ± 0.2	-119	-0.003 ± 0.1	2.7
800	0.03 ± 0.2	-119	-0.04 ± 0.1	2.0
3200	0.008 ± 0.03	-119	-0.02 ± 0.03	2.8

Table 5.1: Values for the first moment Γ_0 and the second moment Γ_2 of the tension profile for systems of different sizes in the gel and the fluid phase.

	gel phase		fluid phase	
Parameter	Value (LJ units)	Value (SI units)	Value (LJ units)	Value (SI units)
$k_c c_0$	$11.1 \pm 0.1\epsilon/\sigma_t$		$-0.3 \pm 0.1\epsilon/\sigma_t$	
c_0	$1.01 \pm 0.01\sigma_t^{-1}$	1.68nm^{-1}	$-0.05 \pm 0.02\sigma_t^{-1}$	-0.08nm^{-1}
k_G	$-60 \ldots 0\epsilon$	$-22 \ldots 0 \cdot 10^{-20}$J	-0.26 $[-2.8 \ldots 0]\epsilon$	$-1 \ldots 0 \cdot 10^{-20}$J

Table 5.2: Values for the spontaneous curvature and the Gaussian rigidity for the gel and the fluid phase measured in a system with 200 lipids. In the fluid phase we have chosen $z_0 = 2.6\sigma_t$. The values in SI units are calculated using $\sigma_t \sim 6$Å and $\epsilon \sim 0.36 \cdot 10^{-20}$J. c_0 is calculated using the value for k_c obtained from the fit of the fluctuation spectra, cf. section 5.2.

In the fluid phase the profiles are broadened in large systems due to large height fluctuations. Because the height fluctuations in the gel phase are very small we do not see this effect in the tension profiles. We assume that the tension profile $\gamma(z)$ bases on a size independent intrinsic tension profile $\gamma_{\text{int}}(z)$:

$$\gamma(z) = \int H\left(z - z'\right) \gamma_{\text{int}}\left(z'\right) \mathrm{d}z' \quad . \tag{5.6}$$

$H(z)$ is the distribution of interface heights and depends on the system size. The zeroth moment $\Gamma_0 = \int_{-\infty}^{\infty} \gamma(z)\mathrm{d}z$ and the second moment $\Gamma_2 = \int_{-\infty}^{\infty} \gamma(z)z^2\mathrm{d}z$ do not depend on the shape of the function $H(z)$ for symmetric tensionless bilayers with $\int \gamma(z)\mathrm{d}z = 0$. The first moment $\Gamma_1 = \int_{-\infty}^{\infty} \gamma(z)|z|\mathrm{d}z$, however, depends on the system size, cf. appendix A. Table 5.1 summarises the values for Γ_0 and Γ_2 for the gel and the fluid phase.

As we can see, Γ_0 is zero within the error in all systems, and Γ_2 does not depend on the system size. Since the lower integration bound in equation 5.5 is finite, the Gaussian rigidity, equation 5.5, nevertheless depends on the system size. The equations 5.4 and 5.5 are therefore only applicable in small systems. In order to calculate c_0 and k_G we use the data from the system with 200 lipids. The monolayer curvature $k_c c_0 = -0.3 \pm 0.1\epsilon/\sigma_t$ is slightly negative in the fluid phase. In the gel phase $k_c c_0 = 11.1 \pm 0.1\epsilon/\sigma_t$ is positive. When the system goes from low to high temperatures the tails disorder and occupy more membrane area, and c_0 decreases and changes sign as a result. The value for the Gaussian rigidity depends on the position of the plane

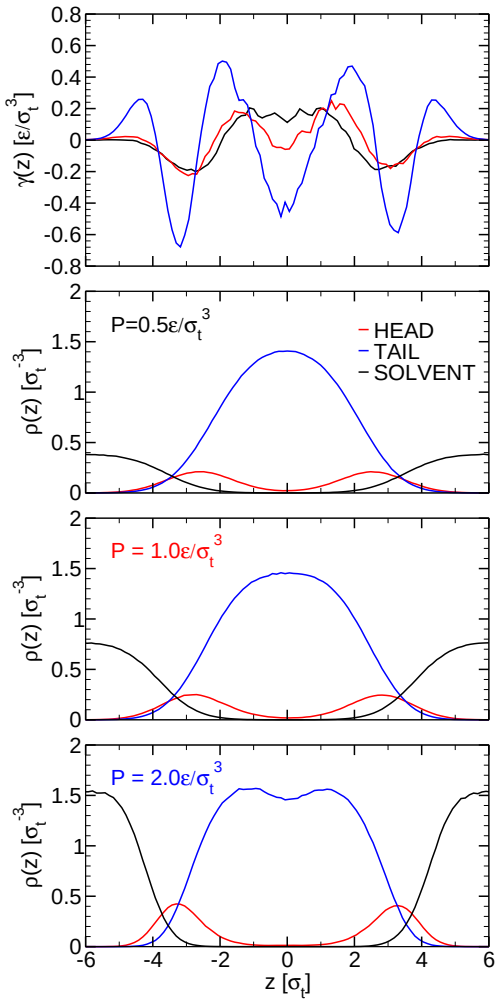

Figure 5.4: Tension profile $\gamma(z)$ of a system with 288 lipids in the fluid phase for different values of the pressure (top panel). The temperature is $k_BT = 1.3\epsilon$ and the pressure is $P = 0.5\epsilon/\sigma_t^3$ (black line), $P = 1.0\epsilon/\sigma_t^3$ (red line), and $P = 2.0\epsilon/\sigma_t^3$ (blue line), respectively. The other three panels show the corresponding density profiles $\rho(z)$ for the head (red line), tail (blue line) and solvent (black line) beads.

z_0. Positive values can be excluded, because a positive Gaussian rigidity would imply that the bilayer favours saddle-shape configurations. These configurations would destabilise flat bilayer structures on large scales and promote interconnected structures like cubic phases or sponge-like structures. Because our bilayers remain flat for all system sizes, only negative values of k_G are physically reasonable. We choose z_0 as the "neutral" plane where $\gamma(z)$ crosses zero.

Table 5.2 summarises the spontaneous curvature and the Gaussian rigidity. Our

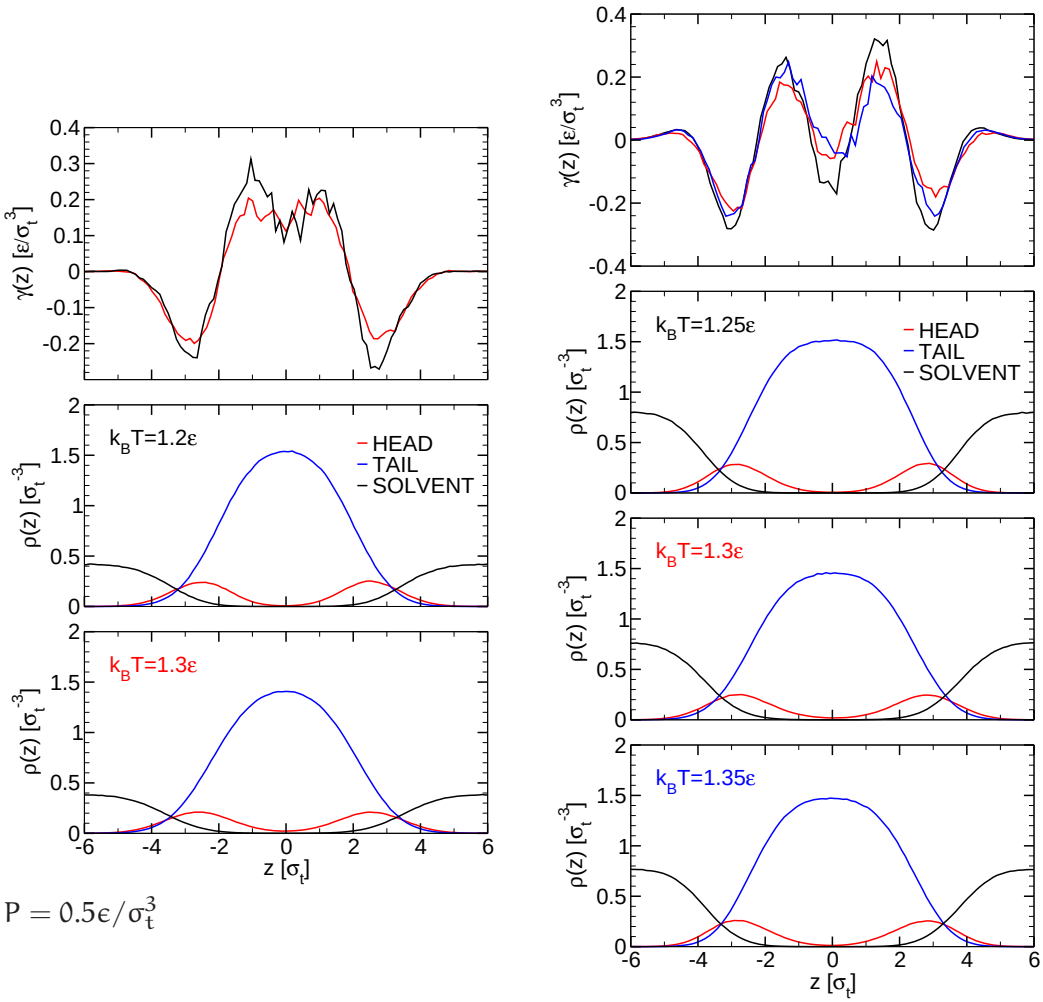

Figure 5.5: Tension profile $\gamma(z)$ of a system with 288 lipids in the fluid phase for different values of the pressure and the temperature (top panel). Left side: $P = 0.5\epsilon/\sigma_t^3$, $k_BT = 1.2\epsilon$ (black line), $k_BT = 1.3\epsilon$ (red line). Right side: $P = 1.0\epsilon/\sigma_t^3$, $k_BT = 1.25\epsilon$ (black line), $k_BT = 1.3\epsilon$ (red line), and $k_BT = 1.35\epsilon$ (blue line). The other three panels show the corresponding density profiles $\rho(z)$ for the head (red line), tail (blue line) and solvent (black line) beads.

value for c_0 in the fluid phase has the same order of magnitude as the values obtained from all-atoms simulations of DPPC $c_0 = -0.02 \ldots -0.05 \mathrm{nm}^{-1}$ [70] and experimental values $c_0 = -0.04 \mathrm{nm}^{-1}$, $k_G/k_c \sim -0.8$ [72].

As a last point we want to analyse the effect of the external pressure and the temperature on the tension profile, figures 5.4 and 5.5. For a system containing 288 lipids

in the fluid phase we varied on the one hand the pressure for a fixed temperature and on the other hand the temperature for a fixed pressure. The density of solvent beads obeys the ideal gas law $PV = Nk_BT$. It decreases with either decreasing pressure or increasing temperature. At a fixed temperature the tension profiles become flatter with decreasing pressure. Because of the decreasing pressure from outside the head and tail density profiles are less pronounced. For a pressure $P = 1.0\epsilon/\sigma_t^3$ the tension profiles exhibit the same characteristics as the profiles for a pressure $P = 2.0\epsilon/\sigma_t^3$, except for being more shallow. With increasing temperature the profiles become flatter. In the case of $P = 0.5\epsilon/\sigma_t^3$ the three middle peaks become one so that only three peaks are left. In the case of $k_BT = 1.2\epsilon$ there is a distinct overlap between the tail profiles of the upper and lower monolayer.

5.2 Fluctuation Spectra

Membranes are not perfectly flat but can exhibit significant thermal fluctuations, which lead to deformations in the bilayer height and thickness [96]. The analysis of the fluctuation spectrum is a widely used procedure to calculate the elastic constants of model membranes [9, 14, 20, 38, 67, 69]. We analyse the fluctuations within an elastic theory introduced with Brannigan and Brown [9].

The two monolayers can be described by four independent fluctuating fields: two for the mesoscopic bending deformations and two for the microscopic protrusions. It is assumed that the volume per lipid is constant and only the area per lipid Σ fluctuates. Furthermore it is assumed that the height and thickness fluctuations as well as the fluctuations in the protrusions are decoupled. The change in free energy due to the fluctuations can then be written as

$$\begin{aligned}\mathcal{F} = \int_{\mathcal{A}} dxdy \Bigg\{ & \frac{k_c}{2}\left(\nabla^2 z^+\right)^2 + k_\lambda \lambda^{+2} + \gamma_\lambda \left(\nabla\lambda^+\right)^2 + 2\gamma_\lambda \nabla z^+ \cdot \nabla\lambda^+ \\ & + \frac{k_A}{2t_0^2}(z^-)^2 + 2k_c c_0 \nabla^2 z^- + 2k_c \zeta \frac{z^-}{t_0}\nabla^2 z^- + \frac{k_c}{2}\left(\nabla^2 z^-\right)^2 \\ & + k_\lambda \lambda^{-2} + \gamma_\lambda \left(\nabla\lambda^-\right)^2 + 2\gamma_\lambda \nabla z^- \cdot \nabla\lambda^- \Bigg\} \quad .\end{aligned} \tag{5.7}$$

k_A is the compressibility modulus, $\zeta = c_0 - c_0'\Sigma_0$ is an extrapolated curvature with $c_0' = \partial c_0/\partial\Sigma|_{\Sigma=\Sigma_0}$, k_c is the bending rigidity, and c_0 is the spontaneous curvature. The parameters k_λ and γ_λ describe the protrusions. The quantities z^+ and z^- are the locally smoothed height of the bilayer midplane and the deviations in the monolayer thickness, whereas the quantities $\lambda^{+,-}$ are the average and half the difference of the protrusion fields. The height h of the bilayer midplane and the monolayer thickness t are defined as

$$h = z^+ + \lambda^+ \quad , \tag{5.8}$$

$$t = z^- + \lambda^- + t_0 \quad . \tag{5.9}$$

The spectra of the bilayer height and the monolayer thickness fluctuations, $\langle|h(q)|^2\rangle$ and $\langle|t(q)|^2\rangle$, are given by

$$\langle|h(q)|^2\rangle = \frac{k_B T}{k_c q^4} + \frac{k_B T}{2(k_\lambda + \gamma_\lambda q^2)} \quad , \tag{5.10}$$

$$\langle|t(q)|^2\rangle = \frac{k_B T}{k_c q^4 - 4k_c \zeta q^2/t_0 + k_A/t_0^2} + \frac{k_B T}{2(k_\lambda + \gamma_\lambda q^2)} \quad . \tag{5.11}$$

To determine the spectra for our membranes the system is divided into $N_x \times N_y$ bins in the xy-plane. In each bin the z-value of the mean head position is separately determined for both monolayers. The bilayer height $h(x, y)$ and monolayer thickness $t(x, y)$ with respect to t_0 is calculated according to equations 3.5 and 3.6. These two fields are Fourier transformed:

$$f(q_x, q_y) = \frac{L_x L_y}{N_x N_y} \sum_{\mathbf{q}} f(x, y) e^{-i(q_x x + q_y y)} \tag{5.12}$$

with $(q_x, q_y) = 2\pi(N_x/L_x, N_y/L_y)$. Because L_x and L_y fluctuate during the simulation q_x and q_y fluctuate, too; therefore the values of $|h(q)|^2$ and $|t(q)|^2$ are collected in q-bins of size 0.1. In each bin the averages $\langle|h(q)|^2\rangle$ and $\langle|t(q)|^2\rangle$ are evaluated.

The fluctuation spectrum for the fluid phase was obtained for a system containing 3200 lipids and 24615 solvent beads that was divided into $N_x = N_y = 20$ bins. To measure the fluctuation spectrum for the gel phase a system with 7200 lipids and 72000 solvent beads was used and divided into $N_x = N_y = 40$ bins. The curves of the different spectra are shown in figure 5.6 and the results of the fit are summarised in table 5.3.

The height fluctuations are Goldstone modes, hence the height spectrum diverges for small wavelength modes. The thickness spectrum is limited by the equilibrium bilayer thickness and tends towards a constant value for small wavelength values. At small q^2 the fluctuation spectra are dominated by the bending deformations. For larger values for q^2 the spectra are dominated by the protrusion modes. The protrusion modes are equal for the height and thickness fluctuations. These observations are consistent with observations from other simulations [67, 69]. We see that the theory fits the data of the fluid phase in an excellent way. The inset of figure 5.6 shows the fit of the thickness profile to the Landau-de Gennes theory, because the equation 2.3 can also be used to deduce an equation for the monolayer thickness fluctuation spectrum. To make the analysis comparable, we have included a protrusion contribution and fitted the monolayer thickness deformations to

$$\langle|t(q)|^2\rangle = \frac{k_B T}{4(a + cq^2)} + \frac{k_B T}{2(k_\lambda + \gamma_\lambda q^2)} \quad . \tag{5.13}$$

Not surprisingly, the Landau-de Gennes theory cannot reproduce the peak at non-zero q in $\langle|t(q)|^2\rangle$, hence it misses one important characteristic of the thickness spectrum. The fit of the data of the gel phase to the elastic theory is not satisfying.

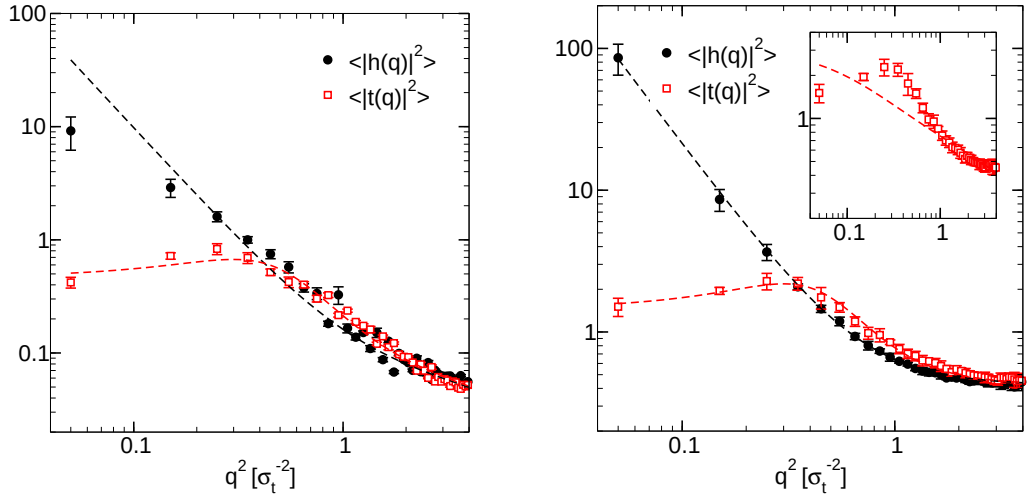

gel phase fluid phase

Figure 5.6: Fluctuation spectra of the height (black circles) and the thickness fluctuations (red squares) of the membrane in the gel phase (left) and the fluid phase (right). The dashed line shows the fit to the elastic theory, equations 5.10 and 5.11. The inset in the right figure shows the thickness data for the fluid phase alone with a fit to the Landau-de Gennes theory, equation 5.13.

	gel phase		fluid phase	
Parameter	Value (LJ units)	Value (SI units)	Value (LJ units)	Value (SI units)
k_c	$10.3 \pm 0.5\epsilon$	$3.7 \cdot 10^{-20}$J	$6.2 \pm 0.4\epsilon$	$2.2 \cdot 10^{-20}$J
ζ/t_0	$0.15 \pm 0.1\sigma_t^{-2}$	0.42nm^{-2}	$0.15 \pm 0.09\sigma_t^{-2}$	0.42nm^{-2}
k_A/t_0^2	$2.6 \pm 0.3\epsilon/\sigma_t^4$	$7.2 \cdot 10^{-20}$J/nm^4	$1.3 \pm 0.3\epsilon/\sigma_t^4$	$3.6 \cdot 10^{-20}$J/nm^4
k_λ	$6.5 \pm 0.2\epsilon/\sigma_t^4$	$18 \cdot 10^{-20}$J/nm^4	$1.5 \pm 0.1\epsilon/\sigma_t^4$	$4.2 \cdot 10^{-20}$J/nm^4
γ_λ	$1.23 \pm 0.1\epsilon/\sigma_t^2$	$3.4 \cdot 10^{-20}$J/nm^2	$0.007 \pm 0.01\epsilon/\sigma_t^2$	$0.7 \cdot 10^{-22}$J/nm^2
$\gamma_\lambda^2/k_\lambda k_c$	0.02		$5 \cdot 10^{-6}$	

Table 5.3: Elastic constants of the membrane in the gel and the fluid phase obtained from the fit of the height and thickness spectrum. The SI values are calculated using $\sigma_t \sim 6$Å and $\epsilon \sim 0.36 \cdot 10^{-20}$J.

The elastic theory assumes that the fluctuations in the height, thickness and protrusions are decoupled. The strength of the coupling between bending modes and protrusion modes can be estimated by the coupling parameter $\gamma_\lambda^2/k_\lambda k_c$. For the fluid phase this parameter is indeed much smaller than unity. For the gel phase the value is much larger but still negligible.

The elastic constants obtained for our model in the fluid phase have the same order of magnitude than those obtained based on all-atom simulations of DPPC [67], other

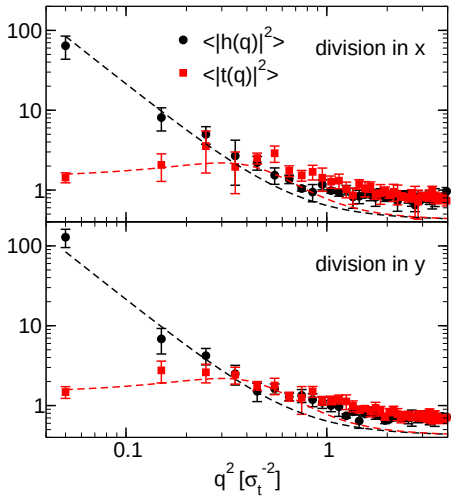

Figure 5.7: Fluctuation spectra of the height (black circles) and the thickness fluctuations (red squares) of the membrane in the fluid phase, if the system is divided along one direction: $N_x = 40, N_y = 1$ bins (upper figure), $N_x = 1, N_y = 40$ bins (lower figure). The dashed lines are the fits to the elastic theory, taken from figure 5.6.

coarse-grained models [9], $k_c \sim 4 \cdot 10^{-20}$J, $k_A/t_0^2 \sim 1.1 \cdot 10^{-20}$J/nm^4, $\zeta/t_0 \sim 0.18$nm^{-2}, and those based on experimental estimates $k_c \sim 5 - 20 \cdot 10^{-20}$J, $k_A/t_0^2 \sim 6 \cdot 10^{-20}$J/nm^4 [72].

Figures 5.7 and 5.8 show the fluctuation spectra if the system is only divided along one direction. In the fluid phase the system is divided into $N_x = 40, N_y = 1$ and $N_x = 1, N_y = 40$ bins. There is no significant difference for the spectra in x- and y-direction: The system is isotropic. If we compare these data to the curves we got by fitting the data obtained for a system divided in both directions simultaneously to the elastic theory, taken from figure 5.6, we see that these theoretical curves agree very reasonably with the data for small q^2 values. There are differences for large values of q^2 where the system is dominated by the protrusion modes. The protrusions are averaged away due to the averaging process along the direction of the system.

In the gel phase the system is divided into $N_x = 60, N_y = 1$ and $N_x = 1, N_y = 60$ bins. The lipids are tilted and can be characterised by two angles: θ describes the tilt angle towards the z-axis and ϕ is the angle in the xy-plane. Therefore the whole system is rotated by the angle $-\phi$ before we measure the fluctuation spectra. If we divide the system in the x- and y-direction simultaneously, the rotation of the system has no influence on the fluctuation spectra, as we can see in the left side of figure 5.8. If the system is divided along the tilt direction the height fluctuations are suppressed on large scales. The thickness fluctuations are suppressed on small scales. If the system is divided perpendicular to the tilt direction the thickness fluctuations are suppressed on all length scales. In this case the protrusion modes on the large length scale are

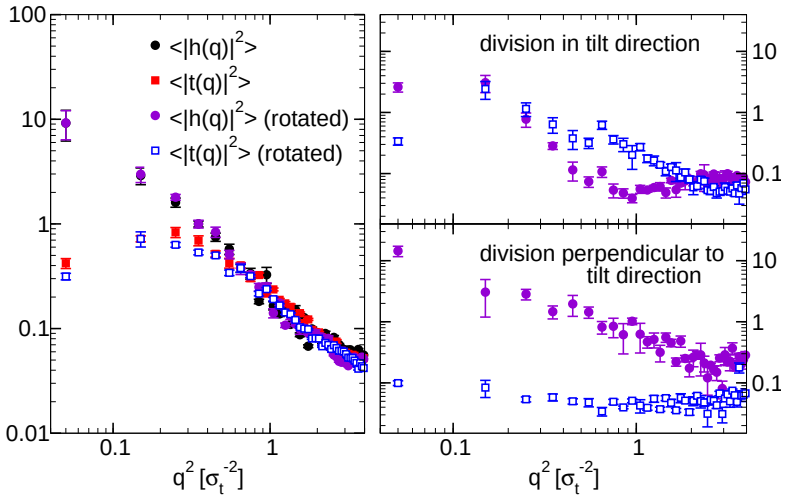

Figure 5.8: Fluctuation spectra of the membrane in the gel phase. The left figure shows the fluctuation spectra if the system is divided into $N_x = 40, N_y = 40$ bins. The black circles and the red squares show the height and thickness fluctuation spectra of the original system, respectively. The violet circles and the blue squares show the height and thickness fluctuation spectrum, respectively, if the system is rotated according to the angle $-\phi$ in the xy-plane. The right upper and lower figure show the fluctuation spectra if the system is divided into $N_x = 60, N_y = 1$ and $N_x = 1, N_y = 60$ bins, respectively. The system is rotated before the fluctuation spectra are measured.

not equal for the height and thickness spectrum.

5.3 Conclusions

The calculation of the pressure tensor shows that the lipid bilayer is in a tension-free state. Additionally we could extract the spontaneous curvature and the Gaussian rigidity from the tension profile. With the elastic theory we could fit the height and thickness fluctuation spectra in an excellent way. Furthermore, we could extract elastic constants we need for the analysis of the deformation profiles of a single protein (cf. chapter 6) and the analysis of the effective interaction between two proteins (cf. chapter 7).

6 Lipid Bilayer with One Protein in the Fluid Phase

In this chapter we investigate a lipid bilayer with one protein in the fluid phase, $P = 2.0\epsilon/\sigma_t^3$, $k_BT = 1.3\epsilon$. The analysis is done for different system sizes. Furthermore we compare on the one hand the deformation profiles for proteins of different diameters and on the other hand the deformation profile of a protein oriented along the z-axis to the deformation profile of a sphero-cylinder protein, which is allowed to tilt. The last point in this chapter is the calculation of the change in free energy if the protein is removed from the lipid bilayer. The simulations run between 3 and 5 million Monte Carlo steps with equilibration times up to 1 million Monte Carlo steps. Moves altering the simulation box were attempted every 50th Monte Carlo step. In the simulations carried out on a parallel computer, the domain decomposition was reshuffled every 10th Monte Carlo step.

6.1 Bilayer Deformation

In order to investigate the deformation of a bilayer by a single protein we measure the bilayer thickness as a function of the distance from the protein in a system containing 3176 lipids. The values for the hydrophobic length L are chosen such that we have one case of negative $(L = 4\sigma_t)$, no $(L = 6\sigma_t)$, and positive $(L = 8\sigma_t)$ hydrophobic mismatch. The hydrophobicity parameter ϵ_{pt} is varied between 1.0 and 6.0, whereas a hydrophobicity of $\epsilon_{pt} = 1.0$ is sufficient to trap the centre of the protein inside the lipid bilayer, figure 6.1.

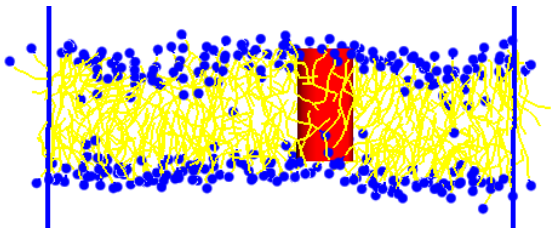

Figure 6.1: Cross-section snapshot of a model membrane with one protein. The hydrophobic length $L = 6\sigma_t$ roughly matches that of the lipid bilayer. The hydrophobicity parameter is $\epsilon_{pt} = 1.0$. The blue circles are the heads and the yellow lines show the tail bonds. The hydrophobic part of the protein is represented by the red cylinder. The solvent beads are omitted for clarity.

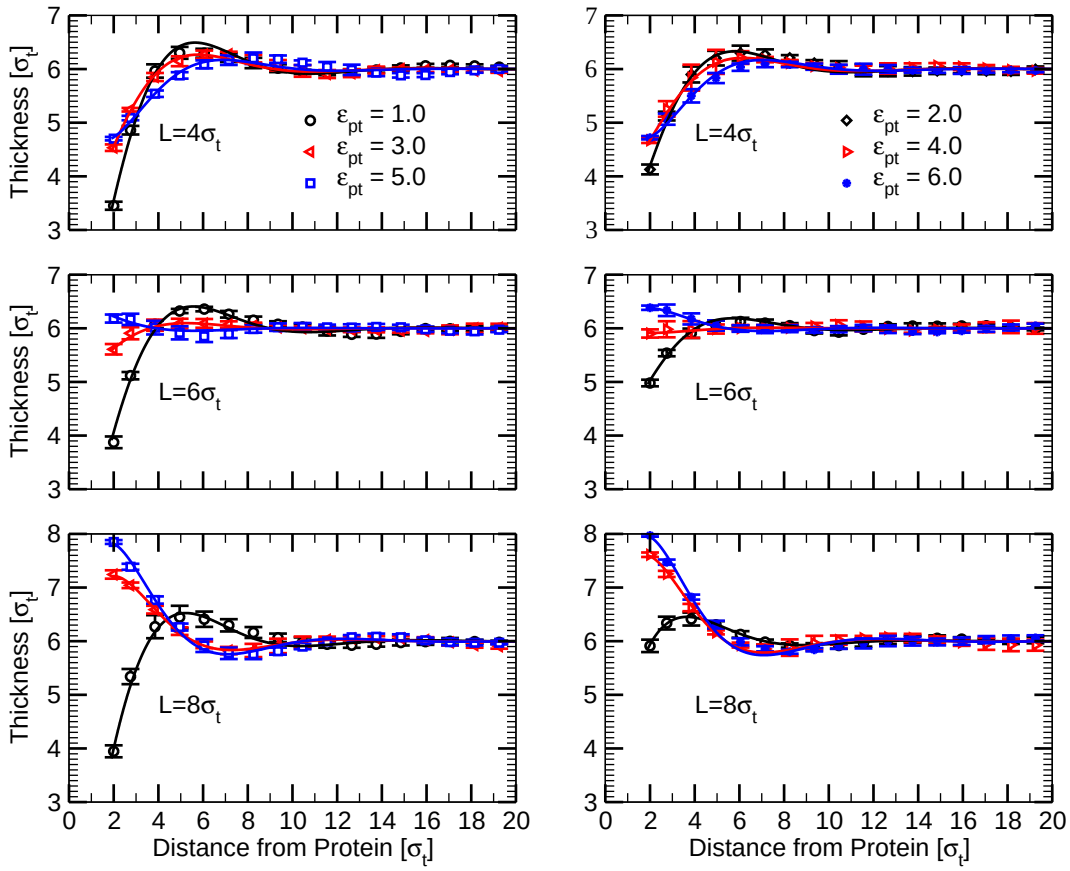

Figure 6.2: Radial membrane thickness profiles in the vicinity of a protein with a hydrophobic length $L = 4\sigma_t$ (top panels), $L = 6\sigma_t$ (middle panels) and $L = 8\sigma_t$ (bottom panels) and hydrophobicity parameters ϵ_{pt} as indicated. The solid lines show the fit to the elastic theory, equation 2.15 with the boundary condition 2.29.

Figure 6.2 shows the thickness profiles for different values of L and ϵ_{pt}. The thickness is measured according to equation 3.5 as a function of the distance from the protein. Although the radius of the protein is $R = 1.5\sigma_t$, the curves start at $R = 2.0\sigma_t$, because up to this distance the head beads are repelled due to the Lennard-Jones potential.

We observe that the hydrophobicity parameter must exceed a certain value in order to produce classical hydrophobic matching. When the hydrophobicity is too small the protein repels the lipids independent of the value of L. The bilayer surfaces get pinned by the protein for values of the hydrophobicity parameter larger than $\epsilon_{pt} = 4.0$. This is the critical value where touching the protein surface is about as favourable for tail beads, from an energetic point of view, than being immersed in the bulk. The maximal contact energy of a tail bead in contact with a plane of tail beads is 4ϵ.

The thickness profiles are not strictly monotonic but rather show a characteristic over- or undershooting at the distance $r \sim 6\sigma_t$. This weakly oscillating behaviour was also observed in previous coarse-grained [10, 115] and atomistic [15] simulations of protein-induced membrane deformations.

The solid lines in figure 6.2 are the fit to the elastic theory, equation 2.15 with the boundary condition 2.29. When fitting the data we set

$$y := \nabla_r^2 \phi \Big|_R = -2\left(\tilde{c}_0 - \frac{\zeta}{t_0} t_R\right) - \frac{k_G}{k_c R} t'_R \tag{6.1}$$

for the boundary condition and use y as a fit parameter. This has the advantage that we can measure the renormalised curvature $\tilde{c}_0$ as a function of the Gaussian rigidity k_G. The second fit parameter is t_R. Furthermore we set $t_0 = 3.0\sigma_t$ for the asymptotic monolayer thickness and $R_{el} = 1.5\sigma_t$ and $2.0\sigma_t$, respectively. The radius $R_{el} = 1.5\sigma_t$ corresponds to the real protein radius and the radius $R_{el} = 2.0\sigma_t$ corresponds to the point where the data starts. The results for the fit parameters are summarised in table 6.1.

The theory describes the thickness profiles very well. The fit curves show no difference for the two values of R_{el}, because a difference due to R_{el} is adjusted by the fit parameter y and with this by the renormalised curvature $\tilde{c}_0$ as we see in table 6.1. For $R_{el} = 2.0\sigma_t$ the renormalised curvature obtained for the data for $L = 4\sigma_t$ and a hydrophobicity parameter $\epsilon_{pt} = 5.0$, 6.0 corresponds to the spontaneous curvature we obtained from the tension profile. Otherwise none of the values for the renormalised curvature agree to the value of our measured spontaneous curvature. The effective hydrophobic length of the protein is defined as $L_{eff} = 2(t_0 + t_R)$. The exact relation between t_R and L is not quite clear, because the lipid-protein interaction is smooth and varies on the length scale σ_t. For values $\epsilon_{pt} > 4.0$ the values obtained for L_{eff} are reasonable close to L, well within $1\sigma_t$.

In order to compare the elastic theory to the Landau-de Gennes theory we use the data for $\epsilon_{pt} = 6.0$, figure 6.3. In the case of the Landau-de Gennes theory, equation 2.7, we fit the three profiles simultaneously using ζ as one common fit parameter and three separate fit parameters t_R, table 6.2. The exponential fit cannot reproduce the oscillatory behaviour of the profiles, but otherwise the fit is quite reasonable. The values obtained for the effective hydrophobic length L_{eff} are in this case larger than the values obtained for the elastic theory, but they are still quite close to L, well within $1\sigma_t$. For the pure version of the elastic theory, equation 2.15 with the boundary condition 2.12, we have varied c_0 and k_G within the error with t_R as sole fit parameter. None of the fits are satisfactory. The pure version of the elastic theory describes the profiles in terms of bulk membrane properties. As we saw earlier the data can be fitted very nicely by replacing the spontaneous curvature c_0 by a renormalised curvature $\tilde{c}_0$. As we can see from table 6.1, $\tilde{c}_0$ depends on L showing that the local structure of the lipids surrounding the protein contributes to the boundary condition. Brannigan and Brown [10] also observed such an effect and explained it by the effect of a non-constant lipid volume. In their model the volume per lipid varied fundamentally

$L\ [\sigma_t]$	ϵ_{pt}	$R_{el}\ [\sigma_t]$	$t_R\ [\sigma_t]$	$L_{eff}\ [\sigma_t]$	$\tilde{c}_0\ [\sigma_t^{-1}]$	
4	1.0	1.5	−1.7	2.6	0.02	[0.16 . . . − 0.15]
4	2.0	1.5	−1.21	3.58	−0.01	[0.07 . . . − 0.11]
4	3.0	1.5	−0.97	4.06	−0.01	[0.06 . . . − 0.09]
4	4.0	1.5	−0.82	4.36	−0.04	[−0.01 . . . − 0.09]
4	5.0	1.5	−0.67	4.66	−0.11	[−0.11 . . . − 0.10]
4	6.0	1.5	−0.66	4.68	−0.11	[−0.12 . . . − 0.11]
6	1.0	1.5	−1.36	3.28	0.03	[0.14 . . . − 0.11]
6	2.0	1.5	−0.66	4.68	0.01	[0.05 . . . − 0.06]
6	3.0	1.5	−0.28	5.44	0.01	[0.04 . . . − 0.02]
6	4.0	1.5	−0.04	5.92	−0.01	
6	5.0	1.5	0.16	6.32	−0.01	[−0.03 . . . 0.01]
6	6.0	1.5	0.18	6.36	0.05	[0.06 . . . 0.03]
8	1.0	1.5	−1.51	2.98	0.08	[0.24 . . . − 0.10]
8	2.0	1.5	−0.27	5.46	0.13	[0.21 . . . 0.03]
8	3.0	1.5	0.56	7.12	0.15	[0.18 . . . 0.11]
8	4.0	1.5	0.78	7.56	0.16	[0.18 . . . 0.14]
8	5.0	1.5	0.92	7.84	0.19	[0.21 . . . 0.15]
8	6.0	1.5	0.93	7.86	0.22	[0.26 . . . 0.17]
4	1.0	2.0	−1.22	3.56	0.08	[0.18 . . . − 0.03]
4	2.0	2.0	−0.9	4.2	0.04	[0.1 . . . − 0.03]
4	3.0	2.0	−0.72	4.56	0.04	[0.09 . . . − 0.02]
4	4.0	2.0	−0.66	4.68	0.005	[0.04 . . . − 0.04]
4	5.0	2.0	−0.64	4.72	−0.05	[−0.04 . . . − 0.07]
4	6.0	2.0	−0.63	4.74	−0.06	[−0.05 . . . − 0.07]
6	1.0	2.0	−0.97	4.06	0.07	[0.15 . . . − 0.02]
6	2.0	2.0	−0.49	5.02	0.03	[0.06 . . . − 0.01]
6	3.0	2.0	−0.19	5.62	0.02	[0.04 . . . − 0.001]
6	4.0	2.0	−0.04	5.92	−0.01	
6	5.0	2.0	0.11	6.22	−0.01	[−0.02 . . . 0.002]
6	6.0	2.0	0.19	6.38	0.022	[−0.02 . . . 0.024]
8	1.0	2.0	−1.0	4.0	0.12	[0.22 . . . 0.01]
8	2.0	2.0	−0.03	5.94	0.1	[0.14 . . . 0.06]
8	3.0	2.0	0.61	7.22	0.08	
8	4.0	2.0	0.79	7.58	0.08	[0.07 . . . 0.09]
8	5.0	2.0	0.93	7.86	0.1	[0.07 . . . 0.11]
8	6.0	2.0	0.97	7.94	0.1	[0.09 . . . 0.12]

Table 6.1: Fit of the radial thickness profiles to the elastic theory: t_R (monolayer deformation at the surface of the protein), L_{eff} (effective hydrophobic length of the protein), $\tilde{c}_0$ (renormalised curvature). The radius is set to $R_{el} = 1.5\sigma_t$ and $2.0\sigma_t$, respectively. The asymptotic value for the monolayer thickness is $t_0 = 3.0\sigma_t$. The value of the renormalised curvature belongs to a Gaussian rigidity $k_G = -0.26\epsilon$. The values in case the Gaussian rigidity is changed within its error are in brackets.

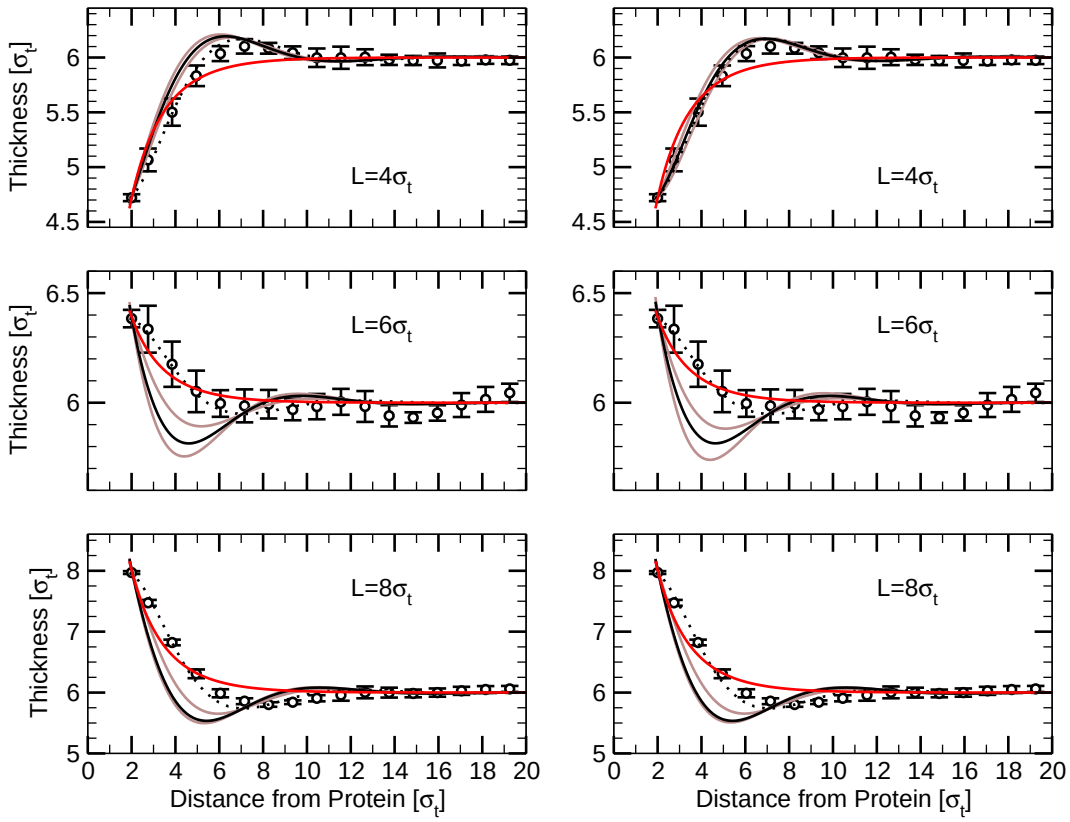

Figure 6.3: Radial membrane thickness profiles in the vicinity of a protein of hydrophobic length $L = 4\sigma_t$ (top panels), $L = 6\sigma_t$ (middle panels) and $L = 8\sigma_t$ (bottom panels) and a hydrophobicity parameter $\epsilon_{pt} = 6.0$ compared to the fit to the Landau-de Gennes theory (red line) and to the elastic theory with fixed spontaneous curvature $c_0 = -0.05\sigma_t^{-1}$ and Gaussian rigidity $k_G = -0.26\epsilon$ (black line) and to the elastic theory where c_0 is replaced by $\tilde{c}_0$ (dotted line). The brown lines indicate the range of the fit at fixed c_0 and k_G, if both quantities are varied within the error. The left hand side corresponds to a protein radius $R_{el,LdG} = 1.5\sigma_t$ and the right hand side corresponds to a protein radius $R_{el,LdG} = 2.0\sigma_t$.

with the distance from the protein. In our model the lipid volume is almost constant throughout the system.

The question arising is what kind of quantity might effect the membrane properties and renormalise the curvature term at the surface. Figure 6.4 shows some candidates. In the top panels there are the thickness as well as the volume per bead, respectively. The volume per bead is, as already mentioned, almost constant at all distances from the protein. It is decreased close to the protein due to the attractive tail-protein interaction. Then a small depletion zone follows, where the volume per bead is increased.

	$R_{LdG} = 1.5\sigma_t$		$R_{LdG} = 2.0\sigma_t$	
$L\ [\sigma_t]$	$t_R\ [\sigma_t]$	$L_{eff}\ [\sigma_t]$	$t_R\ [\sigma_t]$	$L_{eff}\ [\sigma_t]$
4	-0.94	4.12	-0.64	4.72
6	0.3	6.6	0.2	6.4
8	1.44	8.88	1	8

Table 6.2: Fit of the radial thickness profiles for the $\epsilon_{pt} = 6.0$ data to the Landau-de Gennes theory: t_R (monolayer deformation at the surface of the protein), L_{eff} (effective hydrophobic length of the protein). The radius R_{LdG} in equation 2.7 is set to $1.5\sigma_t$ and $2.0\sigma_t$, respectively. The asymptotic monolayer thickness is $t_0 = 3.0\sigma_t$. The decay length is $\zeta = 2.0 \pm 0.1\sigma_t$.

It is remarkable that the curves are almost identical for the three different hydrophobic protein lengths.

The next panels show the area density of all beads, and that of the head beads. The number of beads per area is enhanced close-by the protein for the case of positive and zero hydrophobic mismatch. In the case of negative hydrophobic mismatch it is reduced. This is a consequence of the fact that tail-protein attraction is related to the hydrophobic length of the protein. The larger the hydrophobic length of the protein, the larger the area over which lipid tails get attracted by the protein. A larger area attracts more lipid tails than a smaller one.

The number of heads per area and the hydrophilic shielding parameter are related to the shielding of the hydrophobic membrane interior from the solvent. The shielding is achieved by the head beads and the head density is therefore a measure of the effectiveness of shielding. Since the lipid volume is constant in our model, the head density is directly related to the monolayer thickness and thus cannot directly contribute to the renormalised curvature. The head density is enhanced close to the protein. This is an indirect consequence of the attractive protein-tail interaction. At intermediate distances the head density goes up in the case of positive mismatch and goes down in the case of negative mismatch.

The hydrophobic shielding parameter, shown in the next panel, was introduced by de Meyer et al. [19]. It is defined as the ratio of head density and tail density. The hydrophobic shielding parameter shows the same behaviour as the head density for intermediate distances. Over-shielding for positive mismatch and under-shielding for negative mismatch. Close to the protein the curves turn around. This is in agreement with the observations of de Meyer et al. [19].

The right panel in the third row shows the local chain order parameter S_z. It is calculated according to equation 3.8 using the bond vectors between two neighbouring beads. The order is increased close-by the protein. Not surprisingly the lipids are stretched the most in the case of positive mismatch. In contrast the lipids are more ordered in the case of negative mismatch than in the hydrophobically matching case. At larger distances the profile decays monotonically for the case of positive mismatch and matching. It exhibits a non-monotonic dip in the case of negative mismatch. In

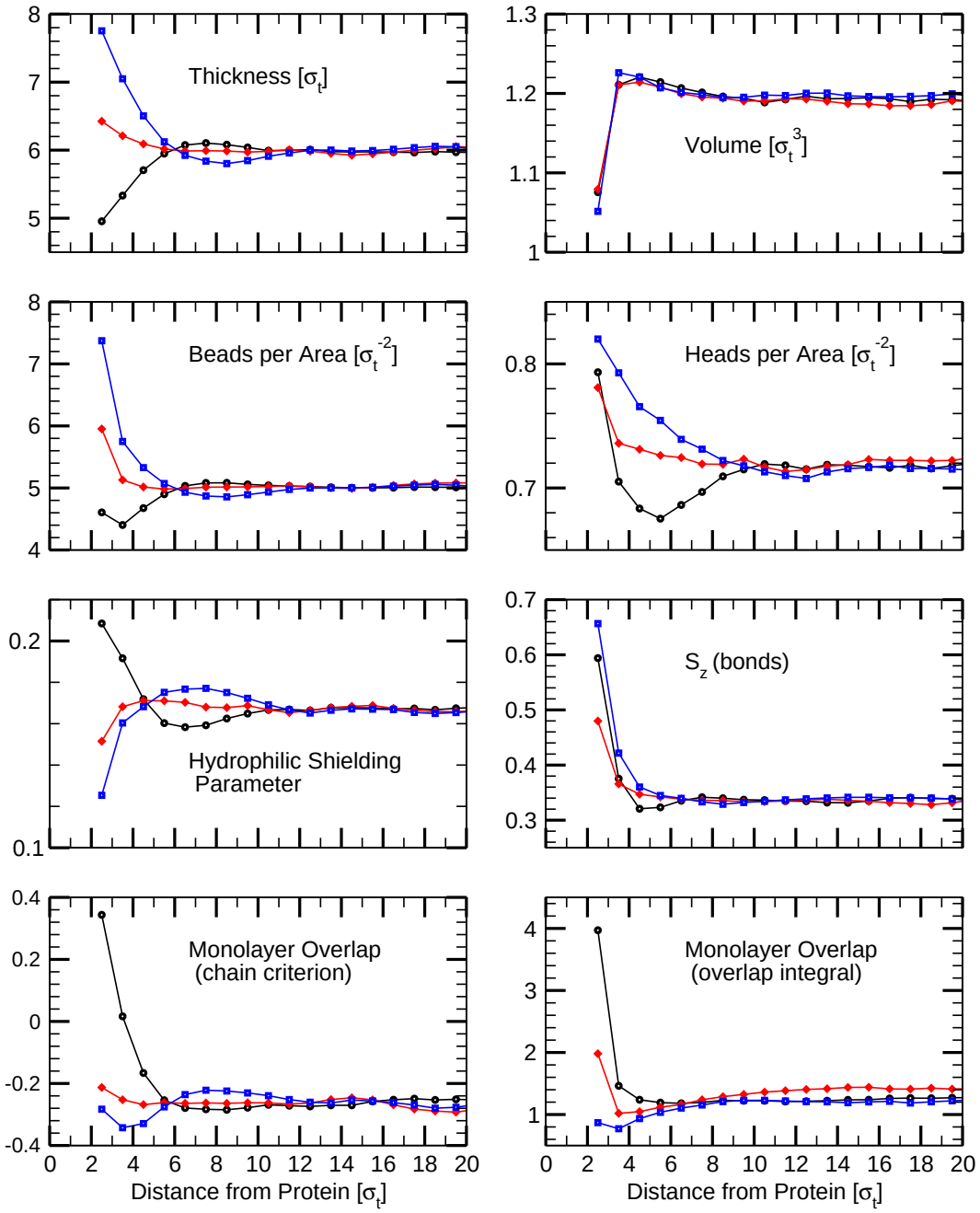

Figure 6.4: Radial profiles of various quantities as a function of the distance from the centre of a protein of hydrophobic length $L = 4\sigma_t$ (black circles), $L = 6\sigma_t$ (red diamonds) and $L = 8\sigma_t$ (blue squares) and a hydrophobicity parameter $\epsilon_{pt} = 6.0$

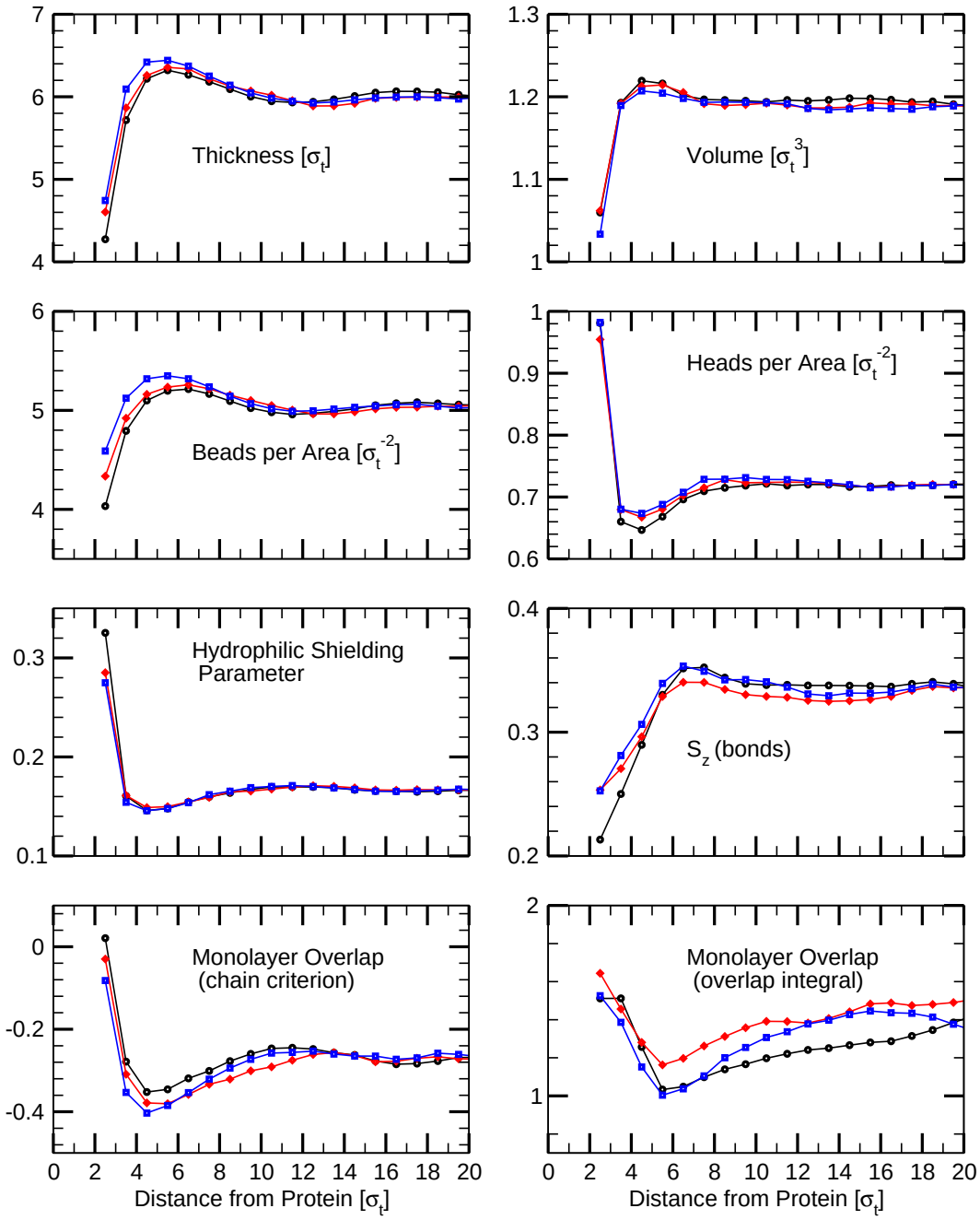

Figure 6.5: Radial profiles of various quantities as a function of the distance from the centre of a protein of hydrophobic length $L = 4\sigma_t$ (black circles), $L = 6\sigma_t$ (red diamonds) and $L = 8\sigma_t$ (blue squares) and a hydrophobicity parameter $\epsilon_{pt} = 1.0$

the negative mismatch case the two monolayers overlap much more than in the hydrophobic matching case, figure 6.4, bottom panels. Therefore the fact that the lipids are much more ordered in the negative matching case is not surprising any more.

The bottom panels show the monolayer overlap calculated according to equation 3.9 and 3.10. The chain criterion overlap parameter is negative far away from the protein indicating that the two monolayers are very well separated. Close to the protein the overlap parameter turns positive in the negative mismatch case. The protein pulls the lipids inwards and thus enforces an overlap. For the case of positive mismatch and matching protein the overlap parameters remain negative and more or less constant. The curves calculated using the overlap integral are shifted to positive values, but besides this show the same characteristics. Even far away from the protein the monolayers have some overlap in the centre of the bilayer.

From these curves it is not clear which quantity contributes to the renormalised curvature. Either we have not found it or most of these quantities affect the renormalised curvature in a concerted way.

Figure 6.5 shows the same quantities for a hydrophobicity parameter $\epsilon_{\mathrm{pt}} = 1.0$. From the thickness profiles we know that the protein repels the lipids independent of the hydrophobic length L. First of all we notice that the different quantities show the same behaviour mostly independent of the hydrophobic length L. If we compare these profiles to the profiles for $\epsilon_{\mathrm{pt}} = 6.0$ we can say something about the influence of ϵ_{pt} on these quantities. As we already know, the bilayer thickness close to the protein increases with an increasing hydrophobicity parameter. The volume at direct contact to the protein decreases a little with increasing hydrophobicity parameter. The beads per area and the tails per area increase, while the heads per area decrease with increasing ϵ_{pt}. This effect is due to the increasing attraction between the tail beads and the protein. Since more tail beads come into contact with the protein the head beads are repelled. The behaviour of the heads per area is reflected in the hydrophilic shielding parameter. The (bond) chain order parameter increases with increasing hydrophobicity parameter indicating that the lipids get stretched. The behaviour described so far is valid independent of the hydrophobic length L. The only parameter that shows a different behaviour dependent on L is the overlap parameter. In the case of negative hydrophobic mismatch, $\mathrm{L} = 4\sigma_{\mathrm{t}}$, the overlap parameter increases with increasing ϵ_{pt}. Whereas in the case of positive hydrophobic mismatch, $\mathrm{L} = 8\sigma_{\mathrm{t}}$, and hydrophobic matching, $\mathrm{L} = 6\sigma_{\mathrm{t}}$, the overlap parameter decreases. For $\epsilon_{\mathrm{pt}} = 1.0$ the overlap parameter is about zero around the protein. In the case of negative hydrophobic mismatch the two monolayers show an overlap, whereas the two monolayers do not overlap in the other two cases. With increasing distance to the protein the chains get stretched and the two monolayers overlap.

6.2 Influence of the System Size on the Thickness Profile

When we fitted the thickness profiles we set a value for the asymptotic monolayer thickness t_0 which was actually slightly smaller than the monolayer thickness of an

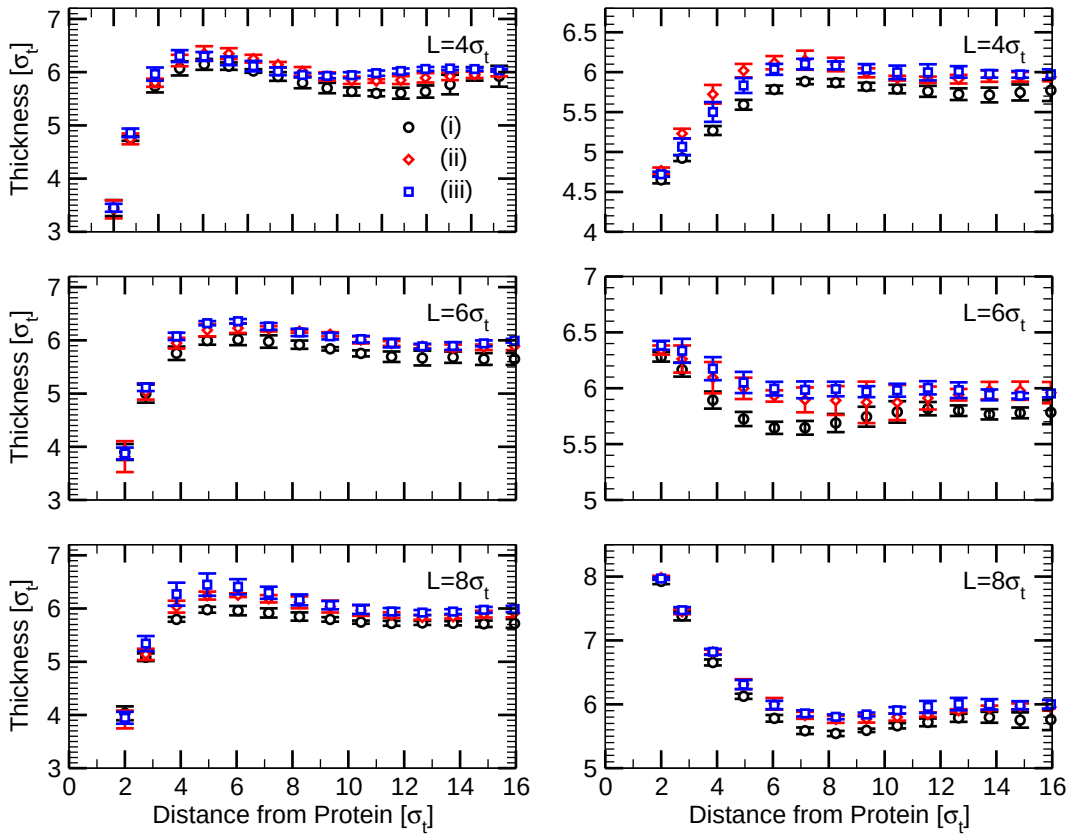

Figure 6.6: Radial membrane thickness profiles of a lipid bilayer of various sizes: (i) 776 lipids and 6153 solvent beads (black circles), (ii) 1776 lipids and 13846 solvent beads (red diamonds), and (iii) 3176 lipids and 24615 lipids (blue squares). The hydrophobic length of the protein is $L = 4\sigma_t$ (upper panels), $L = 6\sigma_t$ (middle panels), and $L = 8\sigma_t$ (bottom panels). The hydrophobicity parameter is $\epsilon_{pt} = 1.0$ (left) and $\epsilon_{pt} = 6.0$ (right).

undisturbed lipid bilayer ($t_0 = 3.05\sigma_t$, section 3.1.1). Theoretically the thickness far away from the protein should be equal to the thickness of an undisturbed lipid bilayer. But this is not the case in our simulations; for distances far away from the protein the thickness profiles do not reach the value for the undisturbed bilayer thickness. In this section we investigate the thickness profiles on the one hand for different system sizes and and on the other hand for different amounts of solvent beads, and analyse the reason for this thickness thinning behaviour. First of all we vary the number of lipids and solvent beads: (i) 776 lipids and 6153 solvent beads, (ii) 1776 lipids and 13846 solvent beads, and (iii) 3176 lipids and 24615 solvent beads, figure 6.6.

The thickness profiles for these different system sizes exhibit the same oscillatory behaviour independently of the system size. However, with decreasing system size the value for the bilayer thickness far away from the protein decreases. For the two

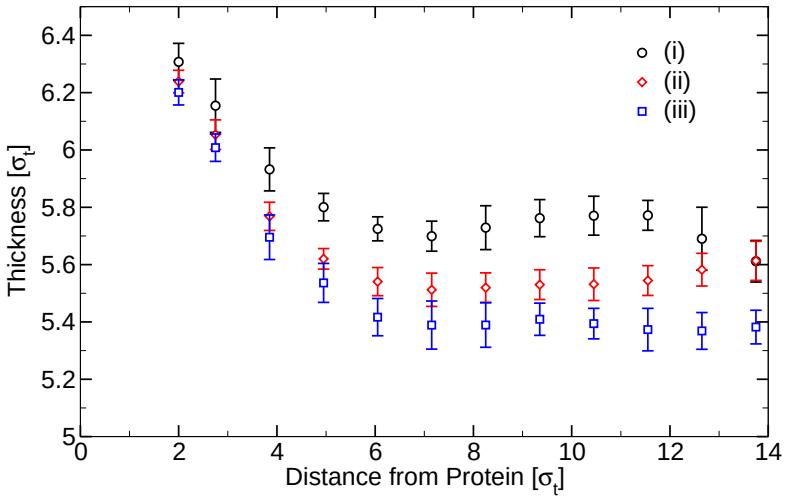

Figure 6.7: Radial membrane thickness profiles of a lipid bilayer with 776 lipids and different amounts of solvent beads in the vicinity of a protein of hydrophobic length $L = 6\sigma_t$ and a hydrophobicity parameter $\epsilon_{pt} = 6.0$: (i) 6153 solvent beads (black circles), (ii) 12307 solvent beads (red diamonds), and (iii) 18461 solvent beads (blue squares).

larger system the asymptotic thickness is about $5.9 - 6.0\sigma_t$. For the system with 776 lipids the asymptotic thickness is about $5.7 - 5.8\sigma_t$. Between the smallest and the largest system the thickness difference is very obvious and beyond the error of the simulation.

As a next step we vary the amount of solvent beads for the system with 776 lipids: (i) 6153 solvent beads, (ii) 12307 solvent beads, and (iii) 18461 solvent beads, figure 6.7. For these simulations we set the hydrophobic length of the protein $L = 6\sigma_t$ and the hydrophobicity parameter $\epsilon_{pt} = 6.0$. With increasing number of solvent beads the thickness far away from the protein decreases. The only difference between the three systems is the amount of solvent beads and with this the length of the simulation box in z-direction. Since the length of the protein cylinder is equal to the simulation box in z-direction, L_z, the solvent beads can not occupy the whole volume of the simulation box. This excluded volume increases with increasing number of solvent beads. The change in free energy $\mathcal{F}$ of the protein-solvent system is:

$$\mathcal{F}(Z, A, N_s) = -k_B T N_s \ln\left(\int dr e^{-\beta U(r)}\right) \tag{6.2}$$

$$= -k_B T N_S \ln\left(AZ + 2\pi \int r dr \left(e^{-\beta U(r)} - 1\right) Z\right) \tag{6.3}$$

$$= -k_B T N_s \ln\left((A - A_0) Z\right) \tag{6.4}$$

$$= -k_B T N_s \left(\ln(A) + \ln(1 - A_0/A) + \ln(Z)\right) \tag{6.5}$$

$$\simeq -k_B T N_s \left(\ln(A) - A_0/A + \ln(Z)\right) \quad . \tag{6.6}$$

N_s is the number of solvent beads and $A = L_x L_y$ is the area of the system. $Z = L_z - d$ is the length of the simulation box that is occupied by the solvent with d the thickness of the lipid bilayer. The solvent volume is $V_s = A \cdot Z$. We have set $A_0 := 2\pi \int r dr(\exp(-\beta U(r)) - 1)$ with $U(r)$ the interaction potential between protein and solvent beads. For a protein of diameter $\sigma_p = 3\sigma_t$ one has $A_0 \simeq 4\pi\sigma_t^2$.

The pressure is the derivative of the free energy $\mathcal{F}$ with respect to the volume V:

$$P = -\frac{\partial \mathcal{F}}{\partial V} \quad . \tag{6.7}$$

Applying this relation on equation 6.6 we get

$$P_N = -\frac{1}{A}\frac{\partial \mathcal{F}}{\partial Z} = \frac{k_B T N_s}{AZ} \tag{6.8}$$

$$P_T = -\frac{1}{Z}\frac{\partial \mathcal{F}}{\partial A} = \frac{k_B T N_s}{ZA} + \frac{k_B T N_s A_0}{ZA^2} \tag{6.9}$$

for the normal and tangential component of the pressure, P_N and P_T. The difference of the normal and tangential component is

$$P_N - P_T = -\frac{k_B T N_s}{AZ}\frac{A_0}{A} \quad . \tag{6.10}$$

Each protein incorporated into the lipid bilayer contributes this amount to the total pressure difference of the system. The tension is obtained by integrating the pressure difference over the z-direction:

$$\Gamma = -\int_0^{L_z} \frac{k_B T N_s}{AZ}\frac{A_0}{A} dz \tag{6.11}$$

$$= -\frac{k_B T N_s}{AZ}\frac{A_0}{A} L_z \tag{6.12}$$

$$= -P\frac{A_0}{A} L_z \quad . \tag{6.13}$$

In the last equation we have inserted the ideal gas law: $PV_s = k_B T N_s$ with P the pressure applied to the system. This (local) tension induced by the excluded volume effect has to be balanced by the lipid bilayer resulting in a positive tension inside the lipid bilayer so that the whole system is in a tension-free state. This positive tension induces a thinning of the bilayer thickness. Figure 6.8 (obtained from Jörg Neder) shows the mean thickness of a pure lipid bilayer as a function of the tension of the system. There is a linear dependence of the bilayer thickness from the tension of the system.

Table 6.3 shows the theoretical values, calculated according to equation 6.13, and measured values for the tension of the system with 776 lipids, one protein and different numbers of solvent beads. In order to measure the tension far away from the protein we have two options. One possibility is to measure the tension profile in a thin rectangular slice of the simulation box which is far away from the protein. If

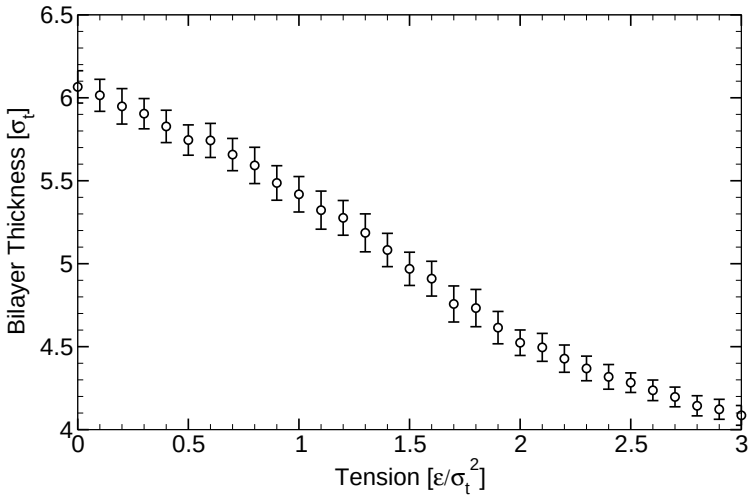

Figure 6.8: Mean bilayer thickness of a pure lipid bilayer as a function of the tension of the system (data obtained from Jörg Neder)

N_s	V_s $[\sigma_t^3]$	A $[\sigma_t^2]$	L_z $[\sigma_t]$	$2t_0$ $[\sigma_t]$	Γ_t $[\epsilon/\sigma_t^2]$	Γ_s $[\epsilon/\sigma_t^2]$	Γ_c $[\epsilon/\sigma_t^2]$
6153	4000	578	14.9	5.74	0.65	0.6 ± 0.2	0.5 ± 0.1
12307	8000	597	21.1	5.58	0.89	0.8 ± 0.2	0.9 ± 0.1
18461	12000	617	27	5.42	1.1	1.0 ± 0.2	1.3 ± 0.1

Table 6.3: System with 776 lipids, one protein and different numbers of solvent beads N_s (solvent volume V_s): Collection of the values for the area $A = L_x L_y$ and z-length of the simulation box, L_z. The thickness $2t_0$ is the thickness of the lipid bilayer far away from the protein. Γ_t is the theoretical value of the membrane tension calculated according to equation 6.13. Γ_s and Γ_c are the tension measured in a thin rectangular slice (s) and in a cylinder (c) as described in the text.

both particles are inside the rectangular slice, the pressure tensor can be calculated as described in section 4.2. If one bead is inside and the other outside the rectangular slice, the point of intersection between the connection line between the two beads and the rectangle is calculated. The weight function, equation 4.11, is applied to the connection line between the point of intersection and the bead inside the rectangular slice. The other possibility is to measure the tension as a function of the distance from the protein. In this case the tension is measured in concentric cylinders around the protein. The connection line between two beads is calculated, and we analyse how much of this line falls into every cylinder. For the tension we take the last cylinder's value which is completely within the simulation box. For cylinders partly outside the simulation box we get an uncertainty due to the periodic boundary conditions. The two methods give results of the same order. The measured value for the tension corresponds within the uncertainty to the calculated values of the tension. If we compare

the measured values for the thickness far away from the protein and the corresponding tension of our simulations to the data of figure 6.8, we see that they correspond very well.

Appendix C.1 gives a summary of the simulations carried out in systems of different sizes for different values of the hydrophobic length of the protein and different values of the hydrophobicity parameter.

6.3 Comparison between Different Protein Diameters

In this section we compare the thickness profile for a system with a protein which corresponds to a β-helix of diameter $\sigma_p = 3\sigma_t \simeq 18$Å with the thickness profile obtained for a protein of diameter $\sigma_p = 1\sigma_t \simeq 6$Å corresponding to an α-helix. We use the label "thick protein" for the protein of diameter $\sigma_p = 3\sigma_t$ and the label "thin protein" for the protein of diameter $\sigma_p = 1\sigma_t$. Like in the case of the thick protein two parameters are varied: the hydrophobic length L of the protein, $L = 4\sigma_t$, $6\sigma_t$, $8\sigma_t$, and the hydrophobicity parameter ϵ_{pt}, $\epsilon_{pt} = 1.0$, 6.0. Figure 6.9 shows the radial thickness profiles as a function of the distance from the protein together with the fit to the elastic theory, equation 2.15 with the boundary condition 2.29. The profiles show the same non-monotonic oscillatory behaviour as in the case of the thick protein. For a hydrophobicity $\epsilon_{pt} = 1.0$ the lipids get repelled, and for $\epsilon_{pt} = 6.0$ the tail-protein interaction is strong enough to produce hydrophobic mismatch. The fit parameters of the elastic theory are summarised in table 6.4. Like in the case of the thick protein none of the values for the renormalised curvature agrees with the value of the spontaneous curvature we measured from the tension profile. The effective hydrophobic length of the protein L_{eff} corresponds within $1\sigma_t$ to the values of L.

Comparing the thickness profiles of the thin protein to the thickness profiles of the thick protein, we see that the lipids get much more repelled in the case of the thick protein. For a hydrophobicity of $\epsilon_{pt} = 1.0$ the bilayer thickness in contact with the protein is between $3 - 4\sigma_t$ for the thick protein and between $4 - 5\sigma_t$ for the thin protein. The overshooting seems a little more distinct in the case of the thick protein. For $\epsilon_{pt} = 6.0$ the profiles for the thin protein look as if they have just been shifted. The thickness of the bilayer in contact with the protein is slightly higher in the case of positive hydrophobic mismatch, and in the case of negative hydrophobic mismatch the thickness of the bilayer in contact with the protein is a bit smaller. As expected the thickness far away from the protein in the case of the thin protein is larger than in the case of the thick protein. The renormalised curvature is much smaller in the case of the thin protein as in the case of the thick protein. If we fit the data for $\epsilon_{pt} = 6.0$ to the Landau-de Gennes theory, table 6.5, the decay length is slightly smaller compared to the decay length in the case of the thick protein. The fact that the perturbation length does not vary much with the inclusion's radius, was also observed in other coarse-grained simulations [41]. For a radius $R_{LdG} = 0.5\sigma_t$ the effective hydrophobic length of the protein differs considerably from the actual value. For a radius $R_{LdG} = 1.0\sigma_t$ it is within $1\sigma_t$ close to the actual value.

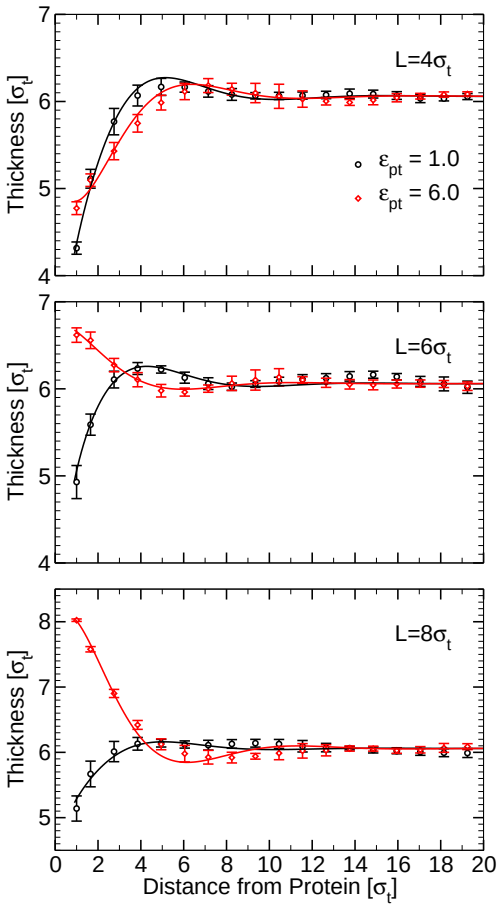

Figure 6.9: Radial membrane thickness profiles in the vicinity of a protein with diameter $\sigma_p = 1.0\sigma_t$. The hydrophobic length of the protein is $L = 4\sigma_t$ (upper panel), $L = 6\sigma_t$ (middle panel), $L = 8\sigma_t$ (lower panel) and the hydrophobicity parameter is $\epsilon_{pt} = 1.0$ (black circles) and $\epsilon_{pt} = 6.0$ (red diamonds). The solid lines show the fit to the elastic theory, equation 2.15 with the boundary condition 2.29.

The quantity A_0 in equation 6.13 depends on the diameter of the protein and with this also the induced tension. A_0 is about $4\pi\sigma_t^2$ for a protein of diameter $3\sigma_t$ and $2\pi\sigma_t^2$ for a protein of diameter $1\sigma_t$. In the case of the thick protein the induced tension shows a very strong dependence on the system size. The asymptotic bilayer thickness increases clearly with increasing system size. In the case of the thin protein the system size dependence is not so distinct, appendix C.2. The asymptotic bilayer thickness almost agrees for the two different system sizes.

As a last point we want to look at the radial profiles of other quantities rather than the thickness, figures 6.10 and 6.11. If we compare these profiles to the profiles of a thick protein, figures 6.5 and 6.4, we see that the diameter does not have much

		$R_{el} = 0.5\sigma_t$			
$L\ [\sigma_t]$	ϵ_{pt}	$t_R\ [\sigma_t]$	$L_{eff}\ [\sigma_t]$	$\tilde{c}_0\ [\sigma_t^{-1}]$	
4	1.0	-1.19	3.68	-0.04	$[0.32 \ldots -0.48]$
4	6.0	-0.55	4.96	-0.21	$[-0.33 \ldots -0.07]$
6	1.0	-0.86	4.34	0.06	$[0.46 \ldots -0.42]$
6	6.0	0.34	6.74	0.07	$[0.05 \ldots 0.09]$
8	1.0	-0.56	4.94	-0.01	$[0.17 \ldots -0.23]$
8	6.0	1.02	8.1	0.27	$[0.31 \ldots 0.22]$

		$R_{el} = 1.0\sigma_t$			
$L\ [\sigma_t]$	ϵ_{pt}	$t_R\ [\sigma_t]$	$L_{eff}\ [\sigma_t]$	$\tilde{c}_0\ [\sigma_t^{-1}]$	
4	1.0	-0.85	4.36	0.01	$[0.13 \ldots -0.13]$
4	6.0	-0.6	4.86	-0.1	$[-0.09 \ldots -0.11]$
6	1.0	-0.5	5.06	0.06	$[0.17 \ldots -0.07]$
6	6.0	0.3	6.6	0.03	$[0.01 \ldots 0.05]$
8	1.0	-0.39	5.28	0.01	$[0.07 \ldots -0.06]$
8	6.0	0.98	8.02	0.12	$[0.08 \ldots 0.17]$

Table 6.4: Fit of the radial thickness profiles to the elastic theory: t_R (monolayer deformation at the surface of the protein), L_{eff} (effective hydrophobic length of the protein), $\tilde{c}_0$ (renormalised curvature). The radius is set to $R_{el} = 0.5\sigma_t$ and $1.0\sigma_t$, respectively. The asymptotic value for the monolayer thickness is $t_0 = 3.03\sigma_t$. The value of the renormalised curvature belongs to a Gaussian rigidity $k_G = -0.26\epsilon$. The values in case the Gaussian rigidity is changed within its error are in brackets.

	$R_{LdG} = 0.5\sigma_t$		$R_{LdG} = 1.0\sigma_t$	
$L\ [\sigma_t]$	$t_R\ [\sigma_t]$	$L_{eff}\ [\sigma_t]$	$t_R\ [\sigma_t]$	$L_{eff}\ [\sigma_t]$
4	-1.51	3.04	-0.88	4.3
6	0.74	7.54	0.43	6.92
8	2.33	10.72	1.36	8.78

Table 6.5: Fit of the radial thickness profiles for the $\epsilon_{pt} = 6.0$ data to the Landau-de Gennes theory: t_R (monolayer deformation at the surface of the protein), L_{eff} (effective hydrophobic length of the protein). The radius R_{LdG} in equation 2.7 is set to $0.5\sigma_t$ and $1.0\sigma_t$, respectively. The asymptotic monolayer thickness is $t_0 = 3.03\sigma_t$. The decay length is $\zeta = 1.8 \pm 0.1\sigma_t$.

influence on the characteristics of these profiles. Small differences are only observed in the case of a hydrophobicity parameter $\epsilon_{pt} = 1.0$ for the behaviour of the bond order parameter. The length of the lipids in direct contact to the protein is more or less constant, they are perhaps a little bit stretched. In the case of the thick protein the lipids are compressed. For distances larger than about $10\sigma_t$ from the protein, the

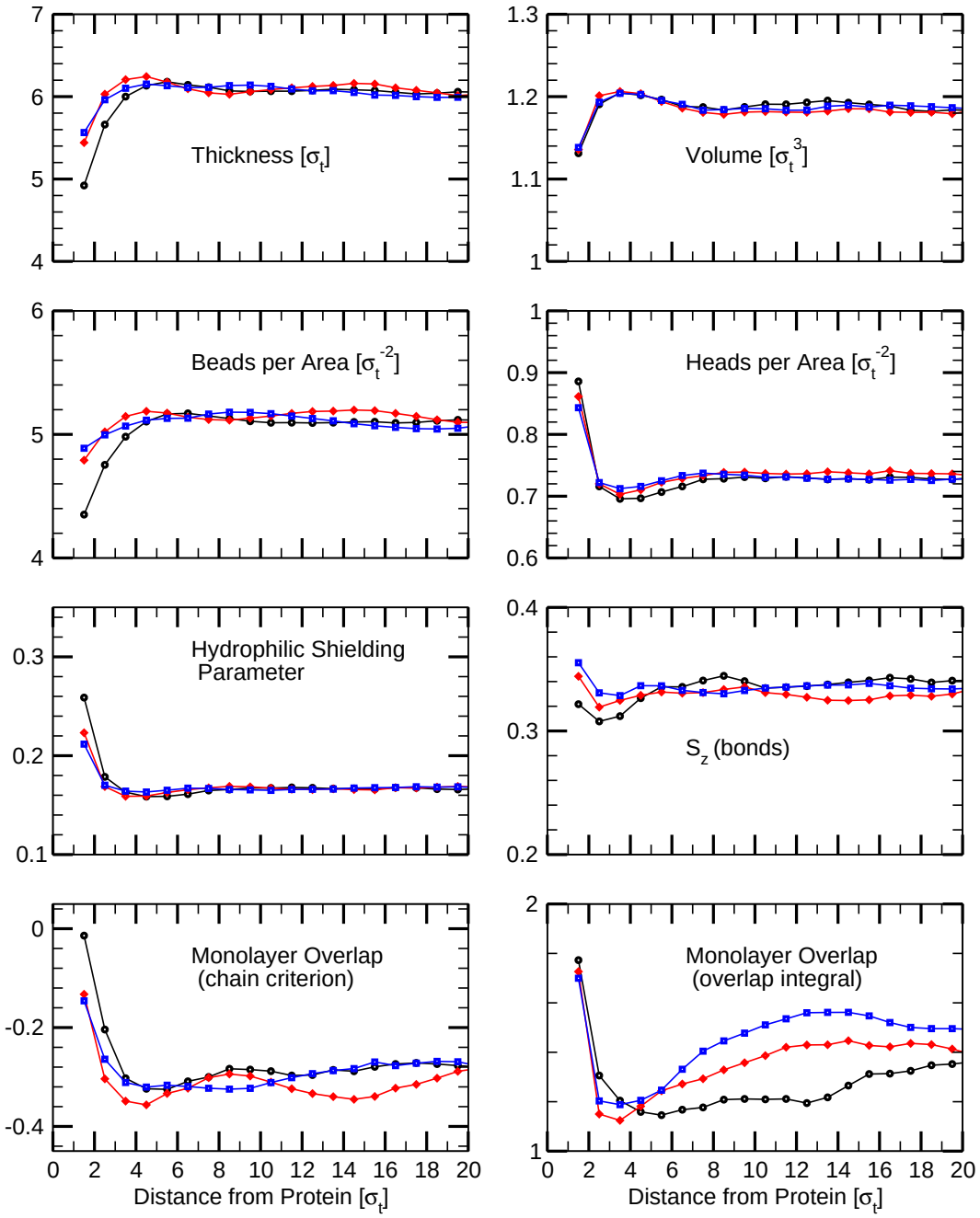

Figure 6.10: Radial profiles of various quantities as a function of the distance from the centre of a thin protein with hydrophobic thickness $L = 4\sigma_t$ (black circles), $L = 6\sigma_t$ (red diamonds), and $L = 8\sigma_t$ (blue squares) and a hydrophobicity parameter $\epsilon_{pt} = 1.0$

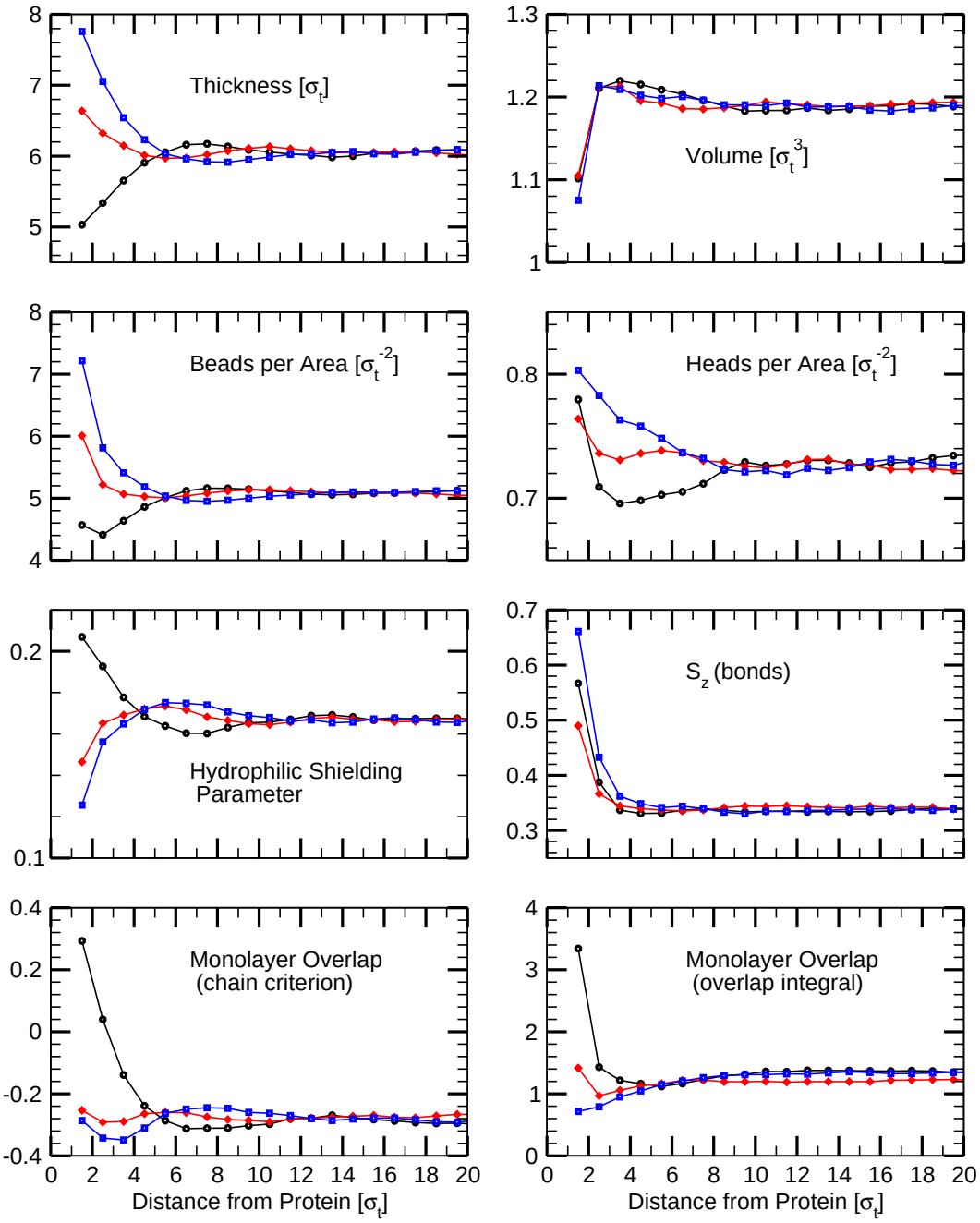

Figure 6.11: Radial profiles of various quantities as a function of the distance from the centre of a thin protein with hydrophobic thickness $L = 4\sigma_t$ (black circles), $L = 6\sigma_t$ (red diamonds), and $L = 8\sigma_t$ (blue squares) and a hydrophobicity parameter $\epsilon_{pt} = 6.0$

bond order parameter shows the same behaviour for the thin and the thick protein.

6.4 Protein with Tilt

In the simulations presented so far the protein is oriented along the z-axis. In the protein model with tilt the long cylinder which covers the whole z-axis is exchanged with a sphero-cylinder. Simulation runs in systems of different sizes with the sphero-cylinder show that the system size does not have an influence on the simulation results. The thickness of the lipid bilayer measured far away from the protein is equal within the error for different system sizes and corresponds to the value of an undisturbed lipid bilayer. This is expected, because the induced tension is a result of an excluded volume effect that is not present in the case of the sphero-cylinder proteins. As before we change the hydrophobic length of the protein L, $L = 4\sigma_t$, $6\sigma_t$, $8\sigma_t$ as well as the hydrophobicity parameter ϵ_{pt}, $\epsilon_{pt} = 1.0$, 6.0. The protein diameter σ_p is set to $\sigma_p = 1\sigma_t$ and $\sigma_p = 3\sigma_t$.

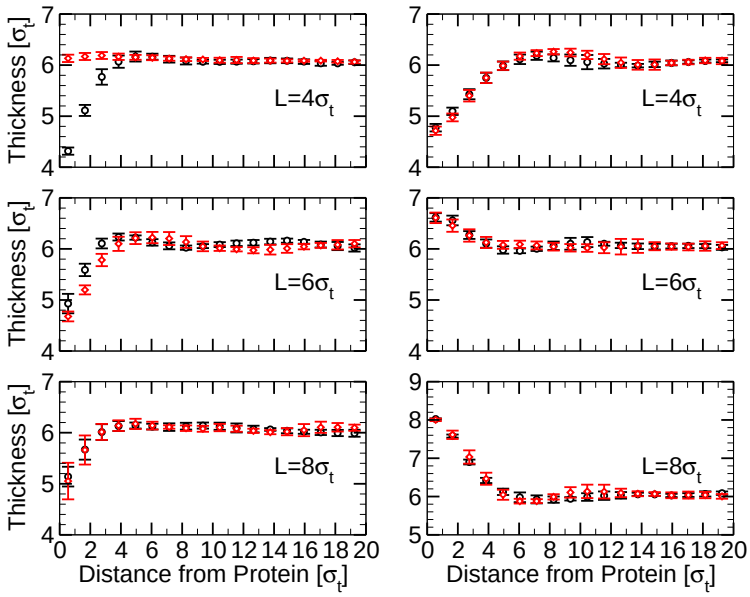

Figure 6.12: Comparison of the radial thickness profiles in the vicinity of a protein of diameter $\sigma_p = 1\sigma_t$ with a length equal to the z-length of the simulation box (black circles) and a protein of finite length, which is allowed to tilt (sphero-cylinder, red diamonds). The hydrophobicity parameter is $\epsilon_{pt} = 1.0$ (left) and $\epsilon_{pt} = 6.0$ (right). The hydrophobic length of the protein is $L = 4\sigma_t$, $6\sigma_t$, $8\sigma_t$ (from top to bottom). The data are obtained from a system with 3194 lipids.

The thickness profiles of a system containing one sphero-cylinder protein, regardless whether it is allowed to tilt or not, show only few differences from the thick-

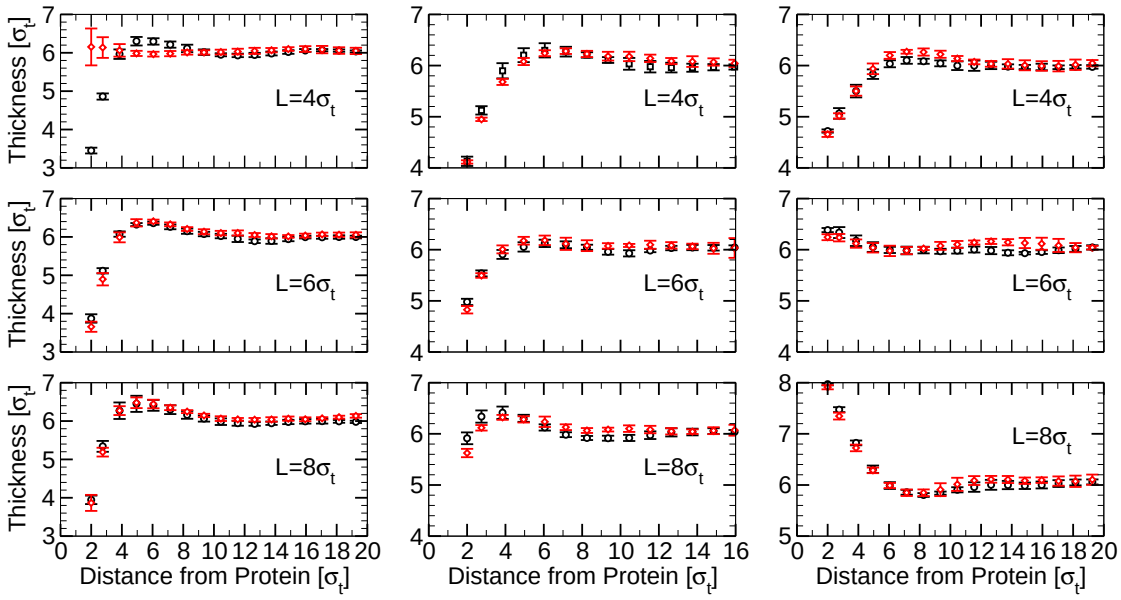

Figure 6.13: Comparison of the radial thickness profiles in the vicinity of a protein of diameter $\sigma_p = 3\sigma_t$ with a length equal to the z-length of the simulation box (black circles) and a protein of finite length, which is allowed to tilt (sphero-cylinder, red diamonds). The hydrophobicity parameter is $\epsilon_{pt} = 1.0$ (left), $\epsilon_{pt} = 2.0$ (middle) and $\epsilon_{pt} = 6.0$ (right). The hydrophobic length of the protein is $L = 4\sigma_t$, $6\sigma_t$, $8\sigma_t$ (from top to bottom). The data for $\epsilon_{pt} = 2.0$, where the protein is allowed to tilt, are obtained for a system with 776 lipids. All other data are obtained from a system with 3176 lipids.

ness profiles of a system containing one large protein. Figures 6.12 and 6.13 show a comparison between the thickness profiles of a long protein with length equal to L_z oriented along the z-axis and a sphero-cylinder protein which is allowed to tilt. The protein diameter is $\sigma_p = 1\sigma_t$ and $\sigma_p = 3\sigma_t$, respectively. The profiles show the same characteristics within the error. The only exception is the thickness profile for a sphero-cylinder protein of hydrophobic length $L = 4\sigma_t$ and a hydrophobicity parameter $\epsilon_{pt} = 1.0$. In this case the binding force between the lipid bilayer and the protein is not strong enough to keep the protein inside the lipid bilayer – the protein "swims" in a straight conformation on the lipid bilayer with only a part of the protein touching the lipid bilayer. This is not an effect of the rotational degree of freedom, but of the finite protein length. We have done simulations in order to check this for the sphero-cylinder protein, where on the one hand the protein is allowed to tilt and on the other hand is aligned along the z-axis. The last point is realised by setting the possible tilt range of the protein to zero. In some of the simulation runs the protein remained inside the lipid bilayer, whereas in other simulation runs the protein left the lipid bilayer. This is independent of whether the protein is allowed to tilt and also

		$\sigma_p = 3\sigma_t$		$\sigma_p = 1\sigma_t$	
L $[\sigma_t]$	ϵ_{pt}	θ(776 lipids) [°]	θ(3176 lipids) [°]	θ(794 lipids) [°]	θ(3194 lipids) [°]
4	1.0	4.63	6.12	13.4	12.55
4	2.0	4.64		8.13	
4	6.0	2.71	3.02	4.71	4.37
6	1.0	3.15	3.12	5.23	5.17
6	2.0	2.69		4.5	
6	6.0	1.52	1.48	2.23	2.27
8	1.0	2.17	2.19	3.86	3.44
8	2.0	1.75		2.44	
8	6.0	0.97	0.96	1.45	1.46

Table 6.6: Maximal tilt angle θ for one sphero-cylinder protein of diameter $\sigma_p = 3\sigma_t$ and $\sigma_p = 1\sigma_t$, respectively. The rotation angle ϕ is between $[-\pi, \pi]$. For $L = 4\sigma_t$ and $\epsilon_{pt} = 1.0$ the protein left the lipid bilayer.

independent of the system size. A hydrophobicity parameter of $\epsilon_{pt} = 2.0$ is sufficient to keep the protein within the lipid bilayer. Figure 6.13 shows this for the case of a protein diameter $\sigma_p = 3\sigma_t$. In this case the simulations were carried out in a system with 776 lipids. All other simulations were carried out in systems with 3176 lipids.

The reason why the possible tilt has no influence on the thickness profiles is that the maximal protein tilt angle is very small. It is always less than 15° and 10° for a protein of diameter $\sigma_p = 1\sigma_t$ and $\sigma_p = 3\sigma_t$, respectively, cf. table 6.6. The tilt angle is larger for the thin protein compared to the thick protein. This effect was also observed by Venturoli et al. [115] in the case of a transmembrane protein and by Nielsen et al. [89] in the case of a transmembrane nanotube. For a fixed hydrophobic length the tilt angle decreases with the increase of the hydrophobicity parameter. For a fixed hydrophobicity parameter the tilt angle decreases with increasing hydrophobic length of the protein. This is in contrast to the observations of Venturoli et al. but agrees with the observations of Jörg Neder, who models the protein as a bead object [85]. In agreement with Venturoli et al. he observes that a further increase in the hydrophobic length, $L = 10\sigma_t$, results in an increase of the tilt angle.

Figures 6.14 and 6.15 show the radial profiles of some interesting quantities as a function of the distance from the protein for a hydrophobicity parameter $\epsilon_{pt} = 1.0$. For a hydrophobic length $L = 6\sigma_t$ and $8\sigma_t$ the profiles are within the uncertainty equal to the profiles obtained for a long protein with length equal to L_z. In case of the protein swimming on the lipid bilayer the profiles show the behaviour that we would except for a lipid bilayer without any proteins. The only exception are the profiles for the beads per area and the heads per area. In this case there is a little enrichment of beads and heads, respectively, around the protein. This can be explained by the fact that even though the protein is not fully inside the lipid bilayer, some part is still inside the lipid bilayer interacting with the lipids.

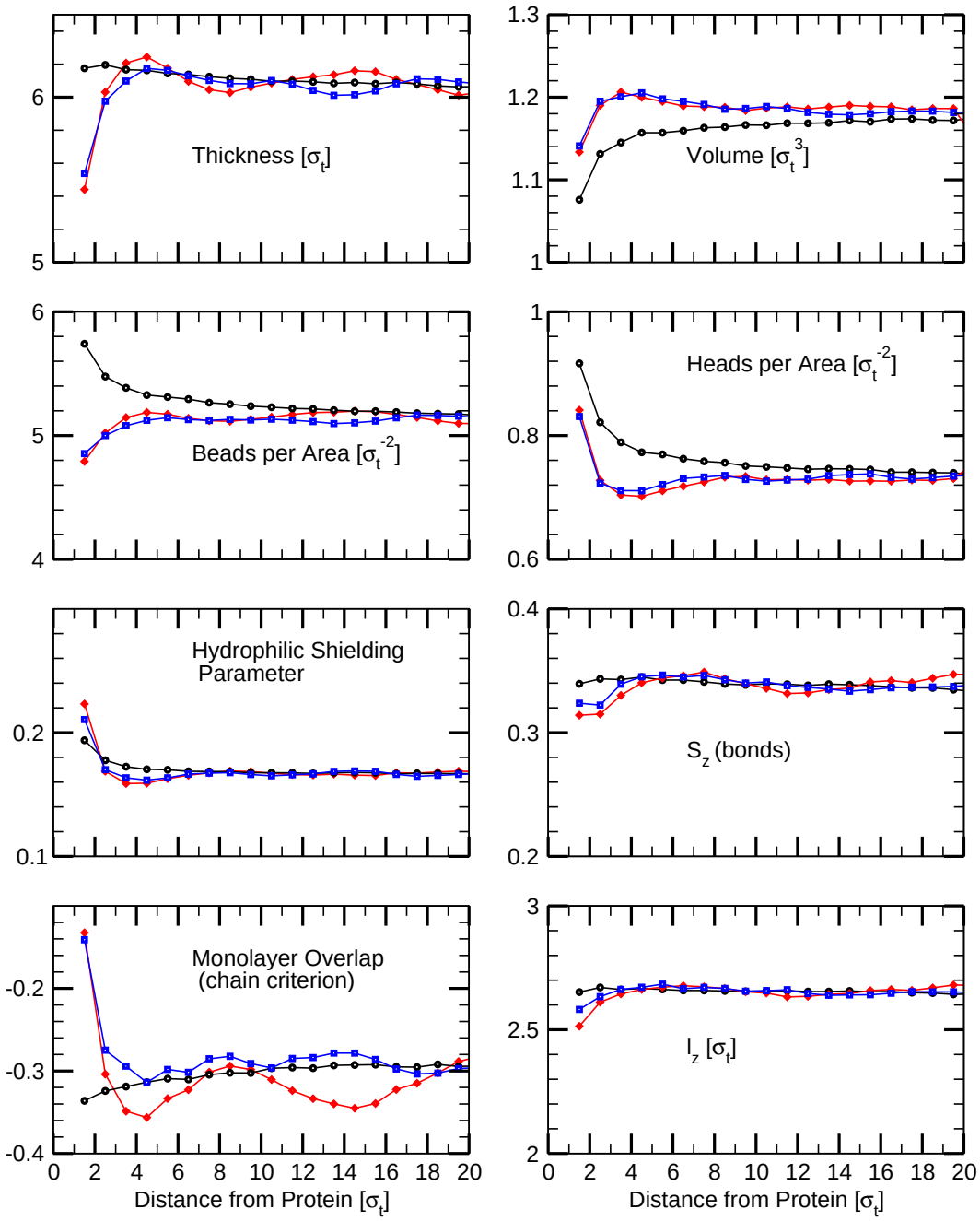

Figure 6.14: Protein of diameter $\sigma_p = 1\sigma_t$, which is allowed to tilt (sphero-cylinder protein): radial profiles of various quantities as a function of the distance from the centre of the protein. The hydrophobic length is $L = 4\sigma_t$ (black circles), $L = 6\sigma_t$ (red diamonds), and $L = 8\sigma_t$ (blue squares) and the hydrophobicity parameter is $\epsilon_{pt} = 1.0$.

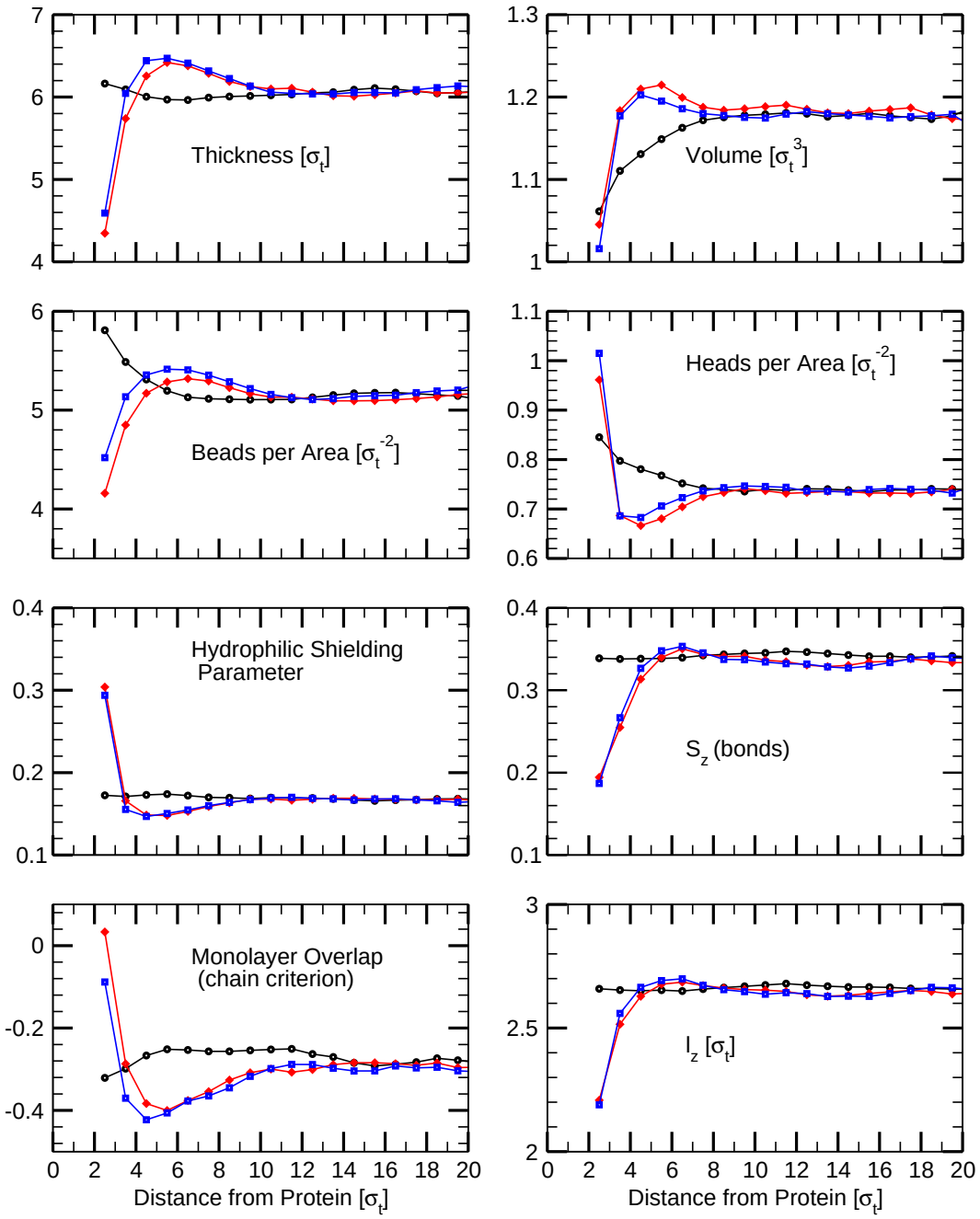

Figure 6.15: Protein of diameter $\sigma_p = 3\sigma_t$, which is allowed to tilt (sphero-cylinder protein): radial profiles of various quantities as a function of the distance from the centre of the protein. The hydrophobic length of the protein is $L = 4\sigma_t$ (black circles), $L = 6\sigma_t$ (red diamonds), and $L = 8\sigma_t$ (blue squares) and the hydrophobicity parameter is $\epsilon_{pt} = 1.0$.

6.5 Calculation of the Free Energy Using Thermodynamic Integration

The incorporation of one or more proteins into a lipid bilayer leads to a change in the free energy. One possibility to measure the change in free energy is to try to bring a protein inside a bilayer without taking lipids out and then measuring the difference in energy. Since this is very difficult to do within the simulation [85], we use the method of thermodynamic integration [119].

The free energy $\mathcal{F}$ is defined in terms of the partition function Z_K:

$$\mathcal{F} = -k_B T \ln(Z_K) \tag{6.14}$$

$$Z_K = \frac{1}{h^{3N} N!} \int_\Omega e^{-\frac{\mathcal{H}(\Gamma)}{k_B T}} d\Gamma \quad . \tag{6.15}$$

$\mathcal{H}$ is the Hamiltonian which depends, in our case, only on the configuration of the system and is thus identical to the potential energy of the system:

$$\mathcal{H}(\Gamma) = \mathcal{H}\left(\mathbf{r}^N\right) = \sum_{i<j} U_{ij}\left(\mathbf{r}^N\right) + \sum_i U_{ip}\left(\mathbf{r}^N\right) \quad . \tag{6.16}$$

The potential energy has a contribution from the bead-bead interaction U_{ij} and a contribution from the bead-protein interaction U_{ip}. The idea is to rescale the bead-protein interaction by a factor α, $0 \leq \alpha \leq 1$. Depending on α the bead-protein interaction then is between zero for $\alpha = 0$ and the original value of U_{ip} for $\alpha = 1$. We substitute the bead-protein potential U_{ip} by a new potential $\tilde{U}_{ip}$:

$$\tilde{U}_{ip}\left(\mathbf{r}^N, \alpha\right) = -\ln\left(1 + \alpha\left(e^{-U_{ip}\left(\mathbf{r}^N\right)} - 1\right)\right) \quad . \tag{6.17}$$

The Hamiltonian now has the form

$$\mathcal{H}\left(\mathbf{r}^N, \alpha\right) = \sum_{i<j} U_{ij}\left(\mathbf{r}^N\right) + \sum_i \tilde{U}_{ip}\left(\mathbf{r}^N, \alpha\right) \quad . \tag{6.18}$$

Figure 6.16 shows the run of the "rescaled" Lennard-Jones potential for different values of α. The change in the free energy $\mathcal{F}$ is

$$\Delta\mathcal{F} = \int_0^1 \frac{\partial \mathcal{F}}{\partial \alpha} d\alpha - \Delta \tag{6.19}$$

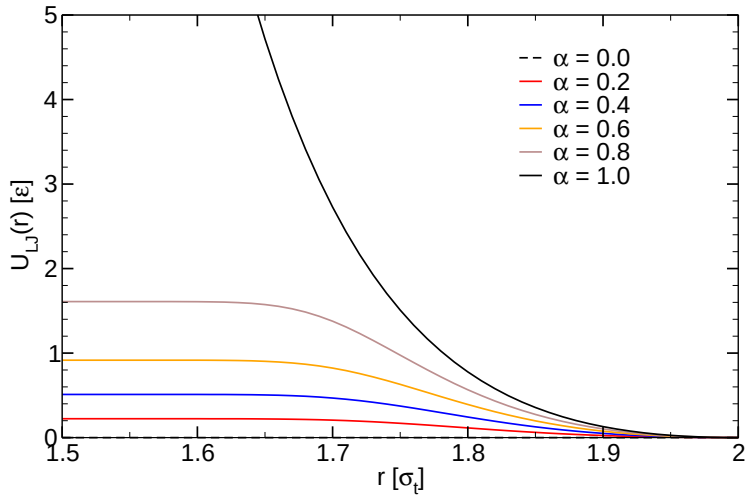

Figure 6.16: Rescaled Lennard-Jones potential, equation 6.17, with $r_c = \sigma_t$, $\sigma = 2$ for different values of α

with

$$\frac{\partial \mathcal{F}\left(\mathbf{r}^N, \alpha\right)}{\partial \alpha} = -k_B T \frac{\partial \ln Z_K\left(\mathbf{r}^N, \alpha\right)}{\partial \alpha} \tag{6.20}$$

$$= \frac{1}{h^{3N} N! Z_K} \int_\Omega d\Gamma \frac{\partial \mathcal{H}\left(\mathbf{r}^N, \alpha\right)}{\partial \alpha} \exp\left(-\frac{\mathcal{H}\left(\mathbf{r}^N, \alpha\right)}{k_B T}\right) \tag{6.21}$$

$$= \left\langle \frac{\partial \mathcal{H}\left(\mathbf{r}^N, \alpha\right)}{\partial \alpha} \right\rangle \tag{6.22}$$

$$= \left\langle \sum_i \frac{\partial \tilde{U}_{ip}\left(\mathbf{r}^N, \alpha\right)}{\partial \alpha} \right\rangle \tag{6.23}$$

$$= \left\langle \sum_i \frac{1 - e^{-U_{ip}\left(\mathbf{r}^N\right)}}{1 + \alpha\left(e^{-U_{ip}\left(\mathbf{r}^N\right)} - 1\right)} \right\rangle \tag{6.24}$$

and $\Delta \simeq 178$ the change in free energy for a free protein (equation 6.4)

$$\Delta = -k_B T N_s \ln(V_s - A_0(L_z - d)) + k_B T N_s \ln(V_s) \quad . \tag{6.25}$$

For our simulations we used an equilibrated configuration with 776 lipids, 6153 solvents and one protein with length equal to L_z and a hydrophobic length $L = 6\sigma_t$. We did independent simulation runs with different values for α. Figure 6.17 shows the mean value of the bead-protein interaction and the parameter $\partial\mathcal{F}/\partial\alpha$, calculated according to equation 6.24, for different values of ϵ_{pt}. The mean value of the bead-protein interaction energy is between zero for $\alpha = 0$ and the original value of the

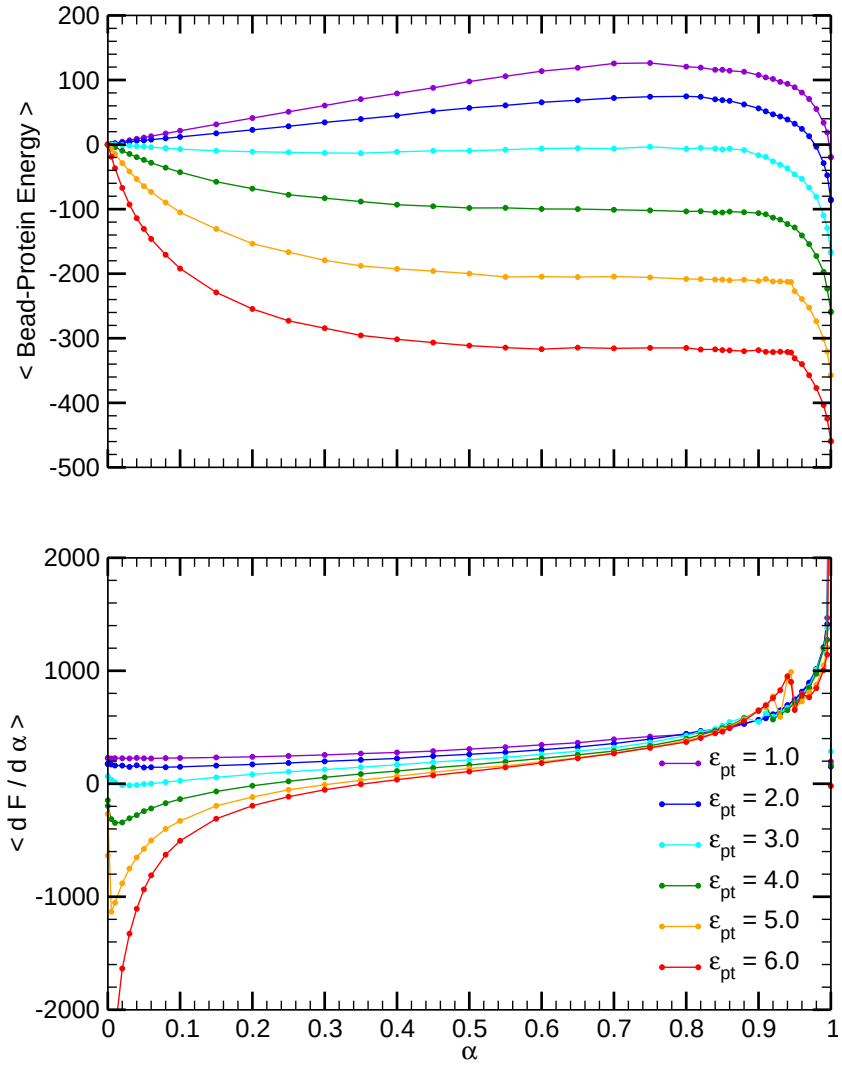

Figure 6.17: Mean rescaled bead-protein interaction for different values of the hydrophobicity parameter ϵ_{pt} as a function of α (top panel). Mean value of the derivative of the free energy after α for different values of the hydrophobicity parameter ϵ_{pt} as a function of α (bottom panel).

interaction energy for $\alpha = 1$. $\partial\mathcal{F}/\partial\alpha$ is monotonic for all values of ϵ_{pt} between $0.1 \leq \alpha \leq 0.9$. For very small and very large values of α the curve diverges. For a hydrophobicity parameter between $\epsilon_{\mathrm{pt}} = 4.0$ and 6.0 something happens in $\mathrm{d}\mathcal{F}/\mathrm{d}\alpha$: There is a step in the curves for approximately $\alpha = 0.95$. Normally such a step indicates a phase transition. Since we have a system of finite size this can not be the case. It is not clear what happens in the system. The values for the change in free energy $\Delta\mathcal{F}$ are collected in table 6.7. The change in free energy is large for small ϵ_{pt} and decreases for increasing hydrophobicity. $\Delta\mathcal{F}$ gets negative at about that value of ϵ_{pt},

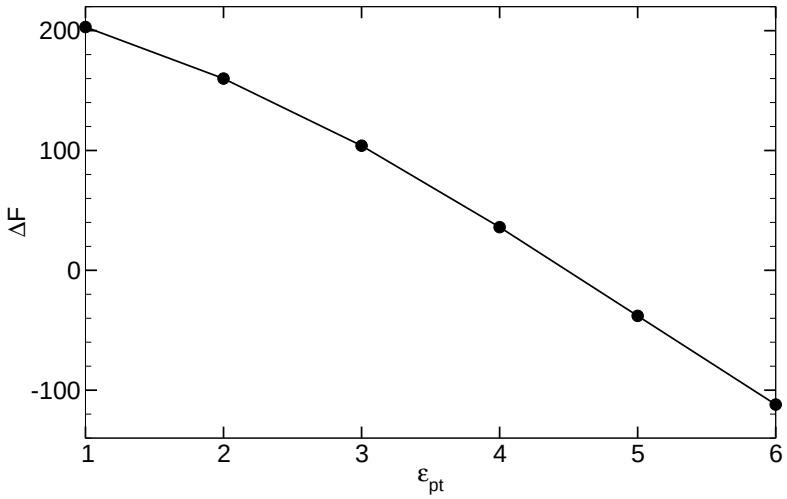

Figure 6.18: Change in free energy $\Delta\mathcal{F}$ as a function of the hydrophobicity parameter ϵ_{pt}, table 6.7

ϵ_{pt}	1.0	2.0	3.0	4.0	5.0	6.0
$\Delta\mathcal{F}$	203	160	104	36	-38	-112

Table 6.7: Values for the change in free energy $\Delta\mathcal{F}$ depending on the hydrophobicity parameter ϵ_{pt}

where we get a step in $\langle\partial\mathcal{F}/\partial\alpha\rangle$, figure 6.17. For this value of ϵ_{pt} we get an adequate pinning of the lipids. The attractive lipid-protein interaction dominates the repulsive lipid-protein interaction.

Figure 6.19 shows for $\epsilon_{\mathrm{pt}} = 6.0$ the thickness profiles for different values of α. For small values of α the lipids penetrate into the protein. For $\alpha = 0.0$ there is no bead-protein interaction at all and the bilayer shows the behaviour of an undisturbed system. The thickness profile fluctuates a bit, but is more or less constant. With increasing values of α the bilayer thickness far away from the protein decreases until for $\alpha = 1$ the thickness profile has the well-known form. The tension of the system measured in a small rectangular slice increases with increasing bead-protein interaction, because with increasing bead-protein interaction the excluded volume of the solvent beads increases resulting in an increasing tension.

6.6 Conclusions

A protein inserted into a lipid bilayer has a strong influence on the surrounding lipids. The elastic theory with a renormalised curvature in the boundary condition fits the simulation data of the thickness profiles in an excellent way. The fitted renormalised curvature does not agree with the measured spontaneous curvature. The thickness

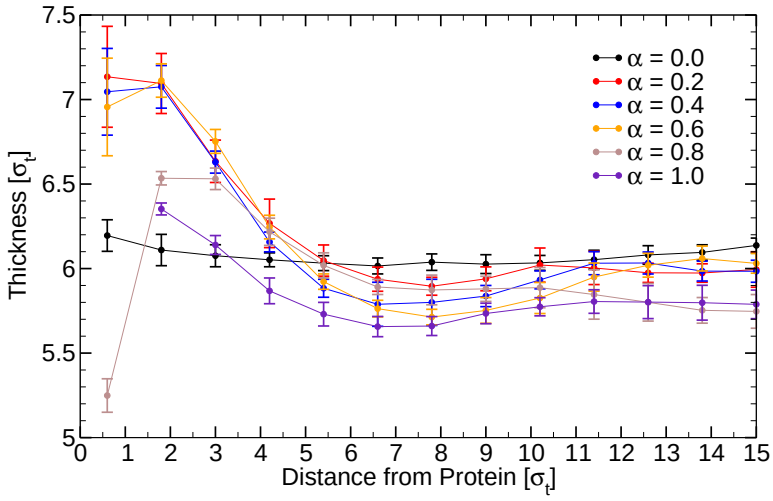

Figure 6.19: Thickness profile for a hydrophobic length $L = 6\sigma_t$ and a hydrophobicity parameter $\epsilon_{pt} = 6.0$ for different values of α. The tension measured in a small rectangular slice is -0.02 ± 0.4, 0.1 ± 0.2, 0.31 ± 0.3, 0.32 ± 0.2, 0.46 ± 0.1, 0.63 ± 0.1 for $\alpha = 0.0$, 0.2, 0.4, 0.6, 1.0, respectively.

profiles as well as the other profiles show the same behaviour for a strong hydrophobicity parameter for different values of the protein diameter. A possible tilt of the protein has no influence on the perturbation of the lipid bilayer because the tilt angle is very small.

7 Lipid Bilayer with Two Proteins in the Fluid Phase

Two proteins inserted into a lipid bilayer do not only interact directly with each other but there are also lipid-mediated interactions. In this chapter we investigate on the one hand the effective pair potential between two proteins and on the other hand the deformations of the lipid bilayer induced by the proteins. All investigations are done for a lipid bilayer in the fluid phase, $P = 2.0\epsilon/\sigma_t^3$, $k_BT = 1.3\epsilon$. The system consists of 744 lipids, 6153 solvent beads and two proteins. The simulations run up to 4 million Monte Carlo steps with equilibration times up to 1 million Monte Carlo steps. Moves altering the simulation box were attempted every 50th Monte Carlo step.

7.1 Effective Interaction between Two Proteins

The effective pair potential between two proteins is measured for different values of the hydrophobic length L of the proteins and the hydrophobicity parameter ϵ_{pt}. Figure 7.1 shows two snapshots of a system containing two proteins. The hydrophobic thickness of the proteins, $L = 6\sigma_t$, roughly matches that of the lipid bilayer. The proteins were set up in a distance equal to their diameter. If the tail-protein interaction is weak, $\epsilon_{pt} = 3.0$, the proteins are pressed together by the lipids. At high tail-protein interactions, $\epsilon_{pt} = 6.0$, the proteins are separated by a single lipid layer.

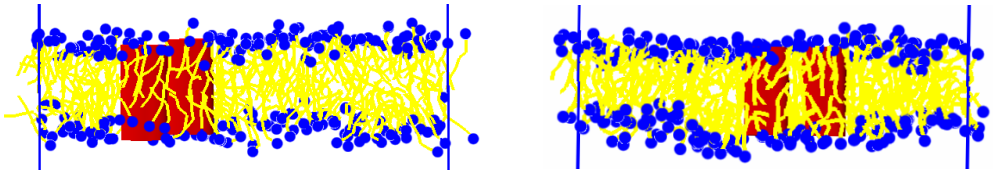

(a) $\epsilon_{pt} = 3.0$ (b) $\epsilon_{pt} = 6.0$

Figure 7.1: Cross-section snapshot of a model membrane with two proteins. The hydrophobic length $L = 6\sigma_t$ roughly matches that of the lipid bilayer. The hydrophobicity parameter is (a) $\epsilon_{pt} = 3.0$, (b) $\epsilon_{pt} = 6.0$. The blue circles are the heads and the yellow lines show the tail bonds. The hydrophobic part of the proteins is represented by the red cylinders. The solvent beads are omitted for clarity.

In order to calculate the effective pair potential $w(r)$ between two proteins we have to determine the radial distribution function $g(r)$ as a function of the protein-protein

distance r:

$$w(r) = -k_B T \ln g(r) \quad . \tag{7.1}$$

The radial distribution function is obtained by an umbrella sampling procedure. We did several independent simulation pre-runs i, where the protein-protein distance r was constrained to stay in a given range $r \in [r_{\min,i}, r_{\max,i}]$. Adjacent windows $[r_{\min}, r_{\max}]$ overlap. From these simulation pre-runs we deduced an estimate for the distribution of distances $h(r)$ in each window. In a second run the simulation in each window was repeated by using $1/h(r)$ as a re-weighting function. This was done to improve the statistics in the valleys. The radial distribution function $g(r)$ was obtained by multiplying the distribution of distances with the re-weighting function and setting the different pieces of the different windows together.

Figure 7.2 shows the effective pair potential for different values of the hydrophobic length L of the proteins and different hydrophobicity parameters ϵ_{pt}. Except for a hydrophobicity parameter $\epsilon_{pt} = 1.0$, where the interaction is too weak, the curves show an oscillatory shape. The oscillations have a period of approximately $1\sigma_t$ indicating that they are caused by packing effects of the lipid chains.

In the case of $\epsilon_{pt} = 1.0$ the characteristics of the curve correspond qualitatively to the findings of Sintes and Baumgärtner [104]. The effective pair potential shows a minimum at close distances followed by a shallow maximum. Apart from the first minimum the minima become more shallow with increasing distance and/or decreasing hydrophobicity parameter ϵ_{pt}. With increasing ϵ_{pt} the layering effect becomes more pronounced. The lipids pack more tightly, if they are closer to the protein surface. This is a result of the strong Lennard-Jones potential we use as interaction potential.

The first minimum disappears for high hydrophobicity parameters and deepens with decreasing ϵ_{pt}. It is a result of different effects: First, there is the direct protein-protein interaction and the solvent-induced interaction between the hydrophilic protein section located outside of the lipid bilayer. When the proteins come into contact the volume of the two proteins get reduced resulting in an attractive force between the two proteins. The amplitude of this interaction is shown in the inset of the bottom panel of figure 7.2. Second, we have the depletion-type interaction induced by the lipids. They maximise their translational and conformational entropy by pushing the proteins together. This effect is strongest at low ϵ_{pt}, where the proteins and the lipids repel each other. The last effect is a bridging interaction induced by the lipids. At higher ϵ_{pt} the lipids gain from being in contact with the proteins. They tend to squeeze themselves between the proteins, pushing them apart, and the height of the first minimum goes up. The competition between the depletion interaction and the lipid bridging effect accounts for the preferred arrangement of the proteins in the membrane which depends on ϵ_{pt}, figure 7.1.

The hydrophobic mismatch between the proteins and the lipid bilayer has an influence on the strength of the layering and the effective contact energy between the proteins. Additionally, for a hydrophobic length $L = 4\sigma_t$ (negative hydrophobic mismatch) and $L = 8\sigma_t$ (positive hydrophobic mismatch), there is a smooth attractive interaction that superimposes the packing interaction at distances $r > 4\sigma_t$.

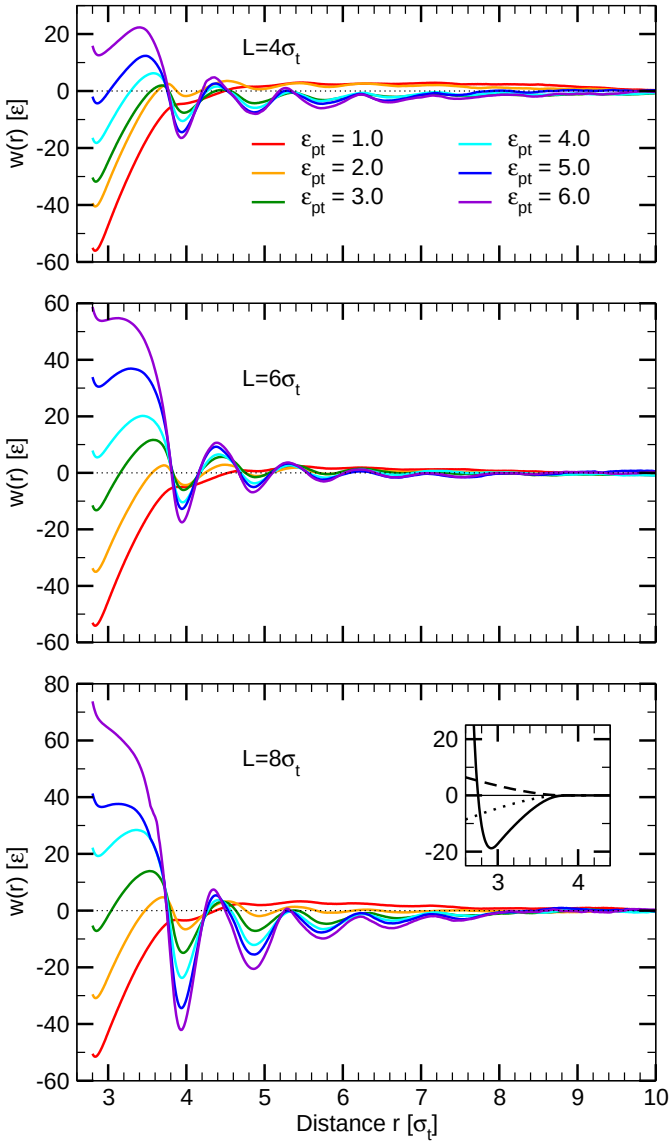

Figure 7.2: Effective pair potential $w(r)$ between two proteins with hydrophobic length $L = 4\sigma_t$ (negative hydrophobic mismatch, top panel), $L = 6\sigma_t$ (no hydrophobic mismatch, middle panel), $L = 8\sigma_t$ (positive hydrophobic mismatch, bottom panel) for different values of the hydrophobicity parameter ϵ_{pt}. The inset in the bottom panel shows the interactions generated outside of the membrane (solvent-mediated depletion interaction and direct interaction) for hydrophobically matched inclusions (solid line) and the additional contribution of solvent-induced interactions at $L = 4\sigma_t$ (dashed line) and $L = 8\sigma_t$ (dotted line).

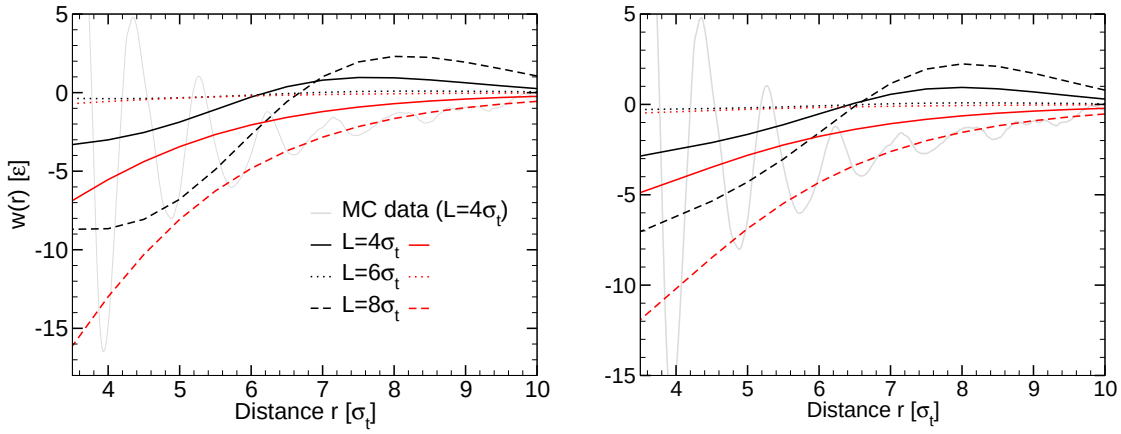

Figure 7.3: Effective interaction potential between two proteins according to the elastic theory (black lines) and the Landau-de Gennes theory (red lines) for proteins with different hydrophobic length L. The thick grey line shows the simulation data for $L = 4\sigma_t$, $\epsilon_{pt} = 6.0$ for comparison. On the left hand side we set $R_{el,LdG} = 1.5\sigma_t$ and on the right hand side we set $R_{el,LdG} = 2.0\sigma_t$.

Now we would like to compare the smooth long-range contribution to the Landau-de Gennes and the elastic theory, figure 7.3. The theoretical curves are calculated numerically by minimising the free energy, equation 2.3 or equation 2.9 with $\tilde{c}_0$ replacing c_0, for a system containing two proteins at given distance r with the boundary condition $\phi = t_R$ at the surface of the protein. The model parameters are taken from the fit of the fluctuation spectra and the fit of the thickness profiles. In the Landau-de Gennes calculation the parameter $4a$ in equation 2.3 is identified with the reduced area compressibility modulus k_A/t_0^2. The fit of the thickness spectrum did not produce dependable parameters a and c, whereas the value of k_A is compatible with independent simulation data of the lipid area increase at finite surface tension [85]. To calculate the free energy, the corresponding integrals are discretised in real space using a square lattice with spatial discretisation parameter h and a second order difference scheme to evaluate the derivatives. The boundary condition was implemented by setting $\phi = t_R$ inside the inclusion. The energy was minimised via a steepest descent method [98]. The final accuracy was $\int d^2r|\delta\mathcal{F}/\delta\phi| \leq 10^{-6}$. The curves shown in figure 7.3 were obtained using the spatial discretisation $h = 0.5\sigma_t$ and a system of size $30 \times 20\sigma_t^2$ with periodic boundary conditions, which corresponds to the situation in the Monte Carlo simulations. The Landau-de Gennes theory as well as the elastic theory predicts an attractive interaction for distances $r < 6\sigma_t$. At larger distances the Landau-de Gennes theory predicts an attractive interaction. The elastic theory shows a repulsive interaction at larger distances with a peak at about $r \sim 8\sigma_t$. The simulation data show no indication for the existence of such a positive peak. In the case of one protein included in the lipid bilayer the elastic theory gives much better results than the Landau-de Gennes theory. In the case of two proteins the predictions of the

Landau-de Gennes theory fit to our simulation data better than the predictions of the elastic theory. This should not be overestimated. The weakly oscillatory behaviour of the effective pair potential in the elastic theory is generated by soft peristaltic modes in the fluctuation spectrum, which has been shown to leave a clear signature in the shape of the distortion profiles around single proteins. The simulation data suggest that the effect of this mode on the lipid-mediated interactions between two proteins is destroyed by some yet unknown mechanism. As in the case of the analysis of the radial thickness profiles in the vicinity of one single protein, we have done the analysis for two values for the protein radius: $R_{el,LdG} = 1.5\sigma_t$, the real radius, and $R_{el,LdG} = 2.0\sigma_t$, the point where the curves start. In general the curves show the same behaviour, independently of the protein radius. The only difference is the depth of the starting point of the curves. This minimum lies deeper in the case of a radius $R_{el,LdG} = 1.5\sigma_t$.

Our finding that the lipid-mediated interaction between proteins tends to be attractive indicate that it is most favourable for the proteins to cluster. This is consistent with the findings of de Meyer et al. [19]. Their effective pair potentials are also always negative, except for proteins with very large diameters.

7.2 Bilayer Deformation

Section 6.1 dealt with the deformation profiles of a lipid bilayer in the vicinity of one single protein. In this section we want to look at the deformation profiles of a lipid bilayer with two proteins. We analyse the thickness as well as the hydrophilic shielding parameter, the (bond) chain order parameter S_z and the (chain criterion) monolayer overlap as two dimensional profiles, figures 7.4-7.10. For this purpose we have rotated the whole system so that the connecting line between the two proteins is on the x-axis. The data of the figures are obtained from the umbrella sampling simulations. The system has been divided along the x- and y-axis in bins of size $1\sigma_t^2$. Since the proteins moved slightly during the simulations, according to their umbrella window, one has to be somewhat careful with the interpretation of the data in the bins at direct contact to the proteins.

The thickness profiles of the lipid bilayer show a similar behaviour as in the case of one single protein incorporated into the lipid bilayer. Far away from the protein the thickness is significantly decreased ($5.3 - 5.5\sigma_t$) in comparison to the case of one single protein ($5.7 - 5.8\sigma_t$) in a system of comparable size. The reason for this is that the pressure difference according to the solvent excluded volume effect is raised for every protein. So in the case of two proteins there is an increase in the pressure difference and with this in the tension resulting in a further thinning of the lipid bilayer. For small distances where the two proteins touch, the thickness is distinctly decreased in the case of negative hydrophobic mismatch. The thickness increases with increasing distance to the connecting line between the proteins up to a value of about $5.4\sigma_t$ and stays more or less constant. At intermediate protein-protein distances the thickness between the two proteins is increased but still much smaller than for distances

far away from the proteins. For large protein distances the thickness between the two proteins is further increased but still does not reach the value far away from the proteins. For the case of hydrophobic matching and positive hydrophobic mismatch the thickness profiles for small protein-protein distances show the behaviour as if one single protein were incorporated into the lipid bilayer. At intermediate distances the thickness between the proteins is increased. At large protein-protein distances the thickness between the proteins is further decreased but still increased in comparison to the thickness far away from the proteins.

Figures 7.4 to 7.7 compare the thickness profiles obtained from the simulation runs to the thickness profiles calculated with the elastic theory. The parameters are the same we used for the calculation of the effective interaction potential. The protein-protein distance $3.5\sigma_t$ is the minimal protein distance we could calculate with the elastic theory. In general, there are much more fluctuations in the simulation data than in the theory data.

At a protein-protein distance of about $6.5\sigma_t$ (figure 7.5) the elastic theory predicts a minimum in the thickness between the two proteins for a hydrophobic length $L = 4\sigma_t$ and a maximum in the thickness between the two proteins for a hydrophobic length $L = 6\sigma_t$ and $L = 8\sigma_t$. We do not observe this minimum and maximum between the proteins in the simulation data. The elastic theory predicts a positive effective pair potential for protein-protein distances between $6.0 - 10.0\sigma_t$. There is a maximum in the pair potential for a protein-protein distance of $8.0\sigma_t$. Perhaps this maximum and minimum, respectively, in the thickness profiles is responsible for the maximum in the effective pair potential obtained by the elastic theory.

Figure 7.6 shows the thickness profiles for a protein-protein distance of about $8.0\sigma_t$. The maximum between the proteins in the case of hydrophobic matching and negative hydrophobic mismatch is not so obvious any more.

For a protein-protein distance of about $11.0\sigma_t$ the thickness between the two proteins is smaller in the case of the negative hydrophobic matching case, and larger in the case of hydrophobic matching and positive hydrophobic mismatch, respectively, for the data obtained from the simulations in comparison to the data obtained from the theory.

There are obvious differences between the thickness profiles obtained from the simulation data and the thickness profiles obtained from the theory. These differences could be the cause of the discrepancy between the effective pair potential obtained from simulation, and elastic theory, respectively. The lipids rearrange themselves as the proteins move closer together. Consequently, the local distortion profiles $\delta q/q_0$ in equation 2.27 change at small protein distances. This in turn affects the renormalised curvature term $\tilde{c}_0$ which then depends on the distance between the two proteins and varies spatially on the protein surface.

The hydrophilic shielding parameter is increased in the case of negative hydrophobic mismatch. The profile shows the same undershooting behaviour as in the case of one single protein. At intermediate distances the hydrophilic shielding parameter is still increased around the proteins, but the undershooting is not so pronounced

any more as in the case of small protein-protein distances. For large protein-protein distances the hydrophilic shielding parameter is decreased between the proteins but still increased in comparison to the value far away from the proteins. In the case of hydrophobic matching and positive hydrophobic mismatch the hydrophilic shielding parameter is decreased at direct contact to the proteins for all protein-protein distances. With increasing protein-protein distance the hydrophilic shielding parameter increases between the two proteins.

The bond chain order parameter S_z is increased for all distances at direct contact to the proteins independent of the hydrophobic length of the proteins. The value for the chain order parameter is higher, about 0.8, for the case of hydrophobic mismatch. At intermediate protein-protein distances the chain order parameter between the two proteins is slightly increased. For large protein-protein distances the chain order parameter measured between the proteins is only increased slightly compared to the chain order parameter measured at any other place far away from the proteins.

The last quantity we want to look at is the chain criterion monolayer overlap. Around the proteins the two monolayers overlap in the case of negative hydrophobic mismatch. With increasing distance to the proteins the two monolayers become very well separated. At intermediate protein-protein distances the two monolayers overlap between the two proteins. This overlap further decreases with increasing protein-protein distance and is about zero for large protein-protein distances. For hydrophobically matching proteins the overlap of the two monolayers is nearly constant over the whole range of distances to the proteins and distances between the two proteins. The two monolayers are very well separated. For positive hydrophobic mismatch the two monolayers are again very well separated, but the separation between the two monolayers increases for some distance to the proteins and then decreases again.

In summary we can say that these profiles show pretty much the same behaviour as the profiles obtained in the vicinity of one single protein.

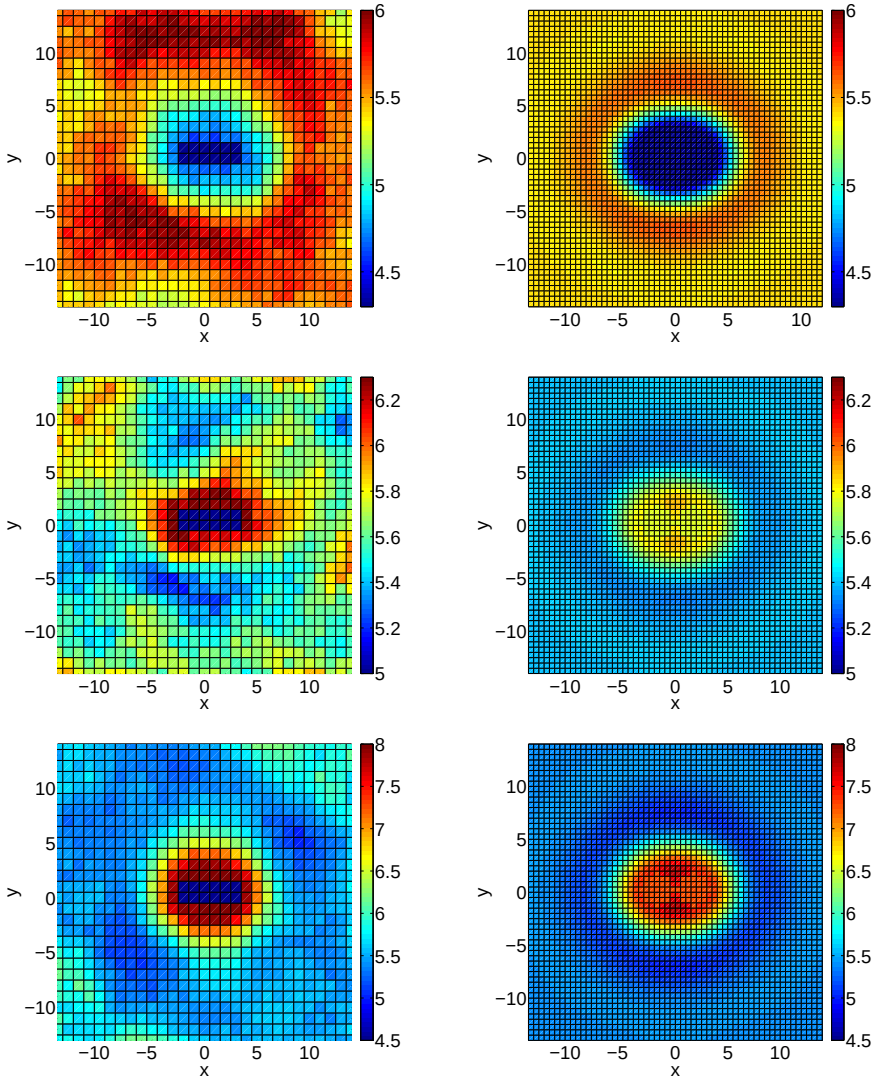

(a) $2.9\sigma_t - 3.05\sigma_t$ (b) $3.5\sigma_t$

Figure 7.4: Comparison of the two-dimensional thickness profiles in the vicinity of two proteins of hydrophobic length $L = 4\sigma_t$ (upper panels), $L = 6\sigma_t$ (middle panels) and $L = 8\sigma_t$ (lower panels). The left hand side (a) is obtained from umbrella sampling simulations (protein-protein distance $2.9\sigma_t - 3.05\sigma_t$). The right hand side is obtained from the elastic theory (protein-protein distance $3.5\sigma_t$).

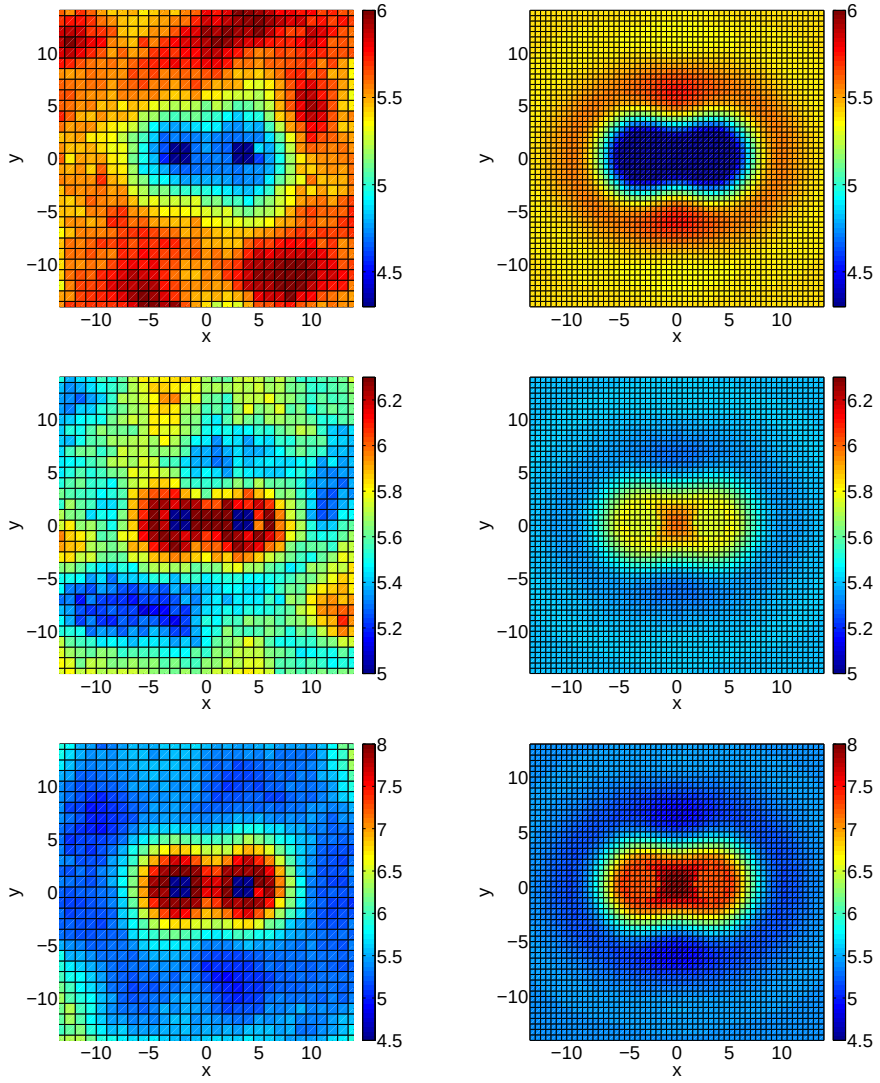

(a) $6.3\sigma_t - 6.8\sigma_t$ (b) $6.5\sigma_t$

Figure 7.5: Comparison of the two-dimensional thickness profiles in the vicinity of two proteins of hydrophobic length $L = 4\sigma_t$ (upper panels), $L = 6\sigma_t$ (middle panels) and $L = 8\sigma_t$ (lower panels). The left hand side (a) is obtained from umbrella sampling simulations (protein-protein distance $6.3\sigma_t - 6.8\sigma_t$). The right hand side is obtained from the elastic theory (protein-protein distance $6.5\sigma_t$).

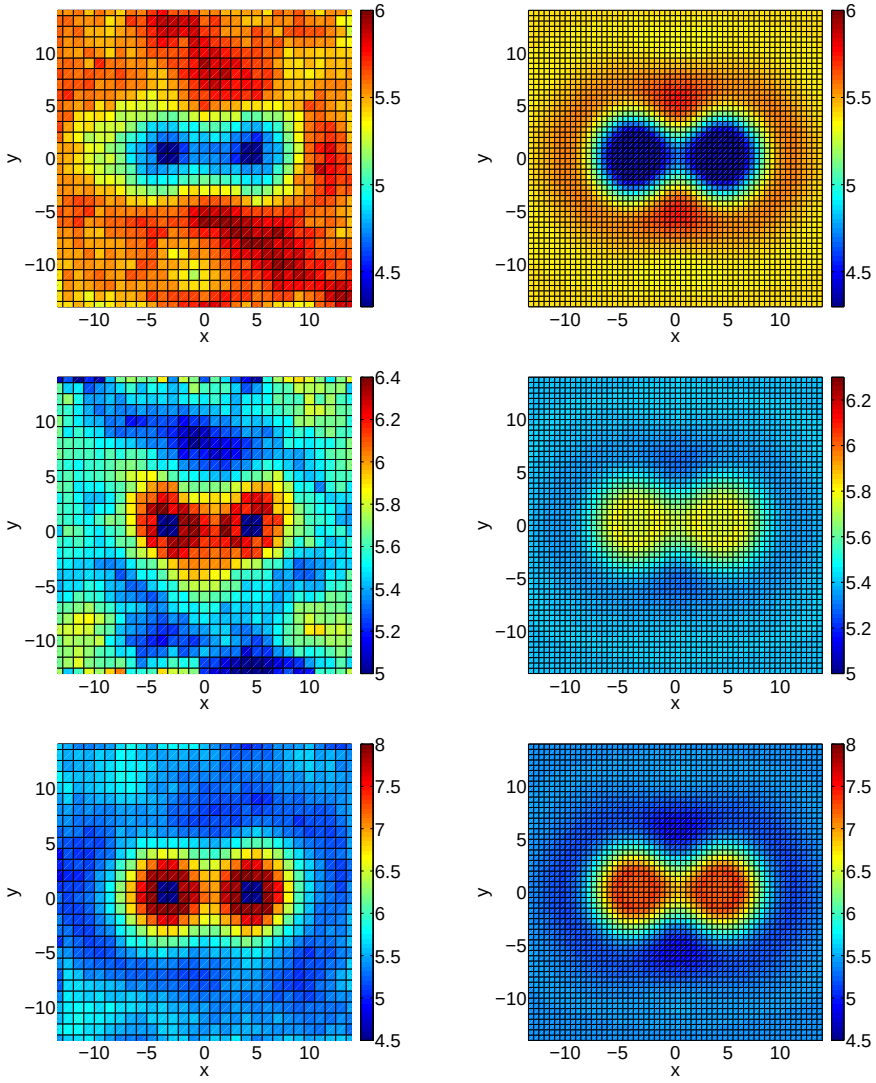

(a) $7.5\sigma_t - 8.5\sigma_t$ (b) $8.0\sigma_t$

Figure 7.6: Comparison of the two-dimensional thickness profiles in the vicinity of two proteins of hydrophobic length $L = 4\sigma_t$ (upper panels), $L = 6\sigma_t$ (middle panels) and $L = 8\sigma_t$ (lower panels). The left hand side (a) is obtained from umbrella sampling simulations (protein-protein distance $7.5\sigma_t - 8.5\sigma_t$). The right hand side is obtained from the elastic theory (protein-protein distance $8.0\sigma_t$).

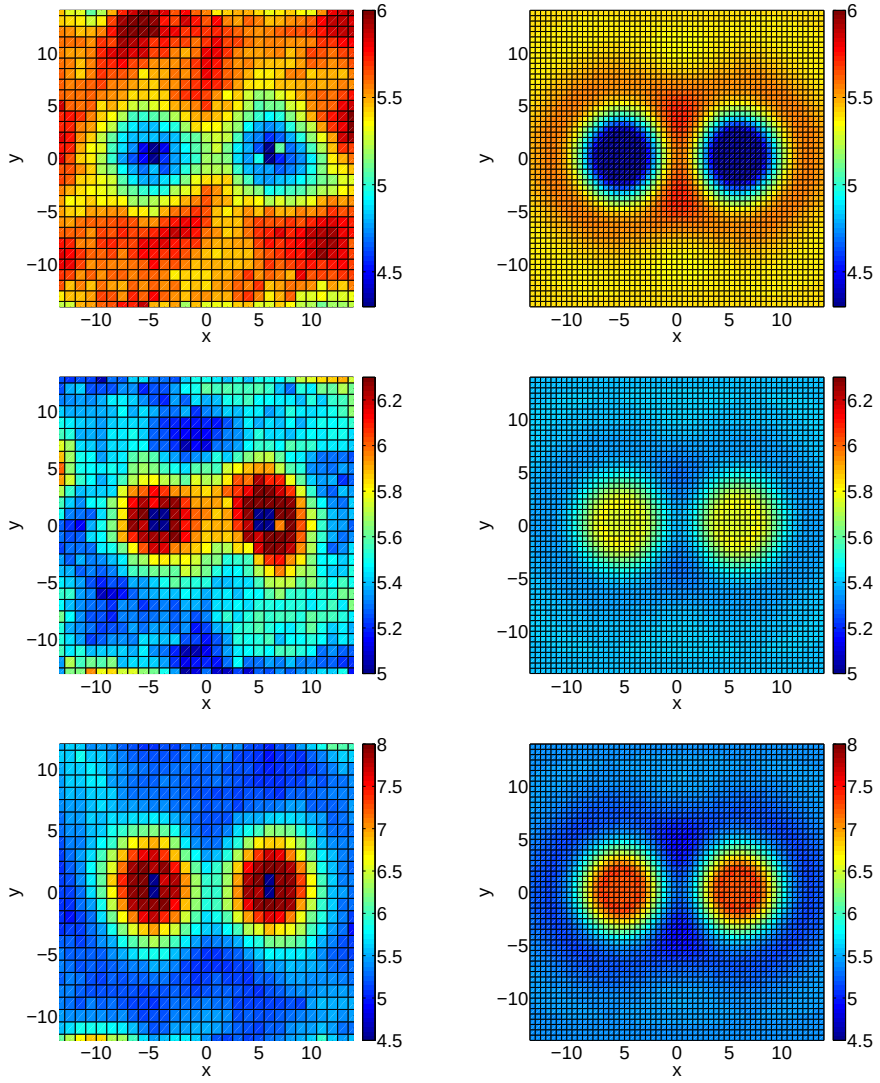

(a) $10.0\sigma_t - 12.0\sigma_t$ (b) $11.0\sigma_t$

Figure 7.7: Comparison of the two-dimensional thickness profiles in the vicinity of two proteins of hydrophobic length $L = 4\sigma_t$ (upper panels), $L = 6\sigma_t$ (middle panels) and $L = 8\sigma_t$ (lower panels). The left hand side (a) is obtained from umbrella sampling simulations (protein-protein distance $10.0\sigma_t - 12.0\sigma_t$). The right hand side is obtained from the elastic theory (protein-protein distance $11.0\sigma_t$).

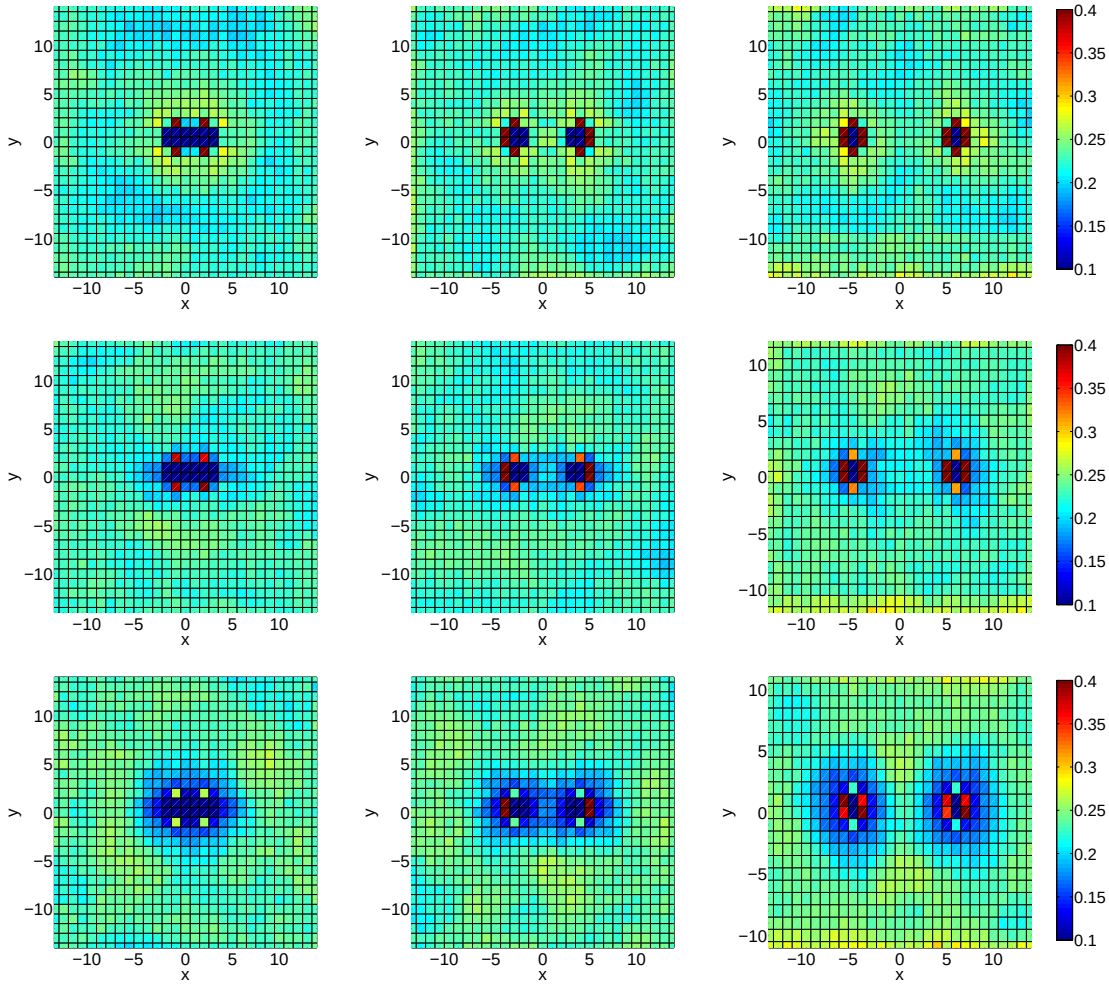

(a) $2.9\sigma_t - 3.05\sigma_t$ (b) $6.3\sigma_t - 6.8\sigma_t$ (c) $10.0\sigma_t - 12.0\sigma_t$

Figure 7.8: Two-dimensional profile of the hydrophilic shielding parameter in the vicinity of two proteins of hydrophobic length $L = 4\sigma_t$ (upper panels), $L = 6\sigma_t$ (middle panels) and $L = 8\sigma_t$ (lower panels) and a hydrophobicity parameter $\epsilon_{pt} = 6.0$ for three different protein-protein distances: (a) $2.9\sigma_t - 3.05\sigma_t$, (b) $6.3\sigma_t - 6.8\sigma_t$, (c) $10.0\sigma_t - 12.0\sigma_t$

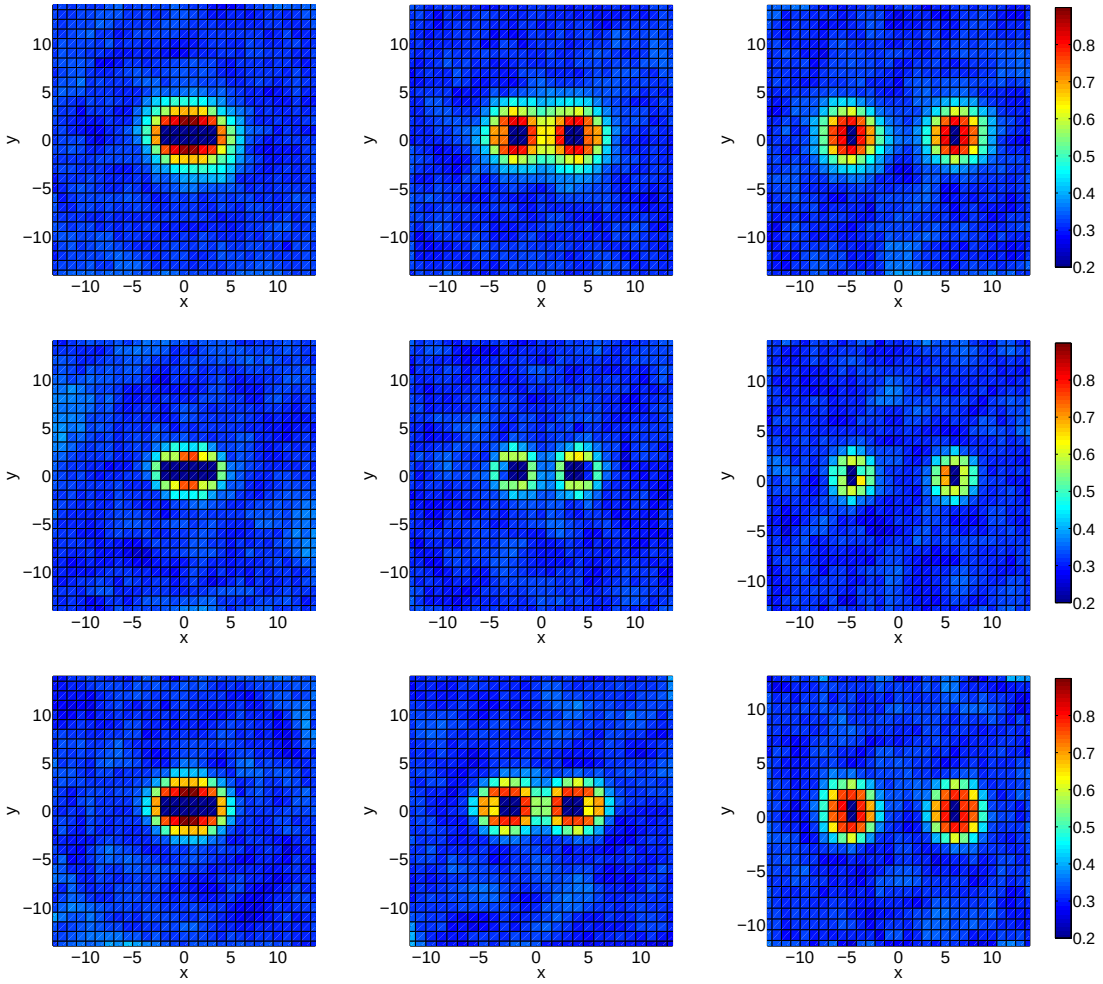

(a) $2.9\sigma_t - 3.05\sigma_t$ (b) $6.3\sigma_t - 6.8\sigma_t$ (c) $10.0\sigma_t - 12.0\sigma_t$

Figure 7.9: Two-dimensional profile of the chain order parameter S_z in the vicinity of two proteins of hydrophobic length $L = 4\sigma_t$ (upper panels), $L = 6\sigma_t$ (middle panels) and $L = 8\sigma_t$ (lower panels) and a hydrophobicity parameter $\epsilon_{pt} = 6.0$ for three different protein-protein distances: (a) $2.9\sigma_t - 3.05\sigma_t$, (b) $6.3\sigma_t - 6.8\sigma_t$, (c) $10.0\sigma_t - 12.0\sigma_t$

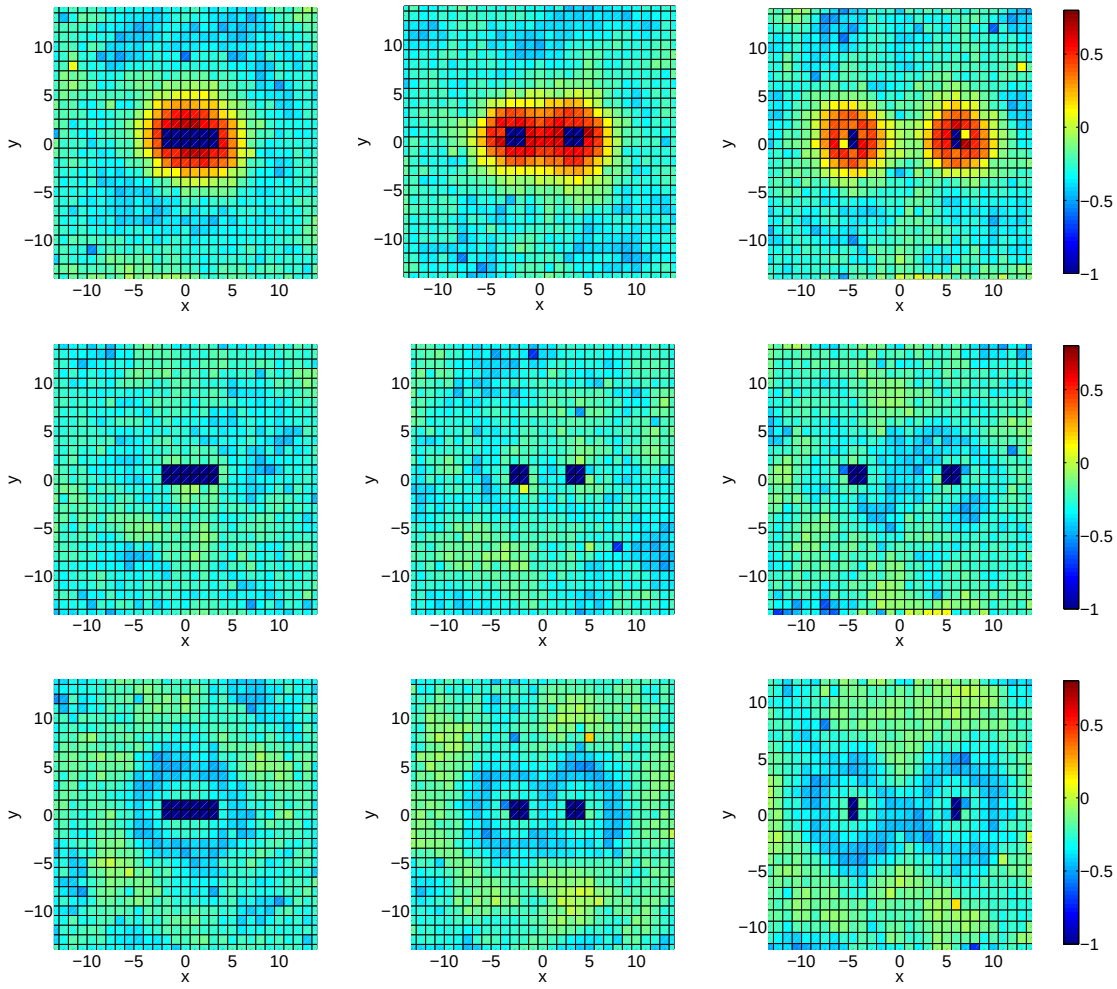

(a) $2.9\sigma_t - 3.05\sigma_t$ (b) $6.3\sigma_t - 6.8\sigma_t$ (c) $10.0\sigma_t - 12.0\sigma_t$

Figure 7.10: Two-dimensional profile of the (chain criterion) monolayer overlap in the vicinity of two proteins of hydrophobic length $L = 4\sigma_t$ (upper panels), $L = 6\sigma_t$ (middle panels) and $L = 8\sigma_t$ (lower panels) and a hydrophobicity parameter $\epsilon_{pt} = 6.0$ for three different protein-protein distances: (a) $2.9\sigma_t - 3.05\sigma_t$, (b) $6.3\sigma_t - 6.8\sigma_t$, (c) $10.0\sigma_t - 12.0\sigma_t$

7.3 Comparison between Different Protein Diameters

In section 6.3 we analysed the influence of the protein diameter on the interaction between one single protein and the lipids. In this section we investigate the influence of the protein diameter on the effective pair potential between two proteins. We repeated the umbrella sampling simulations described in the first section for two proteins of diameter $\sigma_p = 1\sigma_t$. Figure 7.11 shows the effective pair potential between two proteins of hydrophobic length $L = 6\sigma_t$ and hydrophobicity parameter $\epsilon_{pt} = 1.0$ and 6.0, respectively.

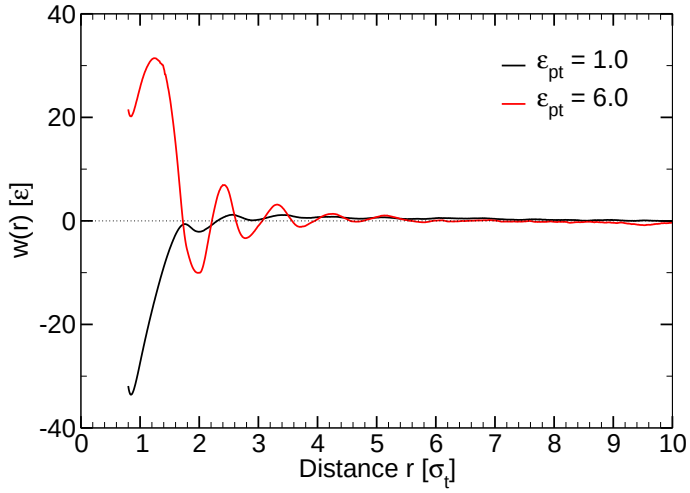

Figure 7.11: Effective pair potential $w(r)$ between two thin proteins with hydrophobic length $L = 6\sigma_t$ for two different values of the hydrophobicity parameter ϵ_{pt}

In the case of $\epsilon_{pt} = 6.0$ the curve shows the oscillatory behaviour as well as the same number of maxima and minima as in the case of the protein of diameter $\sigma_p = 3\sigma_t$. The height and depth of the minima and maxima of both curves are a little reduced in comparison to the corresponding curves obtained for a protein of diameter $\sigma_p = 3\sigma_t$. Especially the first minima and maxima, respectively, show a different behaviour. One reason for the discrepancy in the first maxima is the interaction induced by the solvent. But nevertheless there is no big difference between the curves for the different protein diameters. Figure 7.12 shows the predictions of the elastic theory and the Landau-de Gennes theory for a protein radius $R_{el,LdG} = 0.5\sigma_t$ and $R_{el,LdG} = 1.0\sigma_t$. Since we only have data for the hydrophobic length $L = 6\sigma_t$, which is the most uninteresting case regarding the two theories, we cannot say much about the comparison between theory and simulation data.

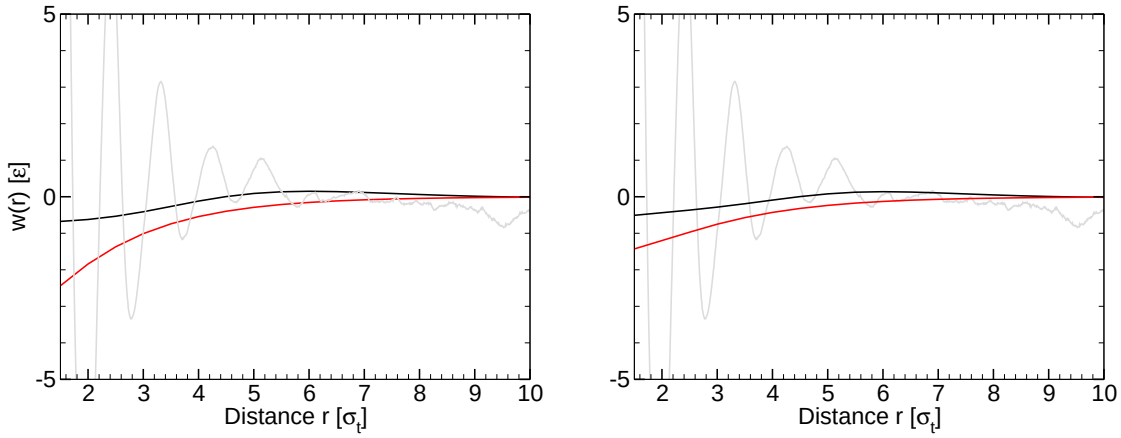

Figure 7.12: Effective interaction potential between two proteins according to the elastic theory (black line) and the Landau-de Gennes theory (red line) for thin proteins with hydrophobic length $L = 6\sigma_t$. The thick grey line shows the simulation data for comparison. On the left hand side we set $R_{el,LdG} = 0.5\sigma_t$ and on the right hand side we set $R_{el,LdG} = 1.0\sigma_t$.

7.4 Protein with Tilt

In the analysis done so far the length of the two proteins is equal to the length of the simulation box in z-direction. The analysis of the simulations with one protein incorporated into the lipid bilayer showed that in the case of the large system there is only little difference between the results obtained for a protein with length equal to the simulation box and a sphero-cylinder protein. There is a little difference in the thickness profiles due to the tension induced by the solvent beads. The measurement of the effective pair potential is done in a small system. In this case the system is too small to balance the tension very well. The thickness is very clearly reduced. To ensure that the induced tension does not have any influence on the effective pair potential between two proteins, we repeated the umbrella sampling simulations for two sphero-cylinder proteins of diameter $\sigma_p = 3\sigma_t$. For simplification we used the re-weighting function obtained in section 7.1. We focus only on the data for the hydrophobicity parameter $\epsilon_{pt} = 4.0$ and $\epsilon_{pt} = 6.0$, respectively, for the three different values of the hydrophobic length. To make the results comparable we measured the distance between the two proteins in the xy-plane. The simulations were done on the one hand for two sphero-cylinder proteins, which were not allowed to tilt and on the other hand for two sphero-cylinder proteins, which were allowed to tilt.

Figure 7.13 shows the effective pair potential for two sphero-cylinder proteins, which are allowed to tilt. For a better comparison we included the curves obtained for two proteins with a length equal to the simulation box in z-direction. The possible tilt has no influence on the global characteristics of the curves. The only difference between the curves for the sphero-cylinder proteins compared to the long proteins is

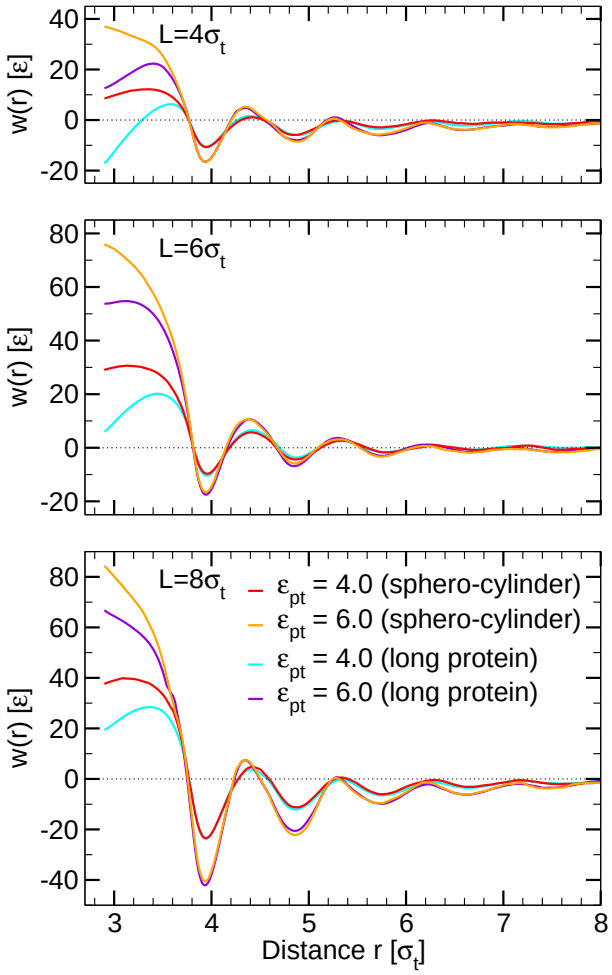

Figure 7.13: Comparison of the effective pair potential $w(r)$ between two sphero-cylinder proteins, which are allowed to tilt (red and orange curve) and two proteins with a length equal to the simulation box in z-direction (cyan and violet curve). The hydrophobic length of the proteins is $L = 4\sigma_t$ (top panel), $L = 6\sigma_t$ (middle panel), and $L = 8\sigma_t$ (bottom panel). The hydrophobicity parameter is $\epsilon_{pt} = 4.0$, and $\epsilon_{pt} = 6.0$ respectively.

observed for distances up to $4\sigma_t$. In the direct contact region the potential is increased in comparison to the long proteins. The reason for this is the depletion-induced interaction with the solvent.

7.5 Conclusions

With umbrella sampling methods we obtained the effective pair potential between two proteins. The tension induced by the solvent has no influence on the effective pair potential. This was ensured by repeating the umbrella sampling simulations with two sphero-cylinder proteins.

8 Conclusions and Outlook

We have presented a generic coarse-grained model to investigate lipid-protein interactions. The analysis of a pure lipid bilayer gave us the possibility to extract some basic characteristics of the lipid bilayer, for example the spontaneous curvature and the Gaussian rigidity. We showed that the elastic theory provides an excellent description of the peristaltic and bending fluctuations. Furthermore from the fluctuation spectra we could extract the elastic constants.

The deformation of the lipid bilayer induced by an inserted protein follows a non-monotonic behaviour. We were able to calculate the characteristics of the curve with an extended version of the elastic theory – we have introduced a renormalised curvature. The renormalised curvature is clearly influenced by certain (unknown) factors.

An artefact of our protein model is that the solvent introduces an internal tension resulting in a thinning of the lipid bilayer. We have analysed this thinning and were able to satisfactorily explain the reason for this behaviour. With an extension of the protein model, a model where the protein is allowed to tilt, we could show that the restriction of the alignment of the protein along the bilayer normal has no influence on the results. One reason is that due to the quite strong lipid-protein interaction the protein only tilts slightly.

With umbrella sampling methods we measured the effective pair potential between two proteins. The elastic theory as well as the Landau-de Gennes theory are not able to reproduce our findings. The curves exhibit an oscillating behaviour due to the hard Lennard-Jones potential we use for the bead-protein interaction. The induced tension does not have any influence on the curves.

Apart from the analysis of the tension profile as well as the fluctuation spectra of a pure lipid bilayer we have done all studies in the fluid phase. In the gel phase the protein-protein interactions would be rather different. In this case one should do a two-dimensional analysis. In the gel-phase the lipid chains are tilted towards the bilayer normal. An adequate study includes not only the analysis with respect to the protein-protein distances but also the analysis with respect to the tilt angle of the lipids and the angle of the connecting line of the two proteins.

Appendix A

System Size Dependence of the Tension Profile

Due to the height fluctuations the tension profile depends on the system size. With increasing system size the tensor profile is broadened. We assume that the tension profile $\gamma(z)$ bases on a size independent intrinsic surface tension profile $\gamma_{int}(z)$:

$$\gamma(z) = \int H\left(z - z'\right) \gamma_{int}\left(z'\right) dz' \quad . \tag{A.1}$$

H is the distribution of interface heights and depends on the system size. It obeys the following equations:

$$\int H\left(z\right) dz = 1 \qquad \text{and} \qquad \int H\left(z\right) z dz = 0 \quad . \tag{A.2}$$

In the following we analyse the system size dependence of the different moments of the tension profile, equation A.1.

$$\begin{aligned}
\Gamma_0 = \int \gamma(z) dz &= \int dz \int dz' H\left(z - z'\right) \gamma_{int}\left(z'\right) \\
&= \int \gamma_{int}\left(z'\right) dz' \underbrace{\int H\left(z - z'\right) dz}_{1} \\
&= \int \gamma_{int}\left(z'\right) dz' = \Gamma \quad .
\end{aligned}$$

Since the overall tension Γ of the system is zero, the zeroth moment vanishes independently of the system size.

$$\begin{aligned}
\Gamma_2 = \int \gamma(z) z^2 dz &= \int dz \int dz' H\left(z - z'\right) \gamma_{int}\left(z'\right) z^2 \\
&\overset{u=z-z'}{=} \int du \int dz' H(u) \gamma_{int}\left(z'\right) \left(u + z'\right)^2
\end{aligned}$$

$$
\begin{aligned}
&= \underbrace{\int dz' \gamma_{int}(z')}_{\Gamma=0} \int du H(u) u^2 + 2 \int dz' \gamma_{int}(z') z' \underbrace{\int du H(u) u}_{0} \\
&+ \int dz' \gamma_{int}(z') z'^2 \underbrace{\int du H(u)}_{1} \\
&= \int \gamma_{int}(z') z'^2 dz' \quad .
\end{aligned}
$$

The second moment is also independent of the system size. In contrast the first moment of the tension profile depends on the system size:

$$
\begin{aligned}
\Gamma_1 = \int \gamma(z)|z| dz &= \int dz \int dz' H(z - z') \gamma_{int}(z') |z| \\
&\overset{u=z-z'}{=} \int dz' \int_{-\infty}^{\infty} du \gamma_{int}(z') H(u)|u + z'| \\
&\overset{u+z'<0}{=} -2 \int dz' \gamma_{int}(z') \int_{-\infty}^{-z'} du H(u) (u + z') \\
&= -2 \int dz' \gamma_{int}(z') z' \int_{-\infty}^{-z'} du H(u) \\
&\quad - 2 \int dz' \gamma_{int}(z') \int_{-\infty}^{-z'} du H(u) u \quad .
\end{aligned}
$$

We make the following ansatz $H(u) = N_L \exp\left(-u^2/2w_L^2\right)$ and get for the two different parts of the last equation:

$$
\begin{aligned}
\int_{-\infty}^{-z} du H(u) u = \int_{z}^{\infty} du H(u) u &= N_L \int_{z}^{\infty} du u \exp\left(-u^2/2w_L^2\right) \\
&= N_L w_L^2 \exp\left(-z^2/2w_L^2\right) = w_L^2 H(z) \\
\int_{-\infty}^{-z} du H(u) = \int_{z}^{\infty} du H(u) &= \int_{z}^{\infty} N_L \exp\left(-u^2/2w_L^2\right) du \\
&= \frac{\sqrt{\pi}}{2} \left(1 - \mathrm{Erf}\left(z/\sqrt{2}w_L\right)\right) \quad .
\end{aligned}
$$

$\mathrm{Erf}(z) = 1 - 2/\sqrt{\pi} \int_z^{\infty} \exp\left(-u^2\right) du$ is the error function. In summary we get for the first moment:

$$
\Gamma_1 = \int |z| \gamma(z) \, dz = 2 \int dz' \gamma_{int}(z') \left(z' \frac{\sqrt{\pi}}{2} \left(\mathrm{Erf}\left(\frac{z}{\sqrt{2}w_L} \right) - 1 \right) - w_L^2 H(z') \right) \quad .
$$

Since H as well as w_L are system size dependent, the first moment depends also on the system size.

Appendix B

Calculation of the Free Energy in the Elastic Theory

We consider a scalar quantity $q(r)$, which is distorted from its bulk value q_0 by the inclusion. This quantity alters the membrane properties, therefore the free energy, equation 2.9, is extended by two new terms:

$$\mathcal{F}_q = \int_R^L d^2r \left\{ K_1 \frac{\delta q(r)}{q_0} \phi + K_2 \frac{\delta q(r)}{q_0} \nabla_r^2 \phi \right\} \quad . \tag{B.1}$$

$\delta q/q_0$ denotes the relative deviation of q. Terms that do not depend on ϕ or that are of higher than quadratic order in the deviations ϕ and $\delta q/q_0$ have been disregarded. We assume that δq decays to zero on a length scale, which is much smaller than the characteristic length scales of the elastic profile. For an inclusion centred at $r = 0$ we can set $\phi = t_R + t'_R(r - R)$. For the first term we get

$$\begin{aligned} 2\pi \int_R^L r dr K_1 \frac{\delta q(r)}{q_0} \phi &= 2\pi \int_R^L r dr K_1 \left(t_R + t'_R (r - R) \right) \frac{\delta q(r)}{q_0} \\ &= 2\pi t_R \int_R^L r dr K_1 \frac{\delta q(r)}{q_0} + 2\pi t'_R \int_R^L r (r - R)\, dr K_1 \frac{\delta q(r)}{q_0} \quad , \end{aligned} \tag{B.2}$$

while the second term yields

$$\begin{aligned} 2\pi \int_R^L r dr K_2 \frac{\delta q(r)}{q_0} ((1/r)\partial_r r \partial_r \phi) &= 2\pi \int_R^L dr K_2 \frac{\delta q(r)}{q_0} (\partial_r r \partial_r \phi) \\ &= 2\pi K_2 \frac{\delta q(r)}{q_0} (r \partial_r \phi) \Big|_R^L - 2\pi \int_R^L dr K_2 \left(\partial_r \frac{\delta q(r)}{q_0} \right) (r \partial_r \phi) \\ &= 2\pi K_2 \frac{\delta q(r)}{q_0} (r \partial_r \phi) \Big|_R^L - 2\pi K_2 \frac{\delta q(r)}{q_0} (r \partial_r \phi) \Big|_R^L \\ &\quad + 2\pi \int_R^L dr K_2 \frac{\delta q(r)}{q_0} (\partial_r \phi) \\ &= 2\pi t'_R \int_R^L dr K_2 \frac{\delta q(r)}{q_0} \quad . \end{aligned} \tag{B.3}$$

Inserting equation B.2 and B.3 into equation B.1 gives

$$\mathcal{F}_q = 2\pi t_R \int_R^L r dr K_1 \frac{\delta q(r)}{q_0} + 2\pi t'_R \int_R^L dr \frac{\delta q(r)}{q_0} (K_2 + K_1 r (r - R)) \quad . \tag{B.4}$$

The total free energy $\mathcal{F}_{el}$, equation 2.26, now has the form

$$\begin{aligned}\mathcal{F}_{el} = 2\pi\int_R^L rdr\left(\frac{k_A}{2t_0^2}\phi^2 + 2k_c c_0\nabla_r^2\phi + 2k_c\frac{\zeta}{t_0}\phi\nabla_r^2\phi + \frac{k_c}{2}\left(\nabla_r^2\phi\right)^2 + k_G\frac{(\partial_r\phi)(\partial_{rr}\phi)}{r}\right)\\ + 2\pi t_R\int_R^L rdrK_1\frac{\delta q(r)}{q_0} + 2\pi t'_R\int_R^L dr\frac{\delta q(r)}{q_0}(K_2 + K_1 r(r-R))\end{aligned} \tag{B.5}$$

with $\partial_{rr} = \partial^2/\partial r^2$. We vary $\mathcal{F}_{el}$ with respect to ϕ and t'_R while keeping t_R fixed:

$$\begin{aligned}\delta\mathcal{F}_{el} = 2\pi\int_R^L rdr\Bigg(\frac{k_A}{t_0^2}\phi\delta\phi + 2k_c c_0\nabla_r^2\delta\phi + 2k_c\frac{\zeta}{t_0}\left(\phi\nabla_r^2\delta\phi + \delta\phi\nabla_r^2\phi\right)\\ + k_c\nabla_r^2\phi\nabla_r^2\delta\phi + k_G\frac{(\partial_r\delta\phi)(\partial_{rr}\phi) + (\partial_r\phi)(\partial_{rr}\delta\phi)}{r}\Bigg)\\ + 2\pi\delta t_R\int_R^L rdrK_1\frac{\delta q(r)}{q_0} + 2\pi\delta t'_R\int_R^L dr\frac{\delta q(r)}{q_0}(K_2 + K_1 r(r-R)) \quad .\end{aligned}$$

Partial integration:

$$\begin{aligned}&= 2\pi\int_R^L rdr\left(\frac{k_A}{t_0^2}\phi + 4k_c\frac{\zeta}{t_0}\nabla_r^2\phi + k_c\nabla_r^4\phi\right)\delta\phi\\ &+ 2\pi\Bigg(2k_c c_0 r(\partial_r\delta\phi)\Big|_R^L + 2k_c\frac{\zeta}{t_0}r\phi(\partial_r\delta\phi)\Big|_R^L + k_c r(\partial_r\delta\phi)\nabla_r^2\phi\Big|_R^L\\ &- k_c r\delta\phi\nabla_r^3\phi\Big|_R^L + k_G(\partial_r\delta\phi)(\partial_r\phi)\Big|_R^L - 2k_c\frac{\zeta}{t_0}r(\partial_r\phi)\delta\phi\Big|_R^L\Bigg)\\ &+ 2\pi\delta t_R\int_R^L rdrK_1\frac{\delta q(r)}{q_0} + 2\pi\delta t'_R\int_R^L dr\frac{\delta q(r)}{q_0}(K_2 + K_1 r(r-R))\\ &= 2\pi\int_R^L rdr\left(\frac{k_A}{t_0^2}\phi + 4k_c\frac{\zeta}{t_0}\nabla_r^2\phi + k_c\nabla_r^4\phi\right)\delta\phi \qquad \text{(B.6)}\\ &+ 2\pi\delta t'_R\Bigg(-2k_c c_0 R - 2k_c\frac{\zeta}{t_0}Rt_R - k_c R\nabla_r^2\phi\Big|_R - k_G t'_R\\ &\qquad + \int_R^L dr\frac{\delta q(r)}{q_0}(K_2 + K_1 r(r-R))\Bigg) \qquad \text{(B.7)}\\ &+ 2\pi\delta t_R\left(2k_c\frac{\zeta}{t_0}Rt'_R + k_c R\nabla_r^3\phi\Big|_R + \int_R^L rdrK_1\frac{\delta q(r)}{q_0}\right) \qquad \text{(B.8)}\\ &= 0 \quad .\end{aligned}$$

t_R is kept fixed, and therefore the variation δt_R is zero. Since $\delta\phi$ and $\delta t'_R = \partial_r\delta\phi|_R$ are different from zero the braces B.6 and B.7 must be zero giving the Euler-Lagrange equation

$$\nabla_r^4\phi + \frac{k_A}{k_c t_0^2}\phi + 4\frac{\zeta}{t_0}\nabla_r^2\phi = 0 \tag{B.9}$$

and the boundary condition

$$\begin{aligned}\nabla_r^2\phi\Big|_R + \frac{k_G}{k_c R}t'_R &= -\left(2c_0 + 2\frac{\zeta}{t_0}t_R - \frac{1}{k_c R}\int_R^L dr\frac{\delta q(r)}{q_0}(K_2 + K_1 r(r-R)\right)\\ &= -\left(2\tilde{c}_0 + 2\frac{\zeta}{t_0}t_R\right)\end{aligned} \tag{B.10}$$

with

$$\tilde{c}_0 = c_0 - \frac{1}{2k_c R}\int_R^L dr\frac{\delta q(r)}{q_0}(K_2 + K_1 r(r-R)) \quad . \tag{B.11}$$

Inserting equation 2.15 into equation 2.26 and doing the partial integration we get

$$\begin{aligned}\mathcal{F}_{el} &= 2\pi\int r dr\left(\frac{k_A}{2t_0}\phi^2 + 2k_c c_0\nabla_r^2\phi + 2k_c\frac{\zeta}{t_0}\phi\nabla_r^2\phi + \frac{k_c}{2}(\nabla_r^2\phi)^2\right.\\ &\qquad\left. + k_G\frac{(\partial_r\phi)(\partial_{rr}\phi)}{r}\right)\\ &\quad + 2\pi t_R\int r dr K_1\frac{\delta q(r)}{q_0} + 2\pi t'_R\int dr\frac{\delta q(r)}{q_0}(K_2 + K_1 r(r-R))\\ &= 2\pi\int r dr\underbrace{\left(\frac{k_A}{2t_0^2}\phi + 2k_c\frac{\zeta}{t_0}\phi\nabla_r^2\phi + \frac{k_c}{2}\nabla_r^4\phi\right)}_{=0\quad\text{Euler-Lagrange-Equation}}\phi\\ &\quad + 2\pi\left(\frac{k_c}{2}r\partial_r\phi\nabla_r^2\phi\Big|_R^L - \frac{k_c}{2}r\phi\nabla_r^3\phi\Big|_R^L + 2k_c c_0 r\partial_r\phi\Big|_R^L + k_G(\partial_r\phi)(\partial_r\phi)\Big|_R^L\right)\\ &\quad + 2\pi t_R\int r dr K_1\frac{\delta q(r)}{q_0} + 2\pi t'_R\int dr\frac{\delta q(r)}{q_0}(K_2 + K_1 r(r-R))\\ &= \pi\left(-k_c R t'_R\nabla_r^2\phi\Big|_R + k_c R t_R\nabla_r^3\phi\Big|_R - 4k_c c_0 R t'_R - k_G t'_R t'_R\right)\\ &\quad + 2\pi t_R\int r dr K_1\frac{\delta q(r)}{q_0} + 2\pi t'_R\int dr\frac{\delta q(r)}{q_0}(K_2 + K_1 r(r-R))\end{aligned} \tag{B.12}$$

$$= \pi k_c R\left(t_R\nabla_r^3\phi\Big|_R - 2t'_R\left(\tilde{c}_0 - \frac{\zeta}{t_0}t_R\right)\right) + \text{const.} \tag{B.13}$$

for the free energy of the deformation. To achieve the last line we inserted the boundary condition B.10 and replaced c_0 with $\tilde{c}_0$, equation B.11.

Appendix C

Collection of System Characteristics

In this appendix we collect the system characteristics of different simulation runs for systems of different size containing one protein with a length equal to the simulation box in z-direction: area $A = L_x \cdot L_y$, volume $V = L_x \cdot L_y \cdot L_z$, z-length of the simulation box L_z. Furthermore we have measured the tension inside the system in a small rectangular slice far away from the protein as well as in cylinders around the protein.

C.1 Protein of Diameter $\sigma_p = 3\sigma_t$

We investigated three different system sizes: a small system with 776 lipids and 6153 solvent beads, table C.1, a middle-size system with 1776 lipids and 13846 solvent beads, table C.2, and a large system with 3176 lipids and 24614 solvent beads, table C.3. The large system is about a factor of 4 larger than the small system.

The variables area, volume and L_z are constant in the range of the uncertainty for the different values of the protein length L and hydrophobicity parameter ϵ_{pt}. The value for the z-length shows a strong dependence of the system size indicating a large tension difference between the three different system sizes.

C.2 Protein of Diameter $\sigma_p = 1\sigma_t$

For a protein of diameter $\sigma_p = 1\sigma_t$ we did the analysis in systems of two different sizes, tables C.4 and C.5. We focused our attention only on the hydrophobicity parameters $\epsilon_{pt} = 1.0$ and $\epsilon_{pt} = 6.0$. Between the two systems the difference in L_z is not as pronounced as in the case of the thick protein. The bilayer thickness only shows little difference depending on the system size, figure D.1.

The values for the volume of the system are comparable to the corresponding values of the volume of a system with one thick protein. In the large system the effect of the solvent-induced tension is not so pronounced, therefore the values of the area and L_z also show only little difference. For a small system the solvent-induced tension has a strong effect on the system with one thick protein. The difference between the area and L_z is very clear.

$L\ [\sigma_t]$	ϵ_{pt}	$A\ [\sigma_t^2]$	$V\ [\sigma_t^3]$	$L_z\ [\sigma_t]$	$\Gamma_{slice}\ [\epsilon/\sigma_t^2]$	$\Gamma_{cylinder}\ [\epsilon/\sigma_t^2]$
4	1.0	576 ± 3	8611 ± 5	14.9 ± 0.1	0.6 ± 0.2	0.6 ± 0.1
4	2.0	581 ± 4	8609 ± 3	14.8 ± 0.1	0.7 ± 0.2	0.6 ± 0.1
4	3.0	582 ± 2	8608 ± 6	14.8 ± 0.1	0.6 ± 0.1	0.6 ± 0.1
4	4.0	581 ± 3	8602 ± 4	14.8 ± 0.1	0.6 ± 0.2	0.6 ± 0.1
4	5.0	581 ± 2	8600 ± 4	14.8 ± 0.1	0.6 ± 0.2	0.6 ± 0.1
4	6.0	585 ± 3	8603 ± 6	14.7 ± 0.1	0.8 ± 0.2	0.7 ± 0.1
6	1.0	578 ± 3	8608 ± 5	14.9 ± 0.1	0.6 ± 0.2	0.6 ± 0.1
6	2.0	578 ± 2	8604 ± 5	14.9 ± 0.1	0.6 ± 0.3	0.6 ± 0.1
6	3.0	578 ± 2	8598 ± 3	14.9 ± 0.1	0.6 ± 0.2	0.6 ± 0.1
6	4.0	579 ± 1	8595 ± 4	14.8 ± 0.1	0.6 ± 0.2	0.6 ± 0.1
6	5.0	578 ± 1	8596 ± 4	14.9 ± 0.1	0.6 ± 0.2	0.7 ± 0.1
6	6.0	577 ± 2	8587 ± 3	14.9 ± 0.1	0.7 ± 0.2	0.7 ± 0.1
8	1.0	578 ± 3	8607 ± 3	14.9 ± 0.1	0.6 ± 0.2	0.7 ± 0.1
8	2.0	575 ± 3	8597 ± 3	15.0 ± 0.1	0.7 ± 0.3	0.6 ± 0.1
8	3.0	573 ± 3	8584 ± 3	15.0 ± 0.1	0.6 ± 0.2	0.7 ± 0.1
8	4.0	569 ± 4	8577 ± 5	15.1 ± 0.1	0.5 ± 0.2	0.6 ± 0.1
8	5.0	568 ± 2	8568 ± 5	15.1 ± 0.1	0.7 ± 0.2	0.7 ± 0.1
8	6.0	568 ± 1	8569 ± 3	15.1 ± 0.1	0.7 ± 0.2	0.6 ± 0.1

Table C.1: System with 776 lipids and 6153 solvent beads: Mean values for the area A, volume V and z-length of the simulation box L_z for different values of the hydrophobic length L of the protein and the hydrophobicity parameter ϵ_{pt}. The thickness of the lipid bilayer far away from the protein is approximately $2t_0 = 5.7 \pm 0.1\sigma_t$. The theoretical value for the tension is $\Gamma_{theory} = 0.6 \pm 0.1\epsilon/\sigma_t^2$.

$L\ [\sigma_t]$	ϵ_{pt}	$A\ [\sigma_t^2]$	$V\ [\sigma_t^3]$	$L_z\ [\sigma_t]$	$\Gamma_{slice}\ [\epsilon/\sigma_t^2]$	$\Gamma_{cylinder}\ [\epsilon/\sigma_t^2]$
4	1.0	1262 ± 3	19395 ± 9	15.4 ± 0.1	0.3 ± 0.2	0.4 ± 0.1
4	2.0	1260 ± 3	19391 ± 10	15.4 ± 0.1	0.3 ± 0.2	0.4 ± 0.1
4	3.0	1264 ± 4	19387 ± 8	15.3 ± 0.1	0.3 ± 0.2	0.4 ± 0.1
4	4.0	1266 ± 3	19386 ± 4	15.3 ± 0.1	0.2 ± 0.1	0.3 ± 0.1
4	4.0	1268 ± 2	19388 ± 8	15.3 ± 0.1	0.3 ± 0.2	0.4 ± 0.1
4	6.0	1266 ± 2	19378 ± 7	15.3 ± 0.1	0.3 ± 0.2	0.3 ± 0.1
6	1.0	1261 ± 4	19386 ± 6	15.4 ± 0.1	0.3 ± 0.1	0.4 ± 0.1
6	2.0	1264 ± 4	19383 ± 5	15.3 ± 0.1	0.3 ± 0.2	0.4 ± 0.1
6	3.0	1264 ± 3	19382 ± 6	15.3 ± 0.1	0.3 ± 0.2	0.3 ± 0.1
6	4.0	1261 ± 4	19376 ± 4	15.4 ± 0.1	0.3 ± 0.2	0.3 ± 0.1
6	5.0	1259 ± 3	19371 ± 5	15.4 ± 0.1	0.3 ± 0.2	0.2 ± 0.1
6	6.0	1259 ± 2	19370 ± 6	15.4 ± 0.1	0.4 ± 0.2	0.4 ± 0.1
8	1.0	1260 ± 4	19393 ± 5	15.4 ± 0.1	0.3 ± 0.2	0.3 ± 0.1
8	2.0	1260 ± 5	19379 ± 5	15.4 ± 0.1	0.2 ± 0.2	0.2 ± 0.1
8	3.0	1259 ± 5	19371 ± 7	15.4 ± 0.1	0.2 ± 0.2	0.4 ± 0.1
8	4.0	1257 ± 3	19360 ± 4	15.4 ± 0.1	0.3 ± 0.2	0.4 ± 0.1
8	5.0	1256 ± 3	19352 ± 5	15.4 ± 0.1	0.1 ± 0.2	0.2 ± 0.1
8	6.0	1256 ± 3	19348 ± 7	15.4 ± 0.1	0.3 ± 0.2	0.2 ± 0.1

Table C.2: System with 1776 lipids and 13846 solvent beads: Mean values for the area A, volume V and z-length of the simulation box L_z for different values of the hydrophobic length L of the protein and the hydrophobicity parameter ϵ_{pt}. The thickness of the lipid bilayer far away from the protein is about $2t_0 = 5.9 \pm 0.1\sigma_t$. The theoretical value for the tension is $\Gamma_{theory} = 0.3 \pm 0.1\epsilon/\sigma_t^2$.

$L\ [\sigma_t]$	ϵ_{pt}	$A\ [\sigma_t^2]$	$V\ [\sigma_t^3]$	$L_z\ [\sigma_t]$	$\Gamma_{slice}\ [\epsilon/\sigma_t^2]$	$\Gamma_{cylinder}\ [\epsilon/\sigma_t^2]$
4	1.0	2218 ± 5	34486 ± 13	15.5 ± 0.1	0.2 ± 0.1	0.1 ± 0.1
4	2.0	2209 ± 7	34480 ± 8	15.6 ± 0.1	0.1 ± 0.2	0.2 ± 0.1
4	3.0	2211 ± 9	34470 ± 8	15.6 ± 0.1	0.2 ± 0.1	0.2 ± 0.1
4	4.0	2221 ± 7	34474 ± 5	15.5 ± 0.1	0.1 ± 0.1	0.2 ± 0.1
4	5.0	2222 ± 14	34488 ± 8	15.5 ± 0.1	0.2 ± 0.1	0.3 ± 0.1
4	6.0	2228 ± 8	34477 ± 7	15.5 ± 0.1	0.1 ± 0.1	0.2 ± 0.1
6	1.0	2215 ± 7	34483 ± 8	15.6 ± 0.1	0.1 ± 0.1	0.1 ± 0.1
6	2.0	2218 ± 4	34464 ± 8	15.5 ± 0.1	0.1 ± 0.1	0.3 ± 0.1
6	3.0	2215 ± 3	34473 ± 8	15.6 ± 0.1	0.1 ± 0.1	0.3 ± 0.1
6	4.0	2212 ± 7	34472 ± 5	15.6 ± 0.1	0.2 ± 0.2	0.2 ± 0.1
6	5.0	2221 ± 6	34456 ± 8	15.5 ± 0.1	0.1 ± 0.2	0.2 ± 0.1
6	6.0	2215 ± 6	34464 ± 5	15.6 ± 0.1	0.1 ± 0.2	0.2 ± 0.1
8	1.0	2219 ± 6	34480 ± 7	15.5 ± 0.1	0.2 ± 0.2	0.2 ± 0.1
8	2.0	2214 ± 5	34466 ± 7	15.6 ± 0.1	0.2 ± 0.1	0.3 ± 0.1
8	3.0	2210 ± 9	34459 ± 13	15.6 ± 0.1	0.1 ± 0.2	0.2 ± 0.1
8	4.0	2210 ± 10	34444 ± 13	15.6 ± 0.1	0.1 ± 0.2	0.2 ± 0.1
8	5.0	2217 ± 5	34436 ± 14	15.5 ± 0.1	0.2 ± 0.1	0.2 ± 0.1
8	6.0	2223 ± 8	34435 ± 8	15.5 ± 0.1	0.1 ± 0.2	0.1 ± 0.1

Table C.3: System with 3176 lipids and 24614 solvent beads: Mean values for the area A, volume V and z-length of the simulation box L_z for different values of the hydrophobic length L of the protein and the hydrophobicity parameter ϵ_{pt}. The thickness of the lipid bilayer far away from the protein is approximately $2t_0 = 6.0 \pm 0.1\sigma_t$. The theoretical value for the tension is $\Gamma_{theory} = 0.2 \pm 0.1\epsilon/\sigma_t^2$.

$L\ [\sigma_t]$	ϵ_{pt}	$A\ [\sigma_t^2]$	$V\ [\sigma_t^3]$	$L_z\ [\sigma_t]$	$\Gamma_{slice}\ [\epsilon/\sigma_t^2]$	$\Gamma_{cylinder}\ [\epsilon/\sigma_t^2]$
4	1.0	559 ± 2	8618 ± 5	15.4 ± 0.1	0.3 ± 0.2	0.3 ± 0.1
4	6.0	556 ± 3	8609 ± 5	15.5 ± 0.1	0.2 ± 0.2	0.1 ± 0.1
6	1.0	553 ± 3	8613 ± 5	15.6 ± 0.1	0.1 ± 0.3	0.4 ± 0.1
6	6.0	555 ± 2	8603 ± 6	15.5 ± 0.1	0.3 ± 0.1	0.2 ± 0.1
8	1.0	556 ± 3	8612 ± 4	15.5 ± 0.1	0.1 ± 0.2	0.3 ± 0.1
8	6.0	548 ± 2	8583 ± 4	15.7 ± 0.1	0.3 ± 0.2	0.3 ± 0.1

Table C.4: System with 794 lipids, 6153 solvent beads and a thin protein: Mean values for the area A, volume V and z-length of the simulation box L_z for different values of the hydrophobic length L of the protein and the hydrophobicity parameter ϵ_{pt}. The theoretical value for the tension is $\Gamma_{theory} = 0.3 \pm 0.1\epsilon/\sigma_t^2$.

$L\ [\sigma_t]$	ϵ_{pt}	$A\ [\sigma_t^2]$	$V\ [\sigma_t^3]$	$L_z\ [\sigma_t]$	$\Gamma_{slice}\ [\epsilon/\sigma_t^2]$	$\Gamma_{cylinder}\ [\epsilon/\sigma_t^2]$
4	1.0	2198 ± 6	34488 ± 9	15.7 ± 0.1	0.1 ± 0.2	0.2 ± 0.1
4	6.0	2190 ± 6	34473 ± 7	15.7 ± 0.1	0.1 ± 0.2	0.1 ± 0.1
6	1.0	2186 ± 9	34481 ± 7	15.8 ± 0.1	0.1 ± 0.2	0.1 ± 0.1
6	6.0	2199 ± 6	34471 ± 8	15.7 ± 0.1	0.1 ± 0.1	0.2 ± 0.1
8	1.0	2188 ± 9	34480 ± 9	15.8 ± 0.1	0.1 ± 0.2	0.1 ± 0.1
8	6.0	2189 ± 5	34466 ± 11	15.7 ± 0.1	0.1 ± 0.1	0.2 ± 0.1

Table C.5: System with 3194 lipids, 24615 solvent beads and a thin protein: Mean values for the area A, volume V and z-length of the simulation box L_z for different values of the hydrophobic length L of the protein and the hydrophobicity parameter ϵ_{pt}. The theoretical value for the tension is $\Gamma_{theory} = 0.1 \pm 0.1\epsilon/\sigma_t^2$.

Appendix D

Additional Figures

D.1 Protein of Diameter $\sigma_p = 1\sigma_t$

Figure D.1 shows the thickness profiles in the vicinity of one thin protein for a system with different numbers of lipids and solvent beads: (i) 794 lipids and 6153 solvent beads, (ii) 3194 lipids and 24615 solvent beads. There is still a small difference in the thickness far away from the protein due to the tension induced by the solvent, but this difference is not as pronounced as in the case of one thick protein.

D.2 Protein with Tilt

The two figures D.2 and D.3 compare the membrane thickness profiles in the vicinity of a single protein with a length equal to the simulation box and a sphero-cylinder protein of finite length, which is not allowed to tilt. This is achieved by setting the tilt range to zero. The protein diameter is $\sigma_p = 1\sigma_t$, figure D.2, and $\sigma_p = 3\sigma_t$, figure D.3.

As already mentioned in section 6.4 the difference between the profiles is neglectable. Possible reasons for the difference are the statistics as well as the fact that there is a tension induced by the solvent, in the case of the protein with a length equal to the simulation box in z-direction. The last point plays especially a role for the thickness far away from the protein.

As a last point we want to compare the membrane thickness profiles in the vicinity of a sphero-cylinder protein of diameter $\sigma_p = 3\sigma_t$ in a lipid bilayer of different sizes: (i) 776 lipids and 6153 solvent beads, (ii) 3176 lipids and 24615 solvent beads, figure D.4. The differences in the curves are neglectable. Especially for the thickness far away from the protein we do not see a dependence on the system size.

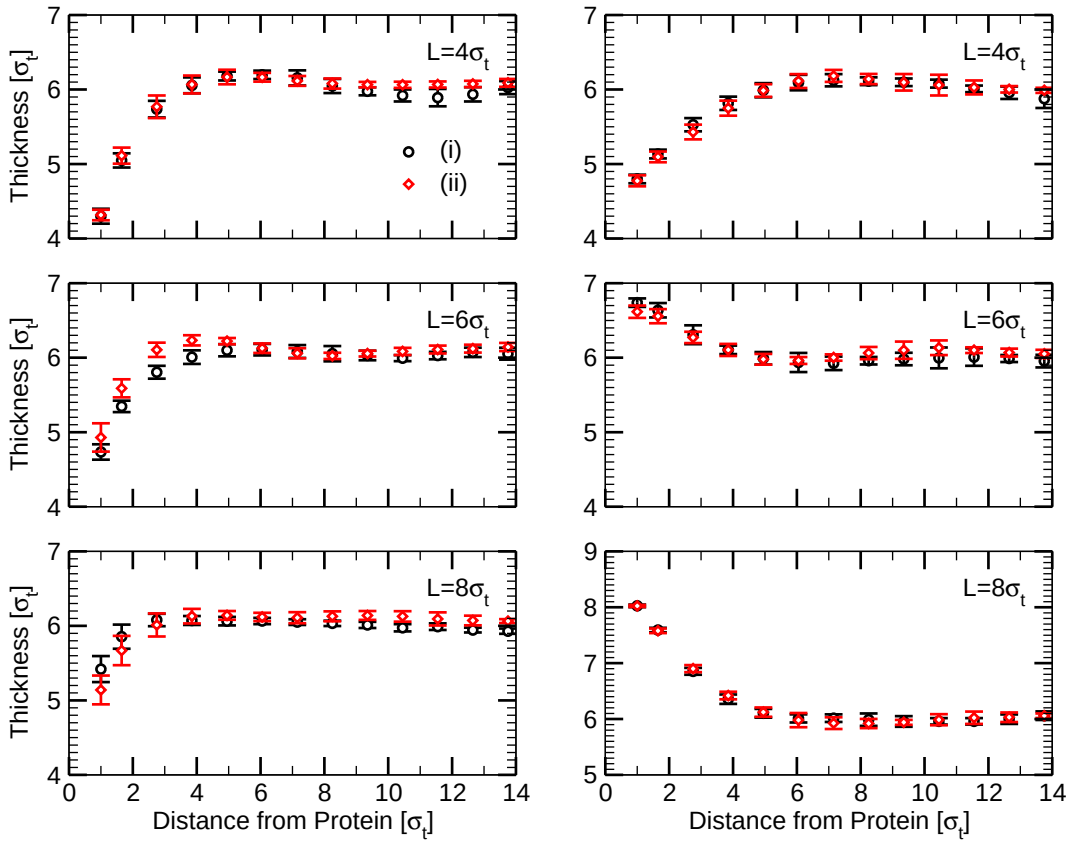

Figure D.1: Radial membrane thickness profiles in the vicinity of a thin protein of a lipid bilayer of various sizes: (i) 794 lipids and 6153 solvent beads (black circles), (ii) 3194 lipids and 24615 solvent beads (red diamonds). The hydrophobic length of the protein is $L = 4\sigma_t$ (upper panels), $L = 6\sigma_t$ (middle panels) and $L = 8\sigma_t$ (bottom panels). The hydrophobicity parameter is $\epsilon_{pt} = 1.0$ (left) and $\epsilon_{pt} = 6.0$ (right).

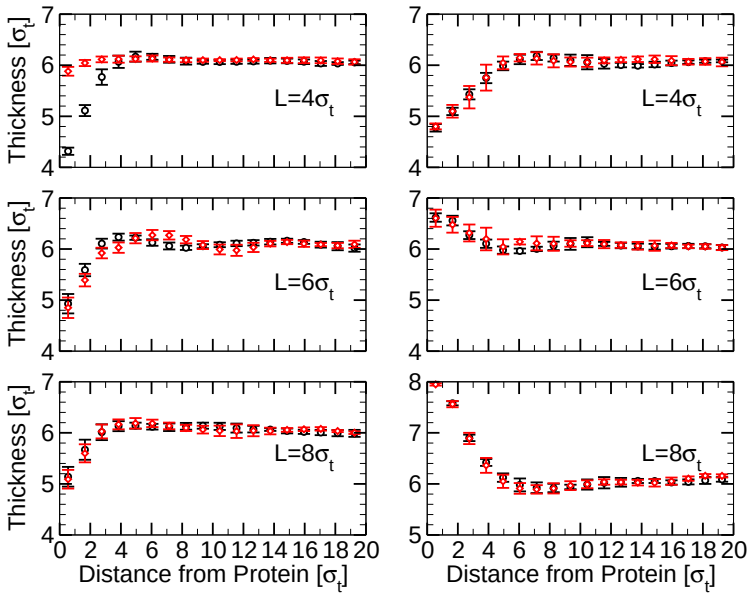

Figure D.2: Comparison of the radial thickness profiles in the vicinity of a protein of diameter $\sigma_p = 1\sigma_t$ with a length equal to the z-length of the simulation box (black circles) and a protein of finite length, which is not allowed to tilt (sphero-cylinder, red diamonds). The hydrophobicity parameter is $\epsilon_{pt} = 1.0$ (left) and $\epsilon_{pt} = 6.0$ (right). The hydrophobic length of the protein is $L = 4\sigma_t$, $6\sigma_t$, $8\sigma_t$ (from top to bottom). The data are obtained from a system with 3176 lipids.

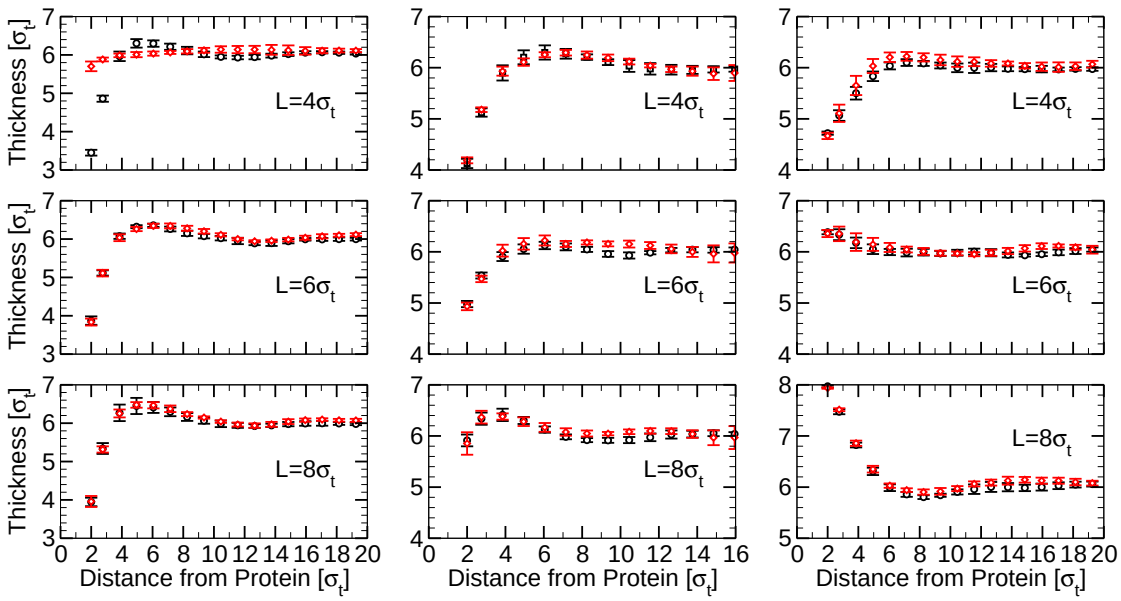

Figure D.3: Comparison of the radial thickness profiles in the vicinity of a protein of diameter $\sigma_p = 3\sigma_t$ with a length equal to the z-length of the simulation box (black circles) and a protein of finite length, which is not allowed to tilt (sphero-cylinder, red diamonds). The hydrophobicity parameter is $\epsilon_{pt} = 1.0$ (left), $\epsilon_{pt} = 2.0$ (middle) and $\epsilon_{pt} = 6.0$ (right). The hydrophobic length of the protein is $L = 4\sigma_t$, $6\sigma_t$, $8\sigma_t$ (from top to bottom). The data for $\epsilon_{pt} = 2.0$, where the protein is allowed to tilt, are obtained from a system with 776 lipids. All other data are obtained from a system with 3176 lipids.

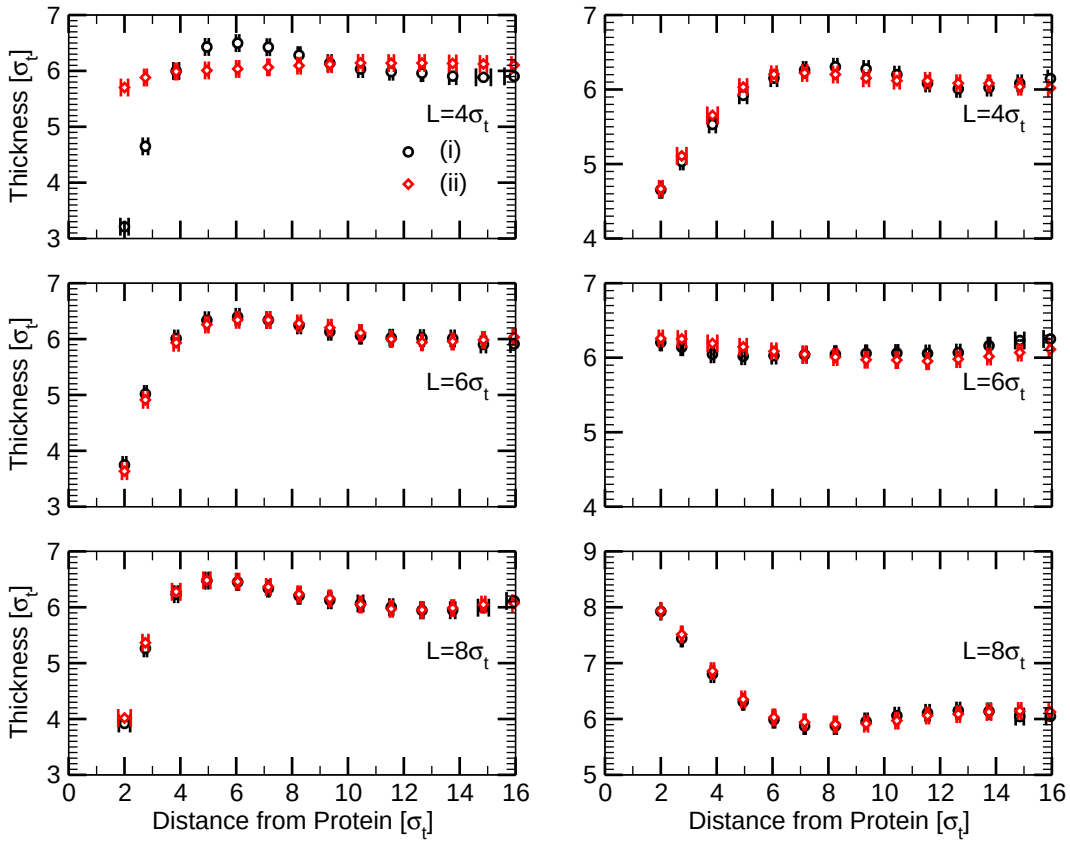

Figure D.4: Radial membrane thickness profiles in the vicinity of a sphero-cylinder protein of diameter $\sigma_p = 3\sigma_t$ of a lipid bilayer of various sizes: (i) 776 lipids and 6153 solvent beads (black circles), (ii) 3176 lipids and 24615 solvent beads (red diamonds). The hydrophobic length of the protein is $L = 4\sigma_t$ (upper panels), $L = 6\sigma_t$ (middle panels) and $L = 8\sigma_t$ (bottom panels). The hydrophobicity parameter is $\epsilon_{pt} = 1.0$ (left) and $\epsilon_{pt} = 6.0$ (right).

Bibliography

[1] http://www.ncnr.nist.gov/programs/reflect/rp/biology/cell_membrane.html.

[2] M.P. Allen. Configurational temperature in membrane simulations using dissipative particle dynamics. *J. Phys. Chem. B*, 110:3823–3830, 2006.

[3] H. Aranda-Espinoza, A. Berman, N. Dan, P. Pincus, and S.A. Safran. Interaction between inclusions embedded in membranes. *Biophysical Journal*, 71:648–656, 1996.

[4] W.L. Ash, M.R. Zlomislic, E.O. Oloo, and D.P. Tieleman. Computer simulations of membrane proteins. *Biochimica et Biophysica Acta*, 1666:158–189, 2004.

[5] N. Ben-Tal and B. Honig. Helix-helix interactions in lipid bilayers. *Biophysical Journal*, 71:3046–3050, 1996.

[6] G. Besold and K. Kremer. Werkstoffe nach Wunsch? *Physik Journal*, 3:41–47, 2004.

[7] M. Bloom, E. Evans, and O.G. Mouritsen. Physical properties of the fluid lipid-bilayer component of cell membranes: a perspective. *Quarterly Reviews of Biophysics*, 24:293–397, 1991.

[8] K. Bohinc, V. Kralj-Iglič, and S. May. Interaction between two cylindrical inclusions in a symmetric lipid bilayer. *J. Chem. Phys.*, 119:7435–7444, 2003.

[9] G. Brannigan and F.L.H. Brown. A consistent model for thermal fluctuations and protein-induced deformations in lipid bilayers. *Biophysical Journal*, 90:1501–1520, 2006.

[10] G. Brannigan and F.L.H. Brown. Contributions of the gaussian curvature and nonconstant lipid volume to protein deformation of lipid bilayers. *Biophysical Journal*, 92:864–876, 2007.

[11] G. Brannigan, P.F. Philips, and F.L.H. Brown. Flexible lipid bilayers in implicit solvent. *Physical Review E*, 72:011915, 2005.

[12] T. Chou, K.S. Kim, and G. Oster. Statistical thermodynamics of membrane bending-mediated protein-protein attractions. *Biophysical Journal*, 80:1075–1087, 2001.

[13] I.R. Cooke and M. Deserno. Solvent-free model for self-assembling fluid bilayer membranes: Stabilization of the fluid phase based on broad attractive tail potentials. *J. Chem. Phys.*, 123:224710, 2005.

[14] I.R. Cooke, K. Kremer, and M. Deserno. Tunable generic model for fluid bilayer membranes. *Physical Review E*, 72:011506, 2005.

[15] A. Cordomí and J.J. Perez. Molecular dynamics simulations of rhodopsin in different one-component lipid bilayers. *J. Phys. Chem. B*, 11:7052–7063, 2007.

[16] N. Dan, A. Berman, P. Pincus, and S.A. Safran. Membrane-induced interactions between inclusions. *J. Phys. II France*, 4:1713–1725, 1994.

[17] N. Dan, P. Pincus, and S.A. Safran. Membrane-induced interactions between inclusions. *Langmuir*, 9:2768–2771, 1993.

[18] N. Dan and S.A. Safran. Effect of lipid characteristics on the structure of transmembrane proteins. *Biophysical Journal*, 75:1410–1414, 1998.

[19] F.J.-M. de Meyer, M. Venturoli, and B. Smit. Molecular simulations of lipid-mediated protein-protein interactions. *Biophysical Journal*, 95:1851–1865, 2008.

[20] W.K. den Otter and W.J. Briels. The bending rigidity of an amphiphilic bilayer from equilibrium and nonequilibrium molecular dynamics. *J. Chem. Phys.*, 118:4712–4720, 2003.

[21] S.S. Deol, P.J. Bond, C. Domene, and M.S.P. Sansom. Lipid-portein interactions of integral membrane proteins: A comparative simulation study. *Biophysical Journal*, 87:3737–3749, 2004.

[22] P.G. Dommersnes and J.-B. Fournier. N-body study of anisotropic membrane inclusions: membrane mediated interactions and ordered aggregation. *Eur. Phys. J. B*, 12:9–12, 1999.

[23] P.G. Dommersnes, J.-B. Fournier, and P. Galatola. Long-range elastic forces between membrane inclusions in spherical vesicles. *Europhysics Letters*, 42:233–238, 1998.

[24] R.M. Dowben. *Cell Biology*. Harper & Row, New York, 1971.

[25] D. Düchs and F. Schmid. Phase behaviour of amphiphilic monolayers: theory and simulations. *J. Phys: Cond. Matt.*, 13:4853–4862, 2001.

[26] F. Dumas, M.C. Lebrun, and J.-F. Tocanne. Is the protein/lipid hydrophobic matching principle relevant to membrane organization and function? *FEBS Letters*, 458:271–277, 1999.

[27] J.R. Elliott, D. Needham, J.P. Dilger, and D.A. Haydon. The effects of bilayer thickness and tension on gramicidin single-channel lifetime. *Biochimica et Biophysica Acta*, 735:95–103, 1983.

[28] D.R. Fattal and A. Ben-Shaul. A molecular model for lipid-protein interaction in membranes: the role of hydrophobic mismatch. *Biophysical Journal*, 65:1795–1809, 1993.

[29] D.R. Fattal and A. Ben-Shaul. Lipid chain packing and lipid-protein interaction in membranes. *Physica A*, 220:192–216, 1995.

[30] J.-B. Fournier. Coupling between membrane tilt-difference and dilation: A new "ripple" instability and multiple crystalline inclusions phases. *Europhysics Letters*, 43:725–730, 1998.

[31] J.-B. Fournier. Microscopic membrane elasticity and interactions among membrane inclusions: interplay between the shape, dilation, tilt and tilt-difference modes. *Eur. Phys. J. B*, 11:261–272, 1999.

[32] M. Fošnarič, A. Iglič, and S. May. Influence of rigid inclusions on the bending elasticity of a lipid membrane. *Physical Review E*, 74:051503, 2006.

[33] D. Frenkel and B. Smit. *Understanding Molecular Simulation - From Algorithms to Applications*. Academic Press, San Diego, 2002.

[34] R.B. Gennis. *Biomembranes - Molecular Structure and Function*. Springer Verlag, New York, 1989.

[35] T. Gil, J.H. Ipsen, O.G. Mouritsen, M.C. Sabra, M.M. Sperotto, and M.J. Zuckermann. Theoretical analysis of protein organization in lipid membranes. *Biochimica et Biophysica Acta*, 1376:245–266, 1998.

[36] R. Golestanian, M. Goulian, and M. Kardar. Fluctuation-induced interactions between rods on a membrane. *Physical Review E*, 54:6725–6734, 1996.

[37] R. Golestanian, M. Goulian, and M. Kardar. Fluctuation-induced interactions between rods on membranes and interfaces. *Europhysics Letters*, 33:241–245, 1996.

[38] R. Götz, G. Gompper, and R. Lipowsky. Mobility and elasticity of self-assembled membranes. *Physical Review Letters*, 82:221–224, 1999.

[39] R. Götz and R. Lipowsky. Computer simulations of bilayer membranes: Self-assembly and interfacial tension. *J. Chem. Phys.*, 108:7397–7409, 1998.

[40] M. Goulian, R. Bruinsma, and P. Pincus. Long-range forces in heterogeneous fluid membranes. *Europhysics Letters*, 22:145–150, 1993.

[41] G. Guigas and M. Weiss. Influence of hydrophobic mismatching on membrane protein diffusion. *Biophysical Journal: Biophysical Letters*, 95:L25–L27, 2008.

[42] J. Gullingsrud, A. Babakhani, and J.A. McCammon. Computational investigation of pressure profiles in lipid bilayers with embedded proteins. *Molecular Simulation*, 32:831–838, 2006.

[43] J. Gullingsrud and K. Schulten. Lipid bilayer pressure profiles and mechanosensitive channel gating. *Biophysical Journal*, 86:3496–3509, 2004.

[44] D. Harries and A. Ben-Shaul. Conformational chain statistics in a model lipid bilayer: Comparison between mean field and Monte Carlo calculations. *J. Chem. Phys.*, 106:1609–1619, 1997.

[45] T.A. Harroun, W.T. Heller, T.M. Weiss, L. Yang, and H.W. Huang. Experimental evidence for hydrophobic matching and membrane-mediated interactions in lipid bilayers containing gramicidin. *Biophysical Journal*, 76:937–945, 1999.

[46] T.A. Harroun, W.T. Heller, T.M. Weiss, L. Yang, and H.W. Huang. Theoretical analysis of hydrophobic matching and membrane-mediated interactions in lipid bilayers containing gramicidin. *Biophysical Journal*, 76:3176–3185, 1999.

[47] P. Helfrich and E. Jakobsson. Calculation of deformation energies and conformations in lipid membranes containing gramicidin channels. *Biophysical Journal*, 57:1075–1084, 1990.

[48] H.W. Huang. Deformation free energy of bilayer membrane and its effect on gramicidin channel lifetime. *Biophysical Journal*, 50:1061–1070, 1986.

[49] H.W. Huang. Elasticity of lipid bilayer interacting with amphiphilic helical peptides. *J. Phys. II France*, 5:1427–1431, 1995.

[50] J.H. Irving and J.G. Kirkwood. The statistical mechanical theory of transport processes. IV. The equations of hydrodynamics. *J. Chem. Phys.*, 18:817–829, 1950.

[51] F. Jähnig. Critical effects from lipid-protein interaction in membranes. *Biophysical Journal*, 36:329–345, 1981.

[52] A.F. Jakobsen, O.G. Mouritsen, and G. Besold. Artifacts in dynamical simulations of coarse-grained model lipid bilayers. *J. Chem. Phys.*, 122:204901, 2005.

[53] M.Ø. Jensen and O.G. Mouritsen. Lipids do influence protein function – the hydrophobic matching hypothesis revisited. *Biochimica et Biophysica Acta*, 1666:205–226, 2004.

[54] S.K. Kandasamy and R.G. Larson. Molecular dynamics simulations of model trans-membrane peptides in lipid bilayers: A systematic investigation of hydrophobic mismatch. *Biophysical Journal*, 90:2326–2343, 2006.

[55] J.A. Killian. Hydrophobic mismatch between proteins and lipids in membranes. *Biochimica et Biophysica Acta*, 1376:401–416, 1998.

[56] K.S. Kim, J. Neu, and G. Oster. Curvature-mediated interactions between membrane proteins. *Biophysical Journal*, 75:2274–2291, 1998.

[57] Z. Kóta, T. Pali, and D. Marsh. Orientation and lipid-peptide interactions of gramicidin A in lipid membranes: Polarized attenuated total reflection infrared spectroscopy and spin-label electron spin resonance. *Biophysical Journal*, 86:1521–1531, 2004.

[58] R. Koynova and M. Caffrey. Phases and phase transitions of the phosphatidylcholines. *Biochimica et Biophysica Acta*, 1376:91–145, 1998.

[59] M. Kranenburg, M. Venturoli, and B. Smit. Phase behavior and induced interdigitation in bilayers studied with dissipative particle dynamics. *J. Phys. Chem. B*, 107:11491–11501, 2003.

[60] P. Lagüe, M.J. Zuckermann, and B. Roux. Protein inclusion in lipid membranes: A theory based on the hypernetted chain integral equation. *Faraday Discuss.*, 111:165–172, 1998.

[61] P. Lagüe, M.J. Zuckermann, and B. Roux. Lipid-mediated interactions between intrinsic membrane proteins: A theoretical study based on integral equations. *Biophysical Journal*, 79:2867–2879, 2000.

[62] P. Lagüe, M.J. Zuckermann, and B. Roux. Lipid-mediated interactions between intrinsic membrane proteins: Dependence on protein size and lipid composition. *Biophysical Journal*, 81:276–284, 2001.

[63] A.G. Lee. Lipid-protein interactions in biological membranes: a structural perspective. *Biochimica et Biophysica Acta*, 1612:1–40, 2003.

[64] O. Lenz. *Computer simulations of lipid bilayers*. Dissertation, Universität Bielefeld, 2007.

[65] O. Lenz and F. Schmid. A simple computer model for liquid lipid bilayers. *J. Mol. Liquids*, 117:147–152, 2005.

[66] O. Lenz and F. Schmid. Structure of symmetric and asymmetric ripple phases in lipid bilayers. *Physical Review Letters*, 98:058104, 2007.

[67] E. Lindahl and O. Edholm. Mesoscopic undulations and thickness fluctuations in lipid bilayers from molecular dynamics simulations. *Biophysical Journal*, 79:426–433, 2000.

[68] E. Lindahl and O. Edholm. Spatial and energetic-entropic decomposition of surface tension in lipid bilayers from molecular dynamics simulations. *J. Chem. Phys.*, 113:3882–3893, 2000.

[69] S.J. Marrink and A.E. Mark. Effect of undulations on surface tension in simulated bilayers. *J. Phys. Chem. B*, 105:6122–6127, 2001.

[70] S.J. Marrink, H.J. Risselada, S. Yefimov, D.P. Tieleman, and A.H. de Vries. The MARTINI force field: Coarse grained model for biomolecular simulations. *J. Phys. Chem. B*, 111:7812–7824, 2007.

[71] G. Marsaglia. Choosing a point from the surface of a sphere. *The Annals of Mathematical Statistics*, 43:645–646, 1972.

[72] D. Marsh. Elastic curvature constants of lipid monolayers and bilayers. *Chemistry and Physics of Lipids*, 144:146–159, 2006.

[73] S. Marčelja. Chain ordering in liquid crystals – II. Structure of bilayer membranes. *Biochimica et Biophysica Acta*, 367:165–176, 1974.

[74] S. Marčelja. Lipid-mediated protein interaction in membranes. *Biochimica et Biophysica Acta*, 455:1–7, 1976.

[75] S. May. Protein-induced bilayer deformations: the lipid tilt degree of freedom. *Eur Biophys J*, 29:17–28, 2000.

[76] S. May. Theories on structural perturbations of lipid bilayers. *Current Opinion in Colloid & Interface Science*, 5:244–249, 2000.

[77] S. May and A. Ben-Shaul. Molecular theory of lipid-protein interaction and the L_α-$H_{||}$ transition. *Biophysical Journal*, 76:751–767, 1999.

[78] S. May and A. Ben-Shaul. A molecular model for lipid-mediated interaction between proteins in membranes. *Phys. Chem. Chem. Phys.*, 2:4494–4502, 2000.

[79] Message Passing Interface Forum. *MPI: A Message-Passing Interface Standard*. University of Tennessee, Knoxville, 1995.

[80] B. Mohr. *Introduction to Parallel Computing*. Forschungszentrum Jülich, 2006. Cecam Tutorial "Programming Parallel Computers".

[81] O.G. Mouritsen and M. Bloom. Models of lipid-protein interactions in membranes. *Annu. Rev. Biophys. Biomol. Struct.*, 22:145–171, 1993.

[82] M. Müller, K. Katsov, and M. Schick. Biological and synthetic membranes: What can be learned from a coarse-grained description? *Physics Reports*, 434:113–176, 2006.

[83] F. Müller-Plathe. Coarse-graining in polymer simulation: From the atomistic to the mesoscopic scale and back. *CHEMPHYSCHEM*, 3:754–769, 2002.

[84] J.F. Nagle, R. Zhang, S. Tristram-Nagle, W. Sun, H.I. Petrache, and R.M. Suter. X-ray structure determination of fully hydrated L_α phase dipalmitoylphosphatidylcholine bilayers. *Biophysical Journal*, 70:1419–1431, 1996.

[85] J. Neder. Private communication.

[86] R.R. Netz. Inclusions in fluctuating membranes: Exact results. *J. Phys. I France*, 7:833–852, 1997.

[87] C. Nielsen and O.S. Andersen. Inclusion-induced bilayer deformations: Effects of monolayer equilibrium curvature. *Biophysical Journal*, 79:2583–2604, 2000.

[88] C. Nielsen, M. Goulian, and O.S. Andersen. Energetics of inclusion-induced bilayer deformations. *Biophysical Journal*, 74:1966–1983, 1998.

[89] S.O. Nielsen, B. Ensing, V. Ortiz, P.B. Moore, and M.L. Klein. Lipid bilayer perturbations around a transmembrane nanotube: A coarse grain molecular dynamics study. *Biophysical Journal*, 88:3822–3828, 2005.

[90] M. Orsi, D.Y. Haubertin, W.E. Sanderson, and J.W. Essex. A quantitative coarse-grain model for lipid bilayers. *J. Phys. Chem. B*, 112:802–815, 2008.

[91] J.C. Owicki and H.M. McConnell. Theory of protein-lipid and protein-protein interactions in bilayer membranes. *Proc. Natl. Acad. Sci. USA*, 76:4750–4754, 1979.

[92] J.C. Owicki, M.W. Springgate, and H.M. McConnell. Theoretical study of protein-lipid interactions in bilayer membranes. *Proc. Natl. Acad. Sci. USA*, 75:1616–1619, 1978.

[93] J.-M. Park and T.C. Lubensky. Interactions between membrane inclusions on fluctuating membranes. *J. Phys. I France*, 6:1217–1235, 1996.

[94] L.T. Pearson, J. Edelman, and S.I. Chan. Statistical mechanics of lipid membranes – protein correlation function and lipid ordering. *Biophysical Journal*, 45:863–871, 1984.

[95] E. Peschel. *Differentialgeometrie*. BI Hochschultaschenbücher, Mannheim, 1973.

[96] S.A. Safran. *Statistical Thermodynamics of Surfaces, Interfaces, and Membranes*. Perseus Books, Cambridge, Massachusetts, 1994.

[97] F. Schmid, D. Düchs, O. Lenz, and B. West. A generic model for lipid monolayers, bilayers, and membranes. *Computer Physics Communications*, 177:168–171, 2007.

[98] F. Schmid and M. Schick. Liquid phases of Langmuir monolayers. *J. Chem. Phys.*, 102:2080–2091, 1995.

[99] U. Schmidt, G. Guigas, and M. Weiss. Cluster formation of transmembrane proteins due to hydrophobic mismatching. *Physical Review Letters*, 101:128104, 2008.

[100] H. Schröder. Aggregation of proteins in membranes. An example of fluctuation-induced interactions in liquid crystals. *J. Chem. Phys.*, 67:1617–1619, 1977.

[101] P. Sens and S.A. Safran. Inclusions induced phase separation in mixed lipid film. *Eur. Phys. J. E*, 1:237–248, 2000.

[102] J.C. Shillcock and R. Lipowsky. Equilibrium structure and lateral stress distribution of amphiphilic bilayers from dissipative particle dynamics simulations. *J. Chem. Phys.*, 117:5048–5061, 2002.

[103] T. Sintes and A. Baumgärtner. Protein attraction in membranes induced by lipid fluctuations. *Biophysical Journal*, 73:2251–2259, 1997.

[104] T. Sintes and A. Baumgärtner. Short-range attractions between two colloids in a lipid monolayer. *J. Chem. Phys.*, 106:5744–5750, 1997.

[105] T. Sintes and A. Baumgärtner. Interaction of wedge-shaped proteins in flat bilayer membranes. *J. Phys. Chem. B*, 102:7050–7057, 1998.

[106] T. Sintes and A. Baumgärtner. Membrane-mediated protein attraction. A monte carlo study. *Physica A*, 249:571–575, 1998.

[107] J. Sonne, F.Y. Hansen, and G.H. Peters. Methodological problems in pressure profile calculations for lipid bilayers. *J. Chem. Phys.*, 122:124903, 2005.

[108] M.M. Sperotto and O.G. Mouritsen. Monte carlo simulation studies of lipid order parameter profiles near integral membrane proteins. *Biophysical Journal*, 59:261–270, 1991.

[109] D. Starck, K. Fiedler, P. Harth, and J. Richter, editors. *Biologie – Eine Vorlesungsreihe für Mediziner und Naturwissenschaftler*. Verlag Chemie, Weinheim, 1981.

[110] D.P. Tieleman, J.L. MacCallum, W.L. Ash, C. Kandt, Z. Xu, and L. Monticelli. Membrane protein simulations with a united-atom lipid and all-atom protein model: lipid-protein interactions, side chain transfer free energies and model proteins. *J. Phys: Condens. Matter*, 18:1221–1234, 2006.

[111] D.P. Tieleman, S.J. Marrink, and H.J.C. Berendsen. A computer perspective of membranes: molecular dynamics studies of lipid bilayer systems. *Biochimica et Biophysica Acta*, 1331:235–270, 1997.

[112] D.J. Tobias, K. Tu, and M.L. Klein. Atomic-scale molecular dynamics simulations of lipid membranes. *Current Opinion in Colloid & Interface Science*, 2:15–26, 1997.

[113] A. Uhlherr, S.J. Leak, N.E. Adam, P.E. Nyberg, M. Doxastakis, V.G. Mavrantzas, and D.N. Theodorou. Large scale atomistic polymer simulations using Monte Carlo methods for parallel vector processors. *Computer Physics Communications*, 144:1–22, 2002.

[114] F. Varnik, J. Baschnagel, and K. Binder. Molecular dynamics results on the pressure tensor of polymer films. *J. Chem. Phys.*, 113:4444–4453, 2000.

[115] M. Venturoli, B. Smit, and M.M. Sperotto. Simulation studies of protein-induced bilayer deformations, and lipid-induced protein tilting, on a mesoscopic model for lipid bilayers with embedded proteins. *Biophysical Journal*, 88:1778–1798, 2005.

[116] M. Venturoli, M.M. Sperotto, M. Kranenburg, and B. Smit. Mesoscopic models of biological membranes. *Physics Reports*, 437:1–54, 2006.

[117] D. Walther, P. Kuzmin, and E. Donath. Brownian dynamics simulation of the lateral distribution of charged membrane components. *Eur Biophys J*, 24:125–135, 1996.

[118] T.R. Weikl. Fluctuation-induced aggregation of rigid membrane inclusions. *Europhysics Letters*, 54:547–553, 2001.

[119] J.T. Wescott, L.R. Fisher, and S. Hanna. Use of thermodynamic integration to calculate the hydration free energies of n-alkanes. *J. Chem. Phys.*, 116:2361–2369, 2002.

Danksagung

An dieser Stelle möchte ich einigen Personen danken, die mich während dieser Arbeit maßgeblich unterstützt haben:

- Friederike Schmid, die immer Zeit sowie ein offenes Ohr für meine Fragen und Probleme hatte.
- Jürgen Schnack für das Erstellen des zweiten Gutachtens.
- Jörg Neder von der Universität Konstanz für seine Diskussionsanregungen und die ausgesprochen gute Zusammenarbeit.
- Olaf Lenz für die geleisteten Vorarbeiten sowie für die Überlassung seines Computerprogrammes.
- Der Arbeitsgruppe „Theorie der kondensierten Materie“ für die wunderbare Arbeitsatmosphäre. Insbesondere möchte ich Hanne Litschewsky für ihre Unterstützung danken.
- Gerhard Ahlers für seine immerwährende Hilfe bei der Administration unseres Rechenclusters.
- Der Großteil der Simulationen wurden im Paderborn Center for Parallel Computing (PC2) sowie dem NIC Computer Center in Jülich durchgeführt.
- Diese Arbeit ist im Rahmen des Teilprojektes A2 des Sonderforschungsbereiches 613 „Physik von Einzelmolekülprozessen und molekularer Erkennung in organischen Systemen“, der von der Deutschen Forschungsgemeinschaft finanziert wird, entstanden.
- Ronald Simmonds für das Korrekturlesen dieser Arbeit.
- Meinen Eltern und Torsten für ihre unermüdliche Geduld und Unterstützung.

Eidesstattliche Erklärung

Der Inhalt der Anhänge A und B wurde von Friederike Schmid entwickelt.

Hiermit versichere ich, die vorliegende Arbeit selbständig angefertig zu haben und keine anderen Hilfsmittel als die angegebenen verwendet zu haben.

Bielefeld, den 3. Dezember 2008